

Characterization of non-linear compliant shell mechanisms

To enhance the design process of a compliant scoliosis brace

by

J.R. Leemans

Student number: 4106555
Project duration: February 27, 2017 – May 22, 2018
Supervisors: Prof. dr. ir. J.L Herder, TU Delft
Associate Prof. dr. M.Sc.Eng. C.J. Kim, Bucknell University
Ir. W.W.PJ van de Sande, TU Delft

Preface

This is the final result of my master High-Tech Engineering at the Technical University Delft, at the faculty of Mechanical, Maritime and Material Engineering. I am truly honoured that the results of this master thesis are communicated to the outside world.

First and foremost, I would like to thank my advisor, Charles, for his involvement, motivation, and thorough feedback during my research. I am grateful for the opportunity he gave me to join his project in the United States. I would also like to thank my daily advisor, Werner, for his excellent guidance, input and interesting discussions. Furthermore, I would like to thank my chair, Just, for his thoughtful recommendations and oversight. Last, but certainly not least, I would like to gratefully thank my parents and Else for their incredible support throughout the years.

J.R. Leemans
Rotterdam, May 2018

Contents

I	Master Thesis	1
1	Introduction	3
2	Design Strategy	5
	Paper: Functional Requirement Quantification Strategy of a Compliant Scoliosis Brace	5
3	Characterization Theory	13
	Paper: Unified Stiffness Characterization of Non-Linear Compliant Shell Mechanisms	13
4	Characterization Experiment	27
	Experimental Determination and Validation of Critical Components of the Unified Stiffness	27
5	Characterization Library	35
	Paper: Compliant Shell Building Block Characterization Library Utilizing Unified Stiffness	35
6	Discussion	45
7	Conclusion	47
II	Appendix	49
A	Additional Paper Linear Characterization Theory	51
	Paper: Unified Rotational and Translational Stiffness Characterization of Compliant Mechanisms . . .	51
B	Non-linear characterization library of promising building blocks	65
C	Experiment Data	71
D	Background Theory	75
	D.1 Structural analysis	75
	D.2 Potential Energy	79
	D.3 Twist and wrench location vector and pitch	80
E	Derivations and Algorithms	81
	E.1 Derivation Translation as Rotation method	81
	E.2 Derivation moment arm	81
	E.3 Quantitative example	82
F	Preliminary work synthesis	85
	F.1 Parallel and series conjunctions spatial mechanisms	85
	F.2 Rigid-body replacement utilizing Lipkin's eigen-decomposition	89
	F.3 Systematic linearisation utilizing Lipkin's eigen-decomposition	89
	Bibliography	93

I

Master Thesis

Introduction

Scoliosis is defined as an irregular curvature of the spine that can cause pain and severe complications [12]. Braces are prescribed for moderate deformations to prevent progression of the spine deformity [14, 19]. Research has shown that wearing a scoliosis brace can negatively influence the emotional and social well-being of patients, leading to decreased user compliance [19]. Reduced compliance towards the brace has been shown to be the most common cause of failure in treatment [16]. The main contributing factor to the reduced user compliance is the restricted in-brace allowable range of motion [15].

The main research objective of this thesis is to enhance the design process of an effective compliant scoliosis brace. This brace should provide correctional loads while allowing in-brace range of motion. This work utilizes compliant mechanisms to transmit these correctional loads through constraint directions while allowing motion in freedom directions. Compliant shell mechanisms, in particular, are highly suitable for the application of human-assistive devices, such as the compliant scoliosis brace. Their monolithic lightweight thin-walled nature makes them ideal to clean, wear and conceal under clothes. Furthermore, the human body does not have clear distinctive constraint and free motion directions, similar to compliant shell mechanisms. Additional general benefits of compliant mechanisms, as described by Howell [5], are no wear, no backlash, low friction, easy assembly and no need for lubrication.

Designing a compliant scoliosis brace that utilizes compliant shell mechanisms motivates the development of spatial compliant shell mechanism design method. Various approaches and methods are available to design compliant mechanisms, as presented by Gallego [3]. However, these approaches are often not suitable for spatial compliant shell mechanisms. This is emphasized by the extensive use of lumped compliance, flexures and planar mechanisms. Available design methods for compliant mechanisms include the Pseudo-Rigid-Body Model, which requires an initial pseudo-rigid design [5]. Topology optimization based approaches, which provide limited insight into the design process as stated by Kim [8] and Gallego [3]. The Freedom and Constraint Topology (FACT) method, introduced by Hopkins [4], which is based on strict freedom and constraint directions, therefore only suitable for spatial flexure mechanisms. Type synthesis approaches utilize characterized building blocks to synthesize complex planar [10] and spatial [6] mechanisms. Nijssen [7] first introduced a promising type synthesis approach to design with spatial compliant shell mechanisms.

Nijssen's type synthesis approach was introduced to design a compliant scoliosis brace that allows in-brace motion and facilitate a force based correction, utilizing compliant shell mechanisms. By introducing a new type synthesis approach along with an unconventional force based correction strategy the final result of Nijssen was difficult to validate [1], as the complex brace-tissue interaction was not taken into account. The ability to validate the compliant scoliosis brace design process, presented in this work, is increased by utilizing the conventional displacement-based correction strategy while adding the desired compliance. The conventional displacement-based control strategy improves the ability to validate a possible brace design, since the correction efficiency can be determined using BraceSim [2]. BraceSim is a validated software tool to simulate the effectiveness of a scoliosis brace prior to manufacture. The displacement correction strategy is based on a displacement controlled reduction of the spinal curvature.

A strategy is presented to reduce the complexity of a bio-mechanical compliant brace design problem into an isolated mechanical problem. Utilizing BraceSim, the main functional requirements of a compliant scoliosis brace are quantified into validatable kinematic design specifications. The kinematic design specifications include desired non-linear behaviour of compliant shell mechanisms, since the motion of the patient is facilitated by large deformations of compliant shell mechanisms.

A building block synthesis approach has proven useful by Nijssen to match compliant shell mechanisms and kinematic design specifications. However, the introduced building block type synthesis approach by Nijssen is based on linear compliance ellipsoids [9]. By taking into account non-linear behaviour of spa-

tial compliant shell mechanisms in concept design, the discrepancy is reduced between the non-linear analysis and the desired non-linear design specifications in a later design stage. However, a compliant shell building block type synthesis approach that takes into account non-linear behaviour is not available in literature. This is explained by limited non-linear characterization and classification methods available for compliant shell mechanisms. One of the principle challenges in designing compliant shell mechanism characterization lies in the intertwined kinematics and kinetics coupled with geometrically non-linear deformations.

The key contribution of this master thesis is a comprehensive characterization method for any non-linear compliant mechanisms, this includes both flexure and shell mechanisms. This method enable the development of a non-linear spatial synthesis approach. This work presents a unified stiffness method to compare and visualize all six kinematic degrees of freedom directions and magnitudes of non-linear mechanisms in a non-arbitrary physically meaningful manner. The presented theory is demonstrated and validated through an experiment.

A library of promising building blocks is introduced which are characterized using the unified stiffness characterization method. The non-linear behaviour of the building blocks is consistently described and generalized. The building block library and the generalization potentially form the basis for a compliant shell building block synthesis method.

The body of this master thesis consists of three independent papers and an experiment. The overall strategy to contribute to the design process of a scoliosis brace is shown in Figure 1.1. Chapter 2 contains the quantification of main functional requirements of a compliant scoliosis brace into validatable kinematic design specifications. Chapter 2 does not contain a key scientific contribution at this stage, but it does support the necessity of the subsequent Chapters. Chapter 3 contains the key contribution of this master thesis. A scientific paper introduces the concept of the unified stiffness, a comprehensive non-linear characterization and classification method. Chapter 4 presents an experiment to demonstrate the introduced theory. Chapter 5 contains a scientific paper that introduces a library of promising building blocks which are characterized using the unified stiffness method. The behaviour of the building blocks is consistently described and generalized.

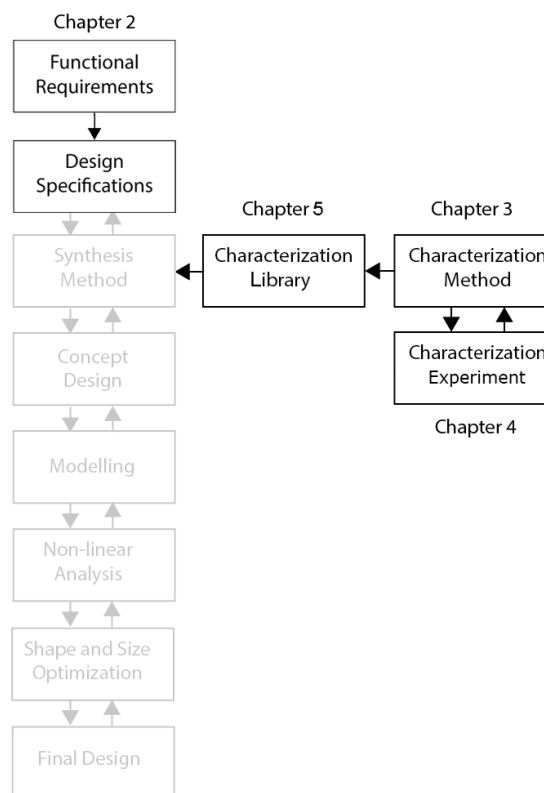


Figure 1.1: Research objective strategy diagram

2

Design Strategy

Paper: Functional Requirement Quantification Strategy of a Compliant Scoliosis Brace

While this chapter is written in paper form it does not contain publishable contribution in this stage of the design process, however it does support the demand for the subsequent scientific papers in Chapters 3, 5 and Appendix A.

FUNCTIONAL REQUIREMENT QUANTIFICATION STRATEGY OF A COMPLIANT SCOLIOSIS BRACE

Tim J. Dries

Dep. of BioMechanical Eng.
Delft University of Technology
The Netherlands
Email: t.j.dries@student.tudelft.nl

Joost R. Leemans

Dep. of Precision and Microsystems Eng.
Delft University of Technology
The Netherlands
Email: j.r.leemans@student.tudelft.nl

Charles J. Kim

Dep. of Mechanical Eng.
Bucknell University
Lewisburg, PA. USA
Email: cjk019@bucknell.edu

ABSTRACT

3% of adolescents suffer from Scoliosis, a spinal deformation of which 10% needs to be treated. Bracing is a common treatment to prevent curve progression. Current scoliosis brace designs are usually rigid or flexible, which either score high in terms of success rate of treatment or in comfort and patient compliance. Attempts have been made to overcome these problems using a compliant brace design. Previous work has shown the ability of spatial mechanisms to combine correction with flexibility. In this work, the functional requirements that lead to correct treatment and allow motion are quantified by deducing validated brace characteristics using BraceSim and combining this with patient motion data. A strategy is proposed, reducing the complexity of the bio-mechanical problem into an isolated mechanical problem. This strategy provides a structure and serves as a structural process-tree to enhance the design of a new, compliant scoliosis brace.

INTRODUCTION

Adolescent Idiopathic Scoliosis (AIS) can be defined as a three-dimensional deformity of the spine, which is characterized by a lateral curvature with a Cobb angle of more than 10 degrees and rotated vertebrae. [1] [2] AIS develops in around 3% of all adolescents, of which approximately 10% has progressive curves that require treatment of some sort. [3]

Treatment possibilities for AIS include surgery, muscle stimulation and training and bracing, depending on the severity of the deformation. Severity of the deformation is measured by the Cobb angle, which is the angle between the two most tilted vertebrae of the spine. [4] When the Cobb angle exceeds 25 degrees, braces are prescribed to prevent further progression of the scoliotic deformation. [5] If the Cobb angle exceeds 40 degrees, usually surgery is performed in order to reduce the deformity by fusing vertebrae together using metal rods and bolts.

Among current state of bracing there are both rigid and flexible solutions. The rigid braces generally have a higher success

rate, but limit the user in their Range of Motion (RoM), thus obstructing the wearer to perform their Activities of Daily Living (ADL). Flexible braces, on the other hand, generally perform better on these criteria but have been shown to generally have a lower success rate in terms of treatment. [6]

In the current project, the research objective is to design a scoliosis brace that corrects the spinal deformation, while allowing for motion during daily activities. Such a brace should be able to provide the high correction rates of rigid braces, while simultaneously using the non-rigidity of flexible braces to allow the patient to move and bend their torso.

Attempts have been made to develop semi-rigid or compliant braces. These promising brace designs show the unique abilities of shell mechanisms being compliant while simultaneously transmitting forces [6] [7].

Nijssen [6] first introduced a spatial mechanism approach to design scoliosis braces which allow motion and facilitate a force based correction utilizing compliant shell mechanisms. By introducing a new type synthesis approach along with an unconventional force based correction strategy the final result of Nijssen was difficult to validate [8], since the complex brace-tissue interaction was not taken into account [6]. Furthermore, no generalized motion data was available, which is why these proof-of-concept braces were focused on specific subjects.

The design strategy presented in this work, is based on the conventional displacement based control strategy while adding compliance using compliant shell elements. Compliant shell mechanisms are highly suitable for the application of human-assistive devices, such as the compliant scoliosis brace. Their monolithic lightweight thin-walled nature makes them ideal to clean, wear and conceal under clothes. Furthermore, the human spine does not have clear distinctive constraint and free motion directions, similar to compliant shell mechanisms.

The conventional displacement based control strategy improves the ability to validate a possible brace design, since the correction efficiency can be determined using BraceSim [9]. BraceSim is a validated software tool to simulate the effective-

ness of a scoliosis brace prior to manufacture, and is developed by our collaborators from the École Polytechnique de Montréal.

The presented strategy reduces the complexity of a bio-mechanical compliant brace design problem into an isolated mechanical problem. Utilizing BraceSim, the main functional requirements of a compliant scoliosis brace are quantified into validatable kinematic design specifications. The kinematic design specifications include desired non-linear behaviour of compliant shell mechanisms. The proposed strategy contributes to the overall design process of designing a compliant scoliosis brace.

Case selection

The strategy presented in this paper, is explained on the basis of patient data provided by our collaborators from the École Polytechnique de Montréal. In this paper this analyzed patient is referred to as the correction study patient. The proposed strategy requires motion data of this patient, however the motion data of the correction study patient was not available. Therefore a motion study was performed on a different patient with similar scoliotic characteristics. This patient was selected by an experienced orthopaedic by comparing the X-rays of the braced patient (correction study patient) with the X-rays of all patients participating in a spinal motion characterization study performed by Dries [10]. From here on this patient is referred to as the motion study patient. Table 1 provides a comparison of the relevant data between the correction study patient and the motion study patient, this includes the spinal length and the Cobb angle.

TABLE 1. COMPARISON BETWEEN CORRECTION STUDY PATIENT AND THE MOTION STUDY PATIENT

	Length T4-S1	Cobb angle
Correction study patient	259.7 mm	25°
Motion study patient	302.5 mm	20°

Since the motion study patient and correction study patient have different body lengths, likely the motion characteristics differ between these subjects.

In this work, it is assumed that both patients have similar bend characteristics and that the captured spatial axes of rotation can be scaled by 0.86 to match the correction study patient's body length.

Since the Cobb angle differs by 20%, further research should be pursued to investigate motion characteristics for patients with different Scoliotic curvatures and Cobb angles, as discussed by Dries [10].

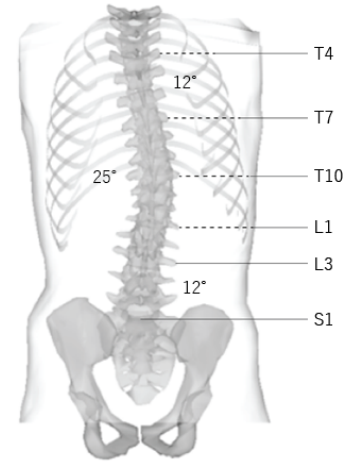


FIGURE 1. PATIENT'S SPINE POSTERIOR VIEW

The correction study patient has the minimum Cobb angle for which braces are prescribed. [5] The spinal deformation of this patient is a so-called C-shaped curvature, having just one apex and consequently one focus area for correction. Patient information containing a finite element model (FEM) of the correction study patient's torso and spine was gathered using surface topography and bi-planar radio-graphs as described in [9]. A visualization of the spine, including the deformation angles, of the correction study patient is depicted in Figure 1.

QUANTIFICATION OUTLINE

This section presents the outline of the proposed strategy to quantify main functional requirements into validatable design specifications of a compliant scoliosis brace. The strategy steps are briefly introduced in this section and shown in Figure 2. Each strategy step will be explained in detail in a separate section and illustrated on the basis of the correction study patient.

Step I - Functional requirements: From the design objective follow the main qualitative functional requirements, which include the facilitation of correction and motion. The key component of the approach is to reduce the complex bio-mechanical functional requirements into isolated mechanical design specifications, by utilizing BraceSim.

Step II_A - Correction analysis: The correction strategy is based on the modification of a validated conventional scoliosis brace, designed by a certified orthotist using BraceSim. This validated conventional scoliosis brace is referred to as the benchmark brace. The analysis of the benchmark brace determines the correctional strategy.

Step II_B - Motion analysis: The motion characteristics determine the desired compliance of the to be designed brace.

Step III - Segment division: Based on correction and mo-

tion analysis, we determine which segment of the brace can be compliant and which segments need to be stiff.

Step IV - Isolated segment analysis: A modified benchmark brace is introduced that results in a similar correction as the original benchmark brace, obtained in BraseSim. In the modified benchmark brace the, to be designed, compliant segment is temporarily modelled as a stiff segment. The temporary stiff segment connects the permanent stiff segments. The temporary stiff segment is isolated to determine the required transmitted loads and deformation using BraseSim.

Step V - Design specifications: The design specifications follow from the temporary stiff segment and the motion characteristics. The stiff segment can be substituted by a compliant segment that can transmit the required loads but is compliant in desired directions.

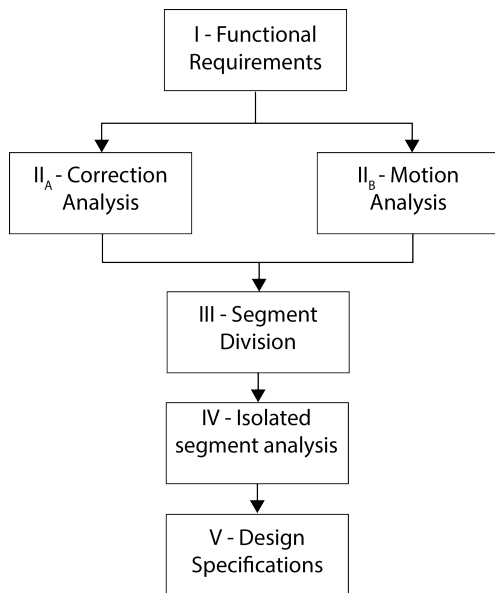


FIGURE 2. QUANTIFICATION STRATEGY DIAGRAM

I - FUNCTIONAL REQUIREMENTS

The main objective is to design a scoliosis brace that corrects the spinal deformations and allows for motion during activities of daily living.

From the design objective two seemingly contradicting main functional requirements can be extracted, given as:

- *Facilitate correction* to reduce the deformation of the spine.
- *Facilitate motion* necessary for activities of daily living.

Additional functional requirements are less crucial to present the introduced strategy and are therefore not addressed

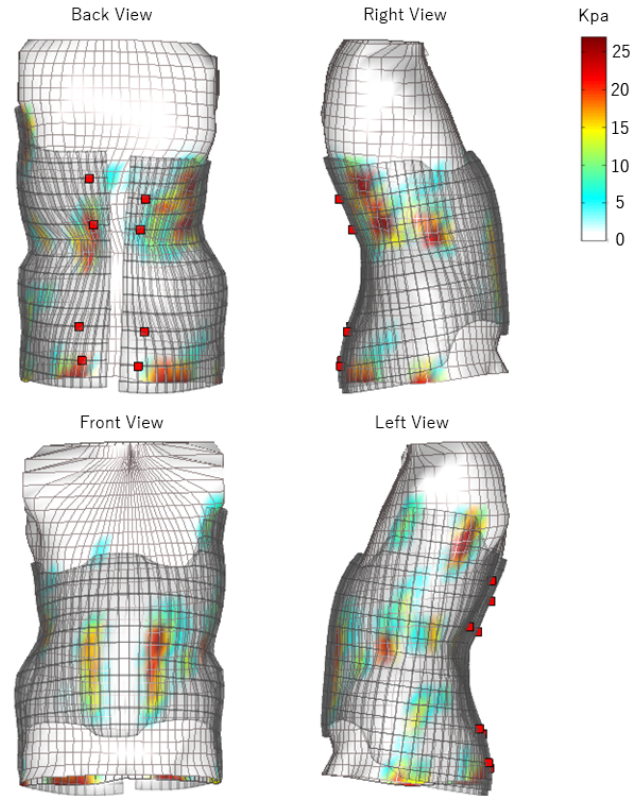


FIGURE 3. VALIDATED BRACE INCLUDING PRESSURES

in this paper. The main functional requirements are qualitative and should be translated into quantitative design specifications. The key contribution of this paper is the strategy that enables this quantification using the steps illustrated in Figure 2.

II_A - CORRECTION ANALYSIS

The correction strategy should accomplish the functional requirement "facilitate correction". The correction strategy is based on a brace designed by a certified orthotist and validated using BraseSim, which is defined as the benchmark brace. The correction of the spinal deformation and the pressures resulting from the benchmark in-brace model serve as correction efficiency benchmark for the design specifications of a new compliant brace design.

The validated brace model and the in-brace results of the correction study patient are shown in Figures 3 and 4.

As can be observed by comparing Figures 1 and 4 the Cobb angle is reduced by 11 degrees under influence of the benchmark brace. We consider this as successful treatment, since usually brace treatment is regarded as being successful when curve progression is less than 5°. [11]

The pressure maps in Figures 3 and 4 show highest pressures

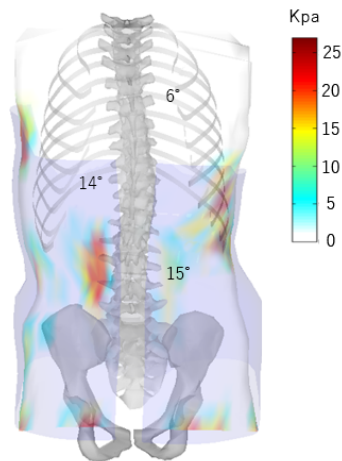


FIGURE 4. SIMULATED CORRECTION AND PRESSURE RESULTS OF BENCHMARK BRACE

of ± 25 Kpa near the apex of the spinal curve, this is the region where most correction is needed. Other higher-pressure regions occur at the opposite side of this apex, on the left and right bottom part of the brace, and in the frontal region on the abdomen. The latter of which is regarded unnecessary and should be minimized as it provides a load orthogonal to the desired correction direction. The pressure maps show that transmitting correctional loads to the spine is done through predominantly hard-tissue regions in the torso. Loads applied on the primarily soft-tissue region are distributed via organs over larger regions of the spine. These larger load distributions result in less correction control of the spine. Furthermore the pressure on the soft-tissue region and inferior organs can be very uncomfortable and should therefore be minimized.

The primarily soft-tissue region is situated between vertebrae L5-T10 as shown in Figure 1.

II_B - MOTION ANALYSIS

The motion characteristics define the desired compliance that should accomplish the functional requirement "facilitate motion".

In previous work by Dries [10], the contribution of different spinal regions to primary bends and the different loci about which particular vertebrae are rotating, were researched for both healthy subjects and scoliosis patients.

Dries showed that for both investigated groups (N=15), the largest portion of spinal deformation during basic motions (sagittal bending and lateral bending) is contributed by the region from vertebrae S1 to T10 (Scoliosis group 81.2%, Control group 87.3% for sagittal bends, Scoliosis group 55.7%, Control group 55.7% for lateral bends).

Contribution to bend tasks

Using the methods described by Dries [10], we are able to calculate the rotation angles and relative contribution of different spinal segments during primary bends, being sagittal bend tasks (flexion), lateral bend tasks and axial twists. Using these measurements, we identify the spinal segments where most motion is present during the primary bend tasks. The motion results of the Motion study patient have been scaled to the correction study patient and shown in table 2. During the sagittal bend, the lower regions of the spine (S1-T10) contribute to 82.4% of the total bend, while the higher regions (T10-T4) contribute for only 17.6%. For the lateral bend, these relative contributions are 73.4% for S1-T10 and 26.6% for T10-T4. For the axial twist motion, the lower region (S1-T10) provides 67.9% and the upper spinal region (T10-T4) contributes 32.1%.

TABLE 2. CONTRIBUTION TO PRIMARY BENDS FOR DIFFERENT SECTIONS OF THE SPINAL COLUMN. CONTRIBUTION IS GIVEN AS PERCENTAGE WITH STANDARD ERROR OF TOTAL BENDING TASK ANGLES.

Vertebra	Sagittal Bend	Lateral Bend	Axial Twist
T7-T4	4.6% \pm 4.6%	9.1% \pm 4.3%	30.8% \pm 16.1%
T10-T7	13.0% \pm 5.3%	17.5% \pm 4.3%	1.3% \pm 12.3%
L1-T10	30.1% \pm 1.7%	42.4% \pm 2.4%	44.5% \pm 15.9%
L3-L1	19.6% \pm 4.0%	22.3% \pm 3.5%	-2.7% \pm 7.1%
S1-L3	32.7% \pm 5.7%	8.7% \pm 1.0%	26.1% \pm 2.3%

Location of screws for lower spinal region

For the spinal region where most motion occurs during primary bends (S1-T10), a spatial motion analysis is performed using a custom made Matlab program to indicate the relative locations about which the vertebrae are rotating. Screws are calculated in the absolute normal planes, neglecting the out-of-plane motion caused by natural motion and imaging errors. [10] The screws of the lower lumbar region (L5-T10) have been averaged and normalized to the pelvis. The screw locations of the T10 vertebra are depicted in Figure 5 for the three primary bending tasks. Since no pitch is involved, the visualized screws are rotation axes. This means the three bending motions in can be simplified to pure rotations about the depicted axes for this patient.

The exact locations including confidence intervals of the average screw origins in the pelvis frame are depicted in Table 3.

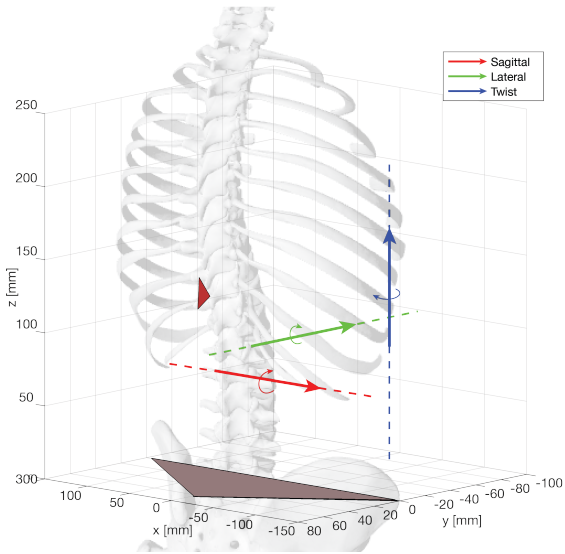


FIGURE 5. LOCATIONS OF GENERALIZED SCREW ROTATIONAL AXES DURING PRIMARY BEND TASKS FOR LOWER LUMBAR REGION (T10, RELATIVE TO PELVIS.)

TABLE 3. LOCATIONS OF AVERAGE SCREW ROTATIONAL AXES BETWEEN T10-S1 WITH RESPECT TO S1

	Sagittal Bend		Lateral Bend		Twist	
x	0	mm	-0.05 ± 9.8	mm	10.5 ± 30.0	mm
y	-14.2 ± 0	mm	0	mm	-81.4 ± 32.8	mm
z	63.6 ± 9.1	mm	97.6 ± 11.0	mm	0	mm

III - SEGMENT DIVISION

With the knowledge obtained by both the correction and the motion analysis the opportunity rises to reduce the complex biomechanical problem to an isolated spatial mechanism problem with quantified load and kinetic requirements. Both the ineffective correctional loads and the desired motion are situated in the soft-tissue region between vertebrae L5-T10. The regions that allow for effective correctional load transfer are the upper and lower hard-tissue regions (T10-T4 and region around Pelvis).

We propose a brace that applies loads in the hard-tissue regions and is compliant in the segment that spans the soft-tissue region.

The loads will be applied by an upper and lower correctional segment which are in contact with the predominantly hard-tissue

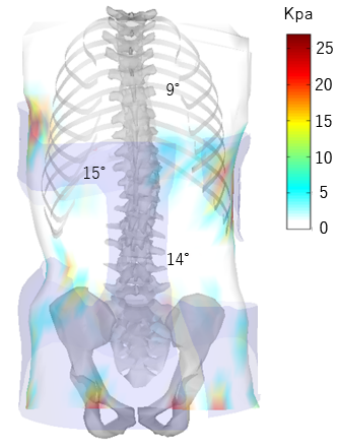


FIGURE 6. SIMULATED CORRECTION RESULTS OF POTENTIALLY COMPLIANT BRACE

regions. The two correctional segments are connected by a middle compliant segment that spans the predominantly soft-tissue regions without skin-contact. In the final design, the compliant segment will transmit the required loads while allowing motion during daily activities.

IV - ISOLATED SEGMENT ANALYSIS

The desired kinematic design specifications of the compliant segment are derived from a isolated segment of a modified benchmark brace. The in-brace correction profile and pressure results of the modified benchmark static brace are shown in Figures 6 and 7.

The modified static brace obtains similar correction as the original brace. Validation in BraceSim shows that the modified benchmark brace reduces the Cobb angle by ± 11 degrees. Figures 6 and 7 compared with Figures 3 and 4 show that the modified benchmark brace results in a similar reduction of the Cobb angle (± 1 degree) and lower peak pressures are apparent on the skin of the patient.

The modified benchmark brace spans the compliance region with a temporary stiff segment, which is isolated as can be seen in Figure 8. The transmitted loads and the resulting deformation of the temporary stiff segment define the kinematic design specifications of the to be designed compliant segment.

Isolated Segment Simulation

A finite element model of the isolated temporary stiff segment is analyzed in ANSYS and post-processed in Matlab. We determine the loads transmitted by the temporary stiff segment spanning the compliance region. Any compliant mechanism that transmits these loads, while resulting in the same in-brace relative location of the upper and lower correction segment is a suit-

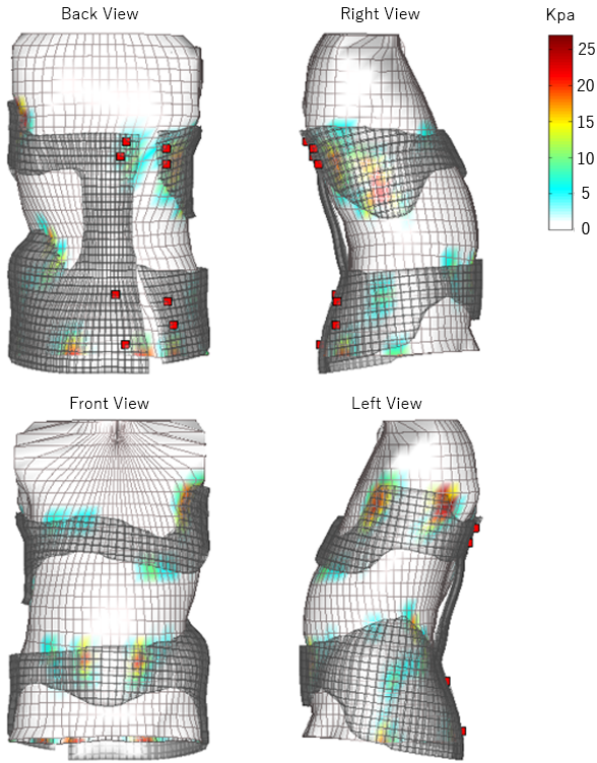


FIGURE 7. POTENTIALLY COMPLIANT BRACE INCLUDING PRESSURES

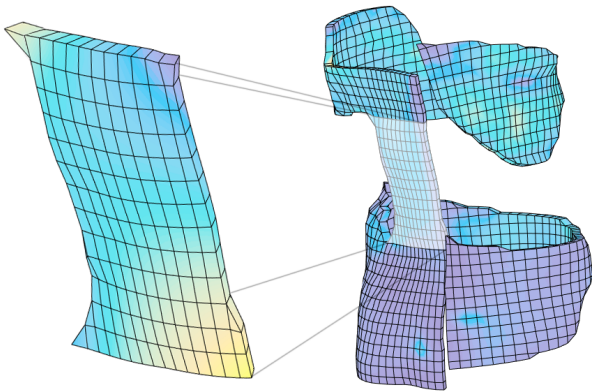


FIGURE 8. FINITE ELEMENT MODEL ISOLATED TEMPORARY STIFF SEGMENT

able substitution compliant mechanism. This includes a compliant mechanism with added desired compliance directions based on the motion study. The relative location is determined by subtracting the average node location of the lower edge from the upper edge in the in-brace configuration. The moments are determined around the average node location of the lower edge.

The transmitted loads and relative locations are given in table 4.

TABLE 4. KINETIC REQUIREMENTS

Axis	F	M	δ_{UE-LE}
x	3.44 N	0.02 Nm	$3.04 \cdot 10^{-02} m$
y	0.51 N	0.55 Nm	$4.86 \cdot 10^{-04} m$
z	3.31 N	0.12 Nm	$1.27 \cdot 10^{-01} m$

V - DESIGN SPECIFICATION

The design specifications are based on the motion study and the temporary stiff segment FEM analysis results. The quantitative design specifications apply to the compliant segment that will substitute the temporary stiff segment of the modified benchmark brace. The temporary stiff segment FEM analysis determines the required loads and deformations. The motion study determined the desired compliance axes of the compliant segment. The complex bio-mechanical problem is reduced to an isolated mechanical problem with clear kinematic design specifications, which consists of average screw locations and kinematic requirements. These quantified results are shown in Tables 3, 4.

DISCUSSION

The goal of this research was to quantify the functional requirements for the design of a compliant scoliosis brace and translate them into design specifications. The strategy presented uses motion analysis of a scoliosis patient and correction analysis of an original non-compliant scoliosis brace to form these design specifications. A brace design based on the presented design specifications can be validated in terms of correction efficiency using BraceSim and compared with the original non-compliant brace design as presented in Figure 4.

The strategy presented in this paper is a new approach to convert qualitative functional requirements into quantitative design specification.

Previous research into compliant scoliosis braces utilizing compliant shell mechanisms did not account for brace-tissue interaction [6], where this strategy does using BraceSim results. We have analyzed the spinal motions of a scoliosis patient and shown what different vertebra contribute to the total motion, and about which twist axes these motions occur. This analysis was performed for the absolute body planes, eliminating out-of-plane motions which can be caused by natural motions or imaging errors.

Ideally the braced correction study patient should have been studied to allow for an exact design of a compliant brace, which can be validated using BraceSim and this patients X-rays and

bodyscan. We reduce these differences by analyzing a patient with a similar Cobb angle and scoliotic progression as the correction study patient, without taking into account the angle of kyphosis or lordosis, and scaling the results to match the body length of the correction study patient. More research is needed to analyze possible differences in motion characteristics between scoliosis patients with similar Cobb angles and scoliotic progression.

The correctional loads needed for correcting the braced correction study patient have been analyzed using FEM analysis of a brace designed by an certified orthotist, and provide clear specifications for the design of compliant elements together with the compliance axes found in the motion studies. In future work it will be beneficial to model the edges of the temporary stiff segment as rigid, to ensure similar boundary conditions for the isolated temporary stiff element edges.

With the presented approach the required correctional loads are found in the patients non-deformed position. As a compliant brace design allows for motion, the required correctional loads in bent positions should be researched.

Currently, not many synthesis methodology are available in literature to generate concepts for compliant mechanism design. Using such a synthesis method one should be able to use the presented quantitative design specifications and translate them into spatial mechanisms allowing for compliant brace designs, which can be validated in terms of correction efficiency using BraceSim.

CONCLUSION

This paper introduced a strategy to reduce the complexity of a bio-mechanical problem into an isolated mechanical problem. The main qualitative functional requirements have been converted into quantitative design specifications for a spatial compliant mechanism. The explained strategy was proven feasible on the basis of an example patient. Using this method, generated concepts can be validated on correctional efficiency using BraceSim software. Further work should be focused on exploring and testing actual brace designs and the generalization of patient motion data.

ACKNOWLEDGMENT

The authors gratefully acknowledge NSF No. IIS - 1527133 as well as STW (HTSM-2012 12814: ShellMech) for their financial support of this project. The writers would also like to thank professor dr. Christiane Cauoette, Nikita Cobetto, PhD and prof. dr. Carl-Éric Aubin of the École Polytechnique de Montréal for collaborating and providing acces to BraceSim.

REFERENCES

- [1] Deacon, P., Flood, B. M., and Dickson, R. a., 1984. "Idiopathic scoliosis in three dimensions. A radiographic and morphometric analysis.". *The Journal of bone and joint surgery. British volume*, **66**(4), pp. 509–512.
- [2] Weinstein, S. L., Dolan, L. A., Wright, J. G., and Dobbs, M. B., 2013. "Effects of bracing in adolescents with idiopathic scoliosis.". *The New England journal of medicine*, **369**(16), pp. 1512–21.
- [3] Nachemson, A. L., Lonstein, J. E., and Weinstein, S. L., 1982. "Report of the Prevalence and Natural History Committee of the Scoliosis Research Society.". In Denver: Scoliosis Research Society.
- [4] Asher, M. A., and Burton, D. C., 2006. "Adolescent idiopathic scoliosis: natural history and long term treatment effects.". *Scoliosis*, **1**(1), p. 2.
- [5] Rigo, M., and Weiss, H.-R., 2008. "The Cheneau Concept of Bracing - Biomechanical Aspects". *The Conservative Scoliosis Treatment*, **135**, pp. 303–319.
- [6] Nijssen, J. P. A., 2017. "Design and Analysis of a Shell Mechanism Based Two-fold Force Controlled Scoliosis Brace". Master's thesis, Delft University of Technology.
- [7] Ring, J. B., Kim, C. J., Evans, J., and Beal, C., 2017. "A Passive Brace for the Treatment of Scoliosis Utilizing Compliant Mechanisms". Master's thesis, Bucknell University, Lewisburg PA.
- [8] Bulthuis, G. J., Veldhuizen, A. G., and Nijenbanning, G., 2008. "Clinical effect of continuous corrective force delivery in the non-operative treatment of idiopathic scoliosis: a prospective cohort study of the triac- brace". *European Spine Journal*, **17**(2), pp. 231–239.
- [9] Desbiens-Blais, F., Clin, J., Parent, S., Labelle, H., and Aubin, C.-E., 2012. "New brace design combining cad/cam and biomechanical simulation for the treatment of adolescent idiopathic scoliosis". *Clinical biomechanics*, **27**(10), pp. 999–1005.
- [10] Dries, T. J., 2018. "A Biomechanical Characterization of Spinal Motion Data for the Design of a Compliant Scoliosis Brace". Master's thesis, Delft University of Technology, Delft, The Netherlands.
- [11] Richards, B. S., Bernstein, R. M., D'Amato, C. R., and Thompson, G. H., 2005. "Standardization of criteria for adolescent idiopathic scoliosis brace studies: SRS Committee on Bracing and Nonoperative Management.". *Spine*, **30**(18), sep, pp. 2068–75; discussion 2076–7.

Characterization Theory

Paper: Unified Stiffness Characterization of Non-Linear Compliant Shell Mechanisms

This paper is submitted to the ASME Journal of Mechanisms and Robotics (JMR). The paper is reviewed and recommended for publication as a research paper pending revision.

The paper is an extension on the paper included in Appendix A: "Unified Rotational and Translational Stiffness Characterization of Compliant Mechanisms" written by the same authors Leemans, Kim, van de Sande and Herder and will be published at the ASME 2018 International Design Engineering Technical Conferences & Computers and Information in Engineering Conference IDETC/CIE 2018.

Unified Stiffness Characterization of Non-Linear Compliant Shell Mechanisms

Joost R. Leemans¹, Charles J. Kim², Werner W.P.J. van de Sande¹ and Just L. Herder¹

¹*Department of Precision and Microsystems Engineering, Delft University of Technology*

²*Department of Mechanical Engineering, Bucknell University*

Compliant shell mechanisms utilize spatially curved thin-walled structures to transfer or transmit force, motion or energy through elastic deformation. To design with spatial mechanisms designers need comprehensive non-linear characterization methods, while existing methods fall short of meaningful comparisons between rotational and translational degrees of freedom. This paper presents two approaches, both of which are based on the principle of virtual loads and potential energy, utilizing properties of screw theory, Plücker coordinates and an eigen-decomposition, leading to two unification lengths that can be used to compare and visualize all six degrees of freedom directions and magnitudes of non-linear behaving mechanisms in a non-arbitrary physically meaningful manner.

1 Introduction

The spatial geometry of compliant shell elements makes them useful as building blocks for spatial mechanism design. Researching the behaviour of compliant shell elements is done both analytically, as can be seen in the work of Sefen [1] Pellegrino [2] and computationally as can be seen in work of Radaelli & Herder [3] [4]. The difficulty of characterizing compliant shell mechanisms lies in the intertwined kinematics and kinetics. Furthermore, the freedom and constraint directions change in a non-linear fashion while subjected to large deformations.

To design mechanisms designers need insight into their kinematics. In the field of rigid body mechanisms this is often characterised by the exact degrees of freedom describing the constraint and free motion directions. Compliant shell mechanisms do not have clear distinctive constraint and free motion directions, since motion tendencies are determined by the relative compliance of the mechanisms.

In order to characterize compliant shell mechanisms we shall discuss the relative compliances of the kinematic degrees of freedom, for spatial compliant mechanisms defined by Nijssen [5] as,

"The motion tendency of a mechanism in 3D space, defined by the relationship between the three rotational and three translational compliances"

Relative compliances refer to the compliance ratios between the relative kinematic degrees of freedom. From here on referred to as the degrees of freedom. Determining and utiliz-

ing these degrees of freedom has proven useful in the characterization and synthesis of spatial mechanisms [4] [5] [6].

In related work, different methods are used to characterize the degrees of freedom of compliant mechanisms. Existing methods do not address the coupling between translations and rotations and thus discuss the rotations and translation separately, for example, by using compliance ellipsoids [4]. Methods to characterize principal compliance axes while including coupling were first introduced by Lipkin & Patterson [7], utilizing Plücker coordinates. Lin [8] introduced an independent derivation of principal compliance axes using hybrid coordinates. Two incomparable principle rotational and translational compliance directions and corresponding magnitude multiplier groups, containing all six degrees of freedom result from Lin and Lipkin's derivation. A full comparison and order of the six degrees of freedom would give deeper insight into kinematic characteristics, such as the determination of whether a mechanism is predominantly rotational or translational compliant. Methods to convert these multiplier groups into compatible units, introduce arbitrarily defined characteristic lengths [9], lacking a physical consistent meaning. This leads to non-robust solutions, since this arbitrarily chosen length represents a different physical distance per analysis. Consequently the resulting unified compliances are not comparable between mechanisms.

A method with comparable results to a section of this paper is introduced by Lin [8]. Lin's derivation is based on a geometrical interpretation of hybrid coordinates to derive principal stiffness axes. The corresponding stiffnesses are converted to similar units based on the principle of potential energy. By introducing the principle of potential energy all directional information is lost, since energy is a scalar quantity. Lin's method is used to optimize the gripping force of graspers, instead of characterizing non-linear compliant mechanisms.

This paper presents two approaches that utilize properties of screw theory, Plücker coordinates and Lipkin's eigen-decomposition which lead to unified compliances. The unified compliances, consisting of two multiplier groups with identical units, facilitates a comparison between all six degrees of freedom compliance magnitudes in a non-arbitrarily insightful manner while including coupling. The unification is utilized in a spatial characterization of non-linear behaving compliant mechanisms.

After the introduction the paper continues, in Section 2, with background theory on Plücker coordinates, stiffness matrices and Lipkin's eigen-decomposition. Section 3 visu-

alises Lipkin's eigen-decomposition. The background theory and visualisation are used to determine two approaches that lead to the unification of the compliances in Section 4. The unification is used to present a visual characterization of the kinematic behaviour of two well-known compliant flexure mechanisms as illustrated in Section 5. After that, in Section 6, the characterisation is used to analyse the non-linear behaviour of compliant shell mechanisms. Section 7 discusses the contribution made by this paper. A brief summary is given and a general conclusion is drawn in Section 8.

2 Background

According to Chasles' theorem [10] a displacement in three-dimensional space can be expressed in Plücker coordinates vector form as a twist \mathbf{T} containing linear $\vec{\delta}$ and angular $\vec{\gamma}$ displacements defined as,

$$\mathbf{T} = \begin{bmatrix} \vec{\delta}_i \\ \vec{\gamma}_i \end{bmatrix} = \begin{bmatrix} (\vec{r}_i \times \vec{\gamma}_i) + h_i \vec{\gamma}_i \\ \vec{\gamma}_i \end{bmatrix}, \quad i = 1, 2, 3 \quad (1)$$

This form expresses the translation in terms of a combination of angular displacement $\vec{\gamma}$ and the 3×1 location vector \vec{r}_i and h the pitch scalar. The Plücker coordinates in vector form are visualised in Figure 1

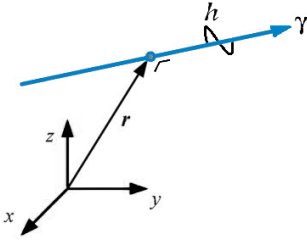


Fig. 1: Visual representation of the Plücker coordinates in vector form

The magnitude of the twist is defined as,

$$|\mathbf{T}| = \begin{cases} \sqrt{\vec{\delta} \cdot \vec{\delta}} & \text{if } \gamma = 0 \\ \sqrt{\vec{\gamma} \cdot \vec{\gamma}} & \text{otherwise} \end{cases} \quad (2)$$

and the direction of the twist is defined as the direction of the angular deformation. The dual of Chasles' theorem is Poincot's theorem. It states that any wrench can be constructed by a force and torque along the same axis [11]. In Plücker coordinate vector form the wrench \vec{w} contains the linear forces \vec{f} and the moment couples $\vec{\tau}$ defined as,

$$\mathbf{w} = \begin{bmatrix} \vec{f}_i \\ \vec{\tau}_i \end{bmatrix} = \begin{bmatrix} \vec{f}_i \\ (\vec{b}_i \times \vec{f}_i) + d_i \vec{f}_i \end{bmatrix}, \quad i = 1, 2, 3 \quad (3)$$

where \vec{b}_i is the 3×1 location vector pitch d_i is the ratio of angular torque to linear force. The magnitude of the wrench is defined as,

$$|\mathbf{w}| = \begin{cases} \sqrt{\vec{\tau} \cdot \vec{\tau}} & \text{if } f = 0 \\ \sqrt{\vec{f} \cdot \vec{f}} & \text{otherwise} \end{cases} \quad (4)$$

and the direction of the wrench is seen as the direction of the force.

The relationship between the displacement and load of a specific point of interest can be described by the secant stiffness matrix \mathbf{K}_s or its inverse, the secant compliance matrix \mathbf{C}_s respectively, expressed as

$$\vec{w} = \mathbf{K}_s \Delta \vec{T}, \quad \Delta \vec{T} = \mathbf{C}_s \vec{w} \quad (5)$$

where \mathbf{K}_s and \mathbf{C}_s are the 6×6 secant stiffness and secant compliance matrix and $\Delta \vec{T}$ is an incremental displacement step. A secant matrix describing an infinitesimal incremental step is known as the tangent matrix, and it is defined as

$$\mathbf{K}_t = \lim_{\Delta \vec{T} \rightarrow 0} \mathbf{K}_s, \quad \mathbf{C}_t = \lim_{\Delta \vec{T} \rightarrow 0} \mathbf{C}_s \quad (6)$$

The tangent matrices describe a linearised configuration-dependant relation between the displacement and the load. The tangent stiffness and compliance matrices are composed of a physical and geometrical stiffness and compliance matrix. Non-linear behaviour can be analysed by using either the secant stiffness matrix or by making an incremental linearised analysis of each quasi-static-equilibrium based on the tangent stiffness matrix.

Any symmetric positive definite non-singular tangent stiffness \mathbf{K}_t and tangent compliance matrix \mathbf{C}_t can be decomposed into an eigen-system as described by Lipkin & Patterson [7]. The eigen-decomposition describes three translational and three rotational principal axes, with corresponding stationary multiplier values of the translational and rotational stiffness. Lipkin's eigen-decomposition of the tangent stiffness matrix \mathbf{K}_t is defined as,

$$\mathbf{K}_t = [\hat{\mathbf{w}}_f \ \hat{\mathbf{w}}_\gamma] \begin{bmatrix} k_f & 0 \\ 0 & k_\gamma \end{bmatrix} \begin{bmatrix} \hat{\mathbf{w}}_f \\ \hat{\mathbf{w}}_\gamma \end{bmatrix} \quad (7)$$

and the resulting tangent compliance matrix eigen-decomposition is defined as,

$$\mathbf{C}_t = [\hat{\mathbf{T}}_f \ \hat{\mathbf{T}}_\gamma] \begin{bmatrix} a_f & 0 \\ 0 & a_\gamma \end{bmatrix} \begin{bmatrix} \hat{\mathbf{T}}_f \\ \hat{\mathbf{T}}_\gamma \end{bmatrix} \quad (8)$$

where for $i = 1, 2, 3$ multipliers $k_{\gamma_i} > 0$ are the angular stiffnesses in the directions of the γ_i , multipliers $k_{f_i} > 0$ are the

translational stiffnesses in the directions of the f_i . The inverse of a translational stiffness gives the translational compliance,

$$a_{f_i} = \frac{1}{k_{f_i}} \quad (9)$$

and the inverse of a rotational stiffness gives the rotational compliance,

$$a_{\gamma_i} = \frac{1}{k_{\gamma_i}} \quad (10)$$

\mathbf{w}_f are the eigen-wrenches, these directions are also known as the wrench axes, defined as

$$\mathbf{w}_{f_i} = \begin{bmatrix} \vec{f}_i \\ \vec{\tau}_i \end{bmatrix}, \quad i = 1, 2, 3 \quad (11)$$

Applying an eigen-wrench \mathbf{w}_{f_i} leads to an induced twist \mathbf{T}_{f_i} a pure translational displacement parallel to the force direction \vec{f}_i , the induced twists \mathbf{T}_f are defined as

$$\mathbf{T}_{f_i} = \begin{bmatrix} a_{f_i} \vec{f}_i \\ 0 \end{bmatrix}, \quad i = 1, 2, 3 \quad (12)$$

\mathbf{T}_γ are the eigen-twists, these directions are also known as the twist axes, defined as

$$\mathbf{T}_{\gamma_i} = \begin{bmatrix} \vec{\delta}_i \\ \vec{\gamma}_i \end{bmatrix}, \quad i = 1, 2, 3 \quad (13)$$

Applying an eigen-twist \mathbf{T}_{γ_i} leads to an induced wrench \mathbf{w}_{γ_i} a pure moment parallel to the rotational direction $\vec{\gamma}_i$, the induced wrenches \mathbf{w}_γ are defined as

$$\mathbf{w}_{\gamma_i} = \begin{bmatrix} 0 \\ k_{\gamma_i} \vec{\gamma}_i \end{bmatrix}, \quad i = 1, 2, 3 \quad (14)$$

The above wrenches and twists are normalized with respect to the defined magnitudes to be used in the eigen-decompositions of Equations 7 and 8.

$$\hat{\mathbf{T}} = \frac{\mathbf{T}}{|\mathbf{T}|} \quad (15)$$

and

$$\hat{\mathbf{w}} = \frac{\mathbf{w}}{|\mathbf{w}|} \quad (16)$$

After the normalization of the twist and wrench eigen-decomposition described in Equations 2 and 4, the direct magnitude relation is lost. In terms of magnitude, the induced twists and wrenches are no longer a direct result of the eigen-wrenches and eigen-twists. After normalization, only the directional relations remain valid.

3 Visualisation of the Eigen-Decomposition

To increase the understanding of the wrench and twist axes the eigen-decompositions is visualised. Nijssen [6] already plotted the three eigen-twist directions. In this section we introduce the visualisation of the eigen-wrench directions and include the corresponding stationary compliance multipliers. A compliant shell mechanism example is introduced which is fully constrained along the bottom edge and the point of interest at which C_i is determined is indicated by a black dot, as can be seen in Figure 2.

The acrylic-plastic shell mechanism is analysed as an IGA shell, with the following material properties; the Young Modulus is 3.2 GPa, the Poisson ratio is 0.35. The 2mm thick geometry is defined by NURBS [12], a third polynomial follows a 3×5 grid. Five coordinates are placed on three planes in $y = -0.05$, $y = 0$ and $y = 0.05$. The x and z coordinates are defined in Table 8.

Table 1: NURB coordinates corrugated shell

Point	1	2	3	4	5
x	0.00	0.00	0.04	0.00	0.00
z	0.00	0.04	0.08	0.11	0.15

The three principle eigen-twist directions are shown in Figure 2a. A rotation of the point of interest around a twist axis plus a translation along this axis leads to pure parallel moments around this twist axes.

The three principle eigen-wrench directions can be seen in Figure 2b. A force along a wrench axis plus a moment around this axis leads to a pure translation along the wrench axis.

Figures 2a and 2b both provide information on the twist and wrench spatial directions, while excluding the compliance and stiffness multipliers. Thus these figures do not show the magnitude of compliance corresponding to these directions. By plotting vectors along the directions of the wrench and twist axes with the length of their corresponding stationary compliance multipliers, both the direction and magnitude of compliance are visualised in an intuitive manner.

Figure 2c shows the vectors along the twist axes with the magnitude of the corresponding rotational compliance multipliers a_γ . The longer the vector the larger the rotational compliance around the twist axis that the vector represents.

Figure 2d shows the vectors along the wrench axes with the magnitude of the corresponding translational compliance

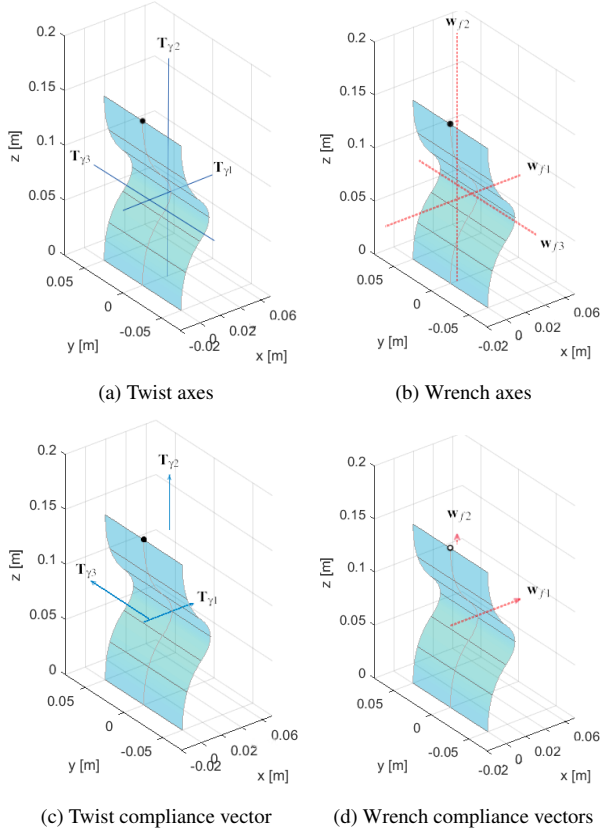


Fig. 2: Visual representation eigen-decomposition

multipliers a_f . The longer the vector the larger the translational compliance along the wrench axis that the vector represents.

Figures 2d and 2c both provide the directional information of the twist and wrench axes and the corresponding compliance magnitude. In itself these are useful characterizations, however, the magnitudes of these vectors cannot be compared between the two Figures, as further discussed in Section 4.

4 Unification methods

The diagonal matrices of the decompositions in Equations 7 and 8 consist of the compliance and stiffness stationary multipliers corresponding to the wrench and twist axes. Considering the decomposition in Equation 8, the upper three stationary multipliers a_f are the translational compliances given as length per force, corresponding to a translation parallel to the wrench axis. The lower three stationary multipliers a_γ are the rotational compliances given as angle divided by force multiplied by length, corresponding to the rotation around the twist axis. The rotational and translational multipliers are not directly comparable due to their different units. To enable this comparison, we utilize unification variables, which will be defined based on equivalent compliance by virtual load or potential energy.

We will discuss two unification approaches, by convert-

ing the units of a_{f_i} into a_{γ_i} and the units of a_{γ_i} into a_{f_i} . The conversion of the units of a_{γ_i} into a_{f_i} can be done by expressing rotational compliance as an equivalent translational compliance at the point of interest using a unification length χ_i . The conversion of the units of a_{f_i} into a_{γ_i} can be done by expressing translational compliance at the point of interest as an equivalent rotational compliance using a unification length Ψ_i . In Equation form the unification approaches are given as,

$$\tilde{a}_{f_i} = \chi_i^2 a_{\gamma_i} \quad (17)$$

and,

$$\tilde{a}_{\gamma_i} = \frac{a_{f_i}}{\Psi_i^2} \quad (18)$$

We introduce two methods to obtain the unification lengths. The first method utilizes virtual load and displacements and the second method is based on the principle of potential energy. The strengths and weaknesses of both methods are discussed in Section 4.3.

4.1 RasT: Rotational as equivalent Translational compliance

The first approach expresses rotational compliance as an equivalent translational compliance at the point of interest. We call this the RasT approach. Both the virtual loads and potential energy are used separately to determine unification length χ_i .

4.1.1 Virtual load method

Converting the rotational compliance into an equivalent translational compliance at the point of interest using the virtual load method can be done in three consecutive steps.

- I Express δ_{eq_i} , an equivalent translation at the point of interest in terms of rotation around the twist axis.
- II Express F_{eq_i} , an equivalent virtual force at the point of interest in terms of the induced counteracting pure parallel moment couple corresponding to a rotation around the twist axis.
- III Express an equivalent translational compliance \tilde{a}_{f_i} , by dividing the expressions above to obtain the equivalent translational compliance. That is,

$$\tilde{a}_{f_i} = \frac{\delta_{eq_i}}{F_{eq_i}} \quad (19)$$

Figures 3 and 4 both show the point of interest of a spatial compliant mechanism as indicated by the black dot and one of the three principal twist axes \mathbf{T}_{γ_i} indicated by the blue line, used to explain the three steps.

Step I: Express δ_{eq_i} , equivalent translation. The equivalent translation at the point of interest is expressed in terms of a screw around the twist axis. The total translation corresponding to a rotation θ_i is a combination of displacement along the arc length around the twist axis δ_{ri} and a translation along the twist axis δ_{hi} . The resulting equivalent translation δ_{eq_i} , a path along a cylinder, is illustrated in Figure 3.

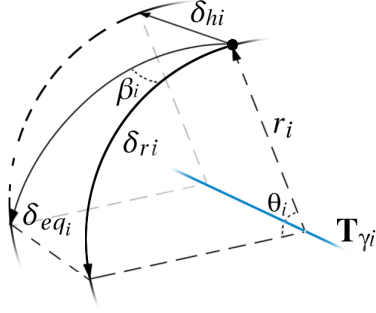


Fig. 3: Equivalent translation geometry

The displacement along the arc at a radius can be expressed as the rotation multiplied by the radius, the arc-length. The radius that defines the displacement along the arc is the shortest distance between the point of interest and the twist axis. This length is defined in Plücker coordinates as the location vector r_i as shown in Figure 1. The displacement along the arc-length is thus given as,

$$\delta_{ri} = |r_i|\theta_i \quad (20)$$

The point of interest translates along the twist axis, due to the pitch h_i , given by the pitch times the rotation,

$$\delta_{hi} = h_i\theta_i \quad (21)$$

The resulting displacement due to the two perpendicular displacements on a cylinder is calculated using the Pythagorean theorem. The equivalent translation expressed in terms of the corresponding rotation is thus given as,

$$\delta_{eq_i} = \sqrt{(h_i^2 + |r_i|^2)}\theta_i \quad (22)$$

Step II: Express F_{eq_i} , equivalent virtual force. The equivalent virtual force at the point of interest in the opposite direction of the equivalent displacement is expressed in terms of the induced moment corresponding to a rotation around the twist axis.

This is done by defining a virtual force F_m at distance r_i with a magnitude and direction which results in the same moment magnitude as the pure moment parallel corresponding to a rotation. By decomposing this virtual moment force vector, with one of the components in the direction of the

equivalent translation determined in step I, the equivalent virtual force F_{eq} can be defined. The introduced virtual moment force vector F_m is given as,

$$F_m = \frac{M_i}{|r_i|} \quad (23)$$

The geometry required to decompose the virtual moment force F_m to the equivalent virtual force F_{eq} in the opposite direction of the point of interest displacement is shown in Figure 4.

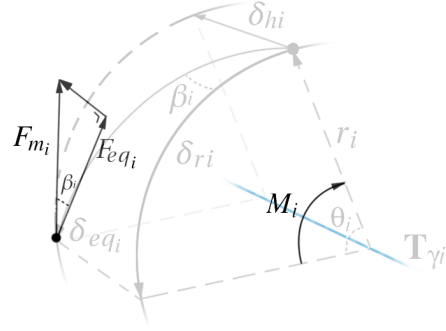


Fig. 4: Equivalent virtual force geometry

where β is the angle between δ_{eq_i} and δ_{γ_i} , since the alternate interior angles between two parallel lines are equal, β_i also defines the angle between F_m and F_{eq_i} , which is defined as,

$$\beta_i = \frac{F_m}{F_{eq_i}} = \frac{\delta_{eq_i}}{\delta_{\gamma_i}} = \frac{\sqrt{(h_i^2 + |r_i|^2)}\theta_i}{|r_i|\theta_i} \quad (24)$$

By combining Equation 23 and 24, the equivalent virtual force expressed in terms of the corresponding moment can be given as,

$$F_{eq_i} = \frac{M_i}{\sqrt{(h_i^2 + |r_i|^2)}} \quad (25)$$

Step III: Express \tilde{a}_{f_i} , the equivalent translational compliance. The third step is to substitute 22 and 25 with 19,

$$a_{f_i} = \frac{\delta_{eq_i}}{F_{eq_i}} = (h_i^2 + |r_i|^2) \frac{\theta_i}{M_i} \quad (26)$$

The unification length χ_i follows from Equation 17 and 26,

$$\chi_i = \sqrt{h_i^2 + |r_i|^2} \quad (27)$$

4.1.2 Potential energy method

To unify the rotational compliance multipliers a_{γ_i} into equivalent translational compliance multipliers \tilde{a}_{f_i} the principle of potential energy can be used as well. The rotational energy is compared with the corresponding virtual equivalent translational energy due to the rotation.

The eigentwist induces a pure moment around the twist axis, therefore the corresponding potential energy is solely dependent on the rotational stiffness and rotation. The potential energy of the eigentwist is defined as,

$$U_{\gamma_i} = \frac{1}{2} k_{\gamma_i} \theta_i^2 \quad (28)$$

By introducing an equivalent translational stiffness \tilde{k}_{f_i} and the equivalent translation $\delta_{e_{q_i}}$ corresponding to the rotation given in Equation 22, we can express the stored energy as,

$$\frac{1}{2} k_{\gamma_i} \theta_i^2 = \frac{1}{2} \tilde{k}_{f_i} \delta_{e_{q_i}}^2 \quad (29)$$

By substituting Equation 22 with 29 the equivalent translational stiffness can be defined as,

$$\tilde{k}_{f_i} = \frac{k_{\gamma_i}}{(h_i^2 + |r_i|^2)} \quad (30)$$

The inverse of the translational and rotational stiffness results in the translational and rotational compliance, as stated in Equation 9 and 10. The equivalent translational compliance of the rotational compliance is thus given as,

$$\tilde{a}_{f_i} = (h_i^2 + |r_i|^2) a_{\gamma_i} \quad (31)$$

From 17 and 31 follows the unification length.

$$\chi_i = \sqrt{h_i^2 + |r_i|^2} \quad (32)$$

which exactly matches Equation 27.

4.2 TasR: Translational as equivalent Rotational compliance

The second approach expresses the translational compliance as an equivalent rotational compliance, which we call the TasR approach. Converting the translational compliance into an equivalent rotational compliance at the point of interest can be done using both the TasR equivalent of the virtual load and the potential energy RasT approach. The virtual load method TasR equivalent steps are:

- I Express $\theta_{e_{q_i}}$, an equivalent rotation at the point of interest in terms of a translation parallel to the wrench axis.
- II Express $M_{e_{q_i}}$, an equivalent virtual moment at the point of interest in terms of the counteracting force corresponding to a translation parallel to the wrench axis.

- III Express an equivalent rotational compliance \tilde{a}_{γ_i} , by dividing the expressions above to obtain the equivalent translational compliance.

The potential energy method TasR equivalent is done by introducing an equivalent rotational stiffness. This stiffness is defined in terms of the translational stiffness corresponding to the wrenches.

Both the virtual load and the potential energy TasR equivalent of the RasT methods result into the unification length,

$$\psi_i = \sqrt{|d_i^2| + b_i^2} \quad (33)$$

which has the same form as the unification length expressed in Equation 32.

4.3 Approach and method comparison

Both the virtual load method and the potential energy method result into the same unification lengths. The potential energy method is more straightforward, however, it gives less insight into the actual kinematics compared to the virtual load method. While the end results of both methods yield similar conclusions, the virtual load method includes interesting sub-steps with physical relevance. The sub-step results in themselves can form the basis for specific designs. Knowledge of the composition of the sub-steps provides the opportunity to vary parameters in an intelligent manner to achieve specific objectives. In addition, energy in any form is a scalar quantity. Using the introduced potential energy method all directional information is excluded.

The RasT unification approach characterizes a mechanism as if a point of interest will be displaced using solely forces. The RasT approach is physically comparable as if the point of interest is displaced, along the wrench and around the twist axis, using a ball-and-socket-joint while evaluating the travelled path and the reaction force. Consequently using the RasT approach pure decoupled rotations around the point of interest are impossible to excite, therefore the RasT approach cannot evaluate the corresponding compliance multipliers. The TasR approach characterizes a mechanism as if the less intuitive opposite is the case, when a point of interest will be displaced solely using torques. Consequently using the TasR approach the unified compliance values corresponding to eigen-wrenches that are pure forces in line with the point of interest cannot be evaluated.

In order to bypass degrees of freedom that are non-evaluable one could use either the TasR or RasT approach. If both approaches result in non-evaluable degrees of freedom magnitudes the combination of the two will give the best characterization. The RasT approach is more intuitive and accounts for the coupling of the rotations and translations by including twist pitch, hence Sections 5 and 6 will focus on this approach. However, both approaches in their context, separately or combined, are a powerful characterization for comparing all six degrees of freedom.

5 Characterization

This Section shows the effectiveness and strength of the ability to characterize and compare all six degrees of freedom using the unification lengths.

5.1 Unified compliance matrix

The unification lengths χ_i and Ψ_i result in unified stationary compliance multipliers, which can be represented in matrix form. In the case of the RasT approach, the unification length of Equation 27 is substituted with Equation 8. The rotational compliance multipliers are multiplied by the unification length squared ($h_i^2 + |r_i|^2$), which results in the equivalent translational compliance. In matrix form this produces the diagonal unified stationary translational compliance multiplier matrix $\tilde{\mathbf{a}}_f$ given as,

$$\tilde{\mathbf{a}}_f = \begin{bmatrix} a_{fi} & 0 \\ 0 & (|r_i|^2 + h_i^2)a_{\gamma i} \end{bmatrix} \quad (34)$$

In the case of the TasR approach, the unification length of Equation 33 substituted with Equation 8 the unified rotational compliance multiplier matrix $\tilde{\mathbf{a}}_\gamma$ is given as,

$$\tilde{\mathbf{a}}_\gamma = \begin{bmatrix} \frac{a_{fi}}{|b_i|^2 + d_i^2} & 0 \\ 0 & a_{\gamma i} \end{bmatrix} \quad (35)$$

To put it in the original context, the complete eigen-decomposition of the tangent compliance matrix, including the new unified compliance matrix for the RasT approach becomes,

$$C_t = [\hat{\mathbf{T}}_f \hat{\mathbf{T}}_\gamma] \begin{bmatrix} I & 0 \\ 0 & \frac{1}{\sqrt{|r_i|^2 + h_i^2}} \end{bmatrix} \tilde{\mathbf{a}}_f \begin{bmatrix} I & 0 \\ 0 & \frac{1}{\sqrt{|r_i|^2 + h_i^2}} \end{bmatrix} \begin{bmatrix} \hat{\mathbf{T}}_f \\ \hat{\mathbf{T}}_\gamma \end{bmatrix} \quad (36)$$

and for the TasR approach the complete decomposition is given as,

$$C_t = [\hat{\mathbf{T}}_f \hat{\mathbf{T}}_\gamma] \begin{bmatrix} |b_i|^2 + d_i^2 & 0 \\ 0 & I \end{bmatrix} \tilde{\mathbf{a}}_\gamma \begin{bmatrix} |b_i|^2 + d_i^2 & 0 \\ 0 & I \end{bmatrix} \begin{bmatrix} \hat{\mathbf{T}}_f \\ \hat{\mathbf{T}}_\gamma \end{bmatrix} \quad (37)$$

5.1.1 Direction and unified compliance magnitude visualised

Vectors in the direction of the eigen-twists $\hat{\mathbf{T}}_i$ and the eigen-wrenches $\hat{\mathbf{w}}_i$ with the length of their corresponding values in the unified compliance matrix $\tilde{\mathbf{a}}_f$ or $\tilde{\mathbf{a}}_\gamma$ visualise the comparable compliance directions. Using this visualisation the dominant compliance directions become evident.

The power of this method is shown through two well-described compliant flexure mechanisms. The first is designed to be predominately rotationally compliant, a cross pivot flexure mechanism. The second designed to be predominately translationally compliant, a double

parallel flexure mechanism with an intermediate body. The visualisation using the unified compliance matrix confirms the expected behaviour of these well-described mechanisms.

Both mechanisms are analysed in SPACAR, which is a program for dynamic analysis of flexible spatial mechanisms and manipulators [13]. The mechanisms contain blue spring steel flexures with the following properties; the Young Modulus is 500 MPa, the Poisson ratio is 0.3 and the geometry is $75 \times 15 \times 0.5$ mm.

Cross pivot flexure mechanism

The cross pivot flexure mechanism consists of two perpendicular flexures and two parallel rigid bodies. The lower rigid body is fully constrained and the centre of the upper rigid body is considered to be the point of interest. Using SPACAR the 6x6 tangent compliance matrix C_t is determined. The introduced, in Section 3, visualisation of Lipkin's eigen-decomposition is applied. Figure 5 shows the twist and wrench compliant axes of the mechanism.

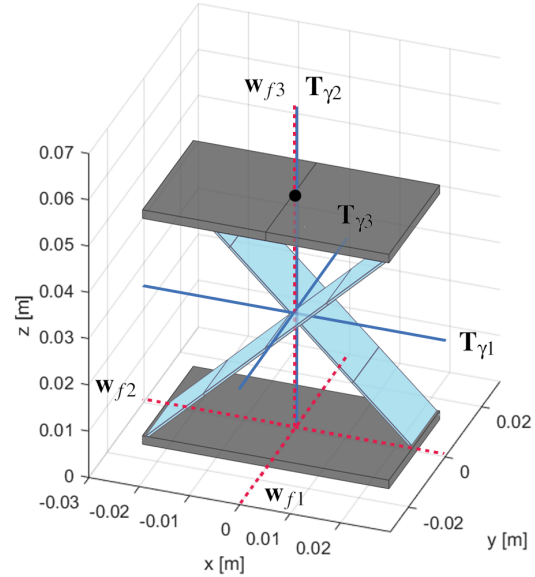


Fig. 5: Principal compliance directions of the cross pivot flexure mechanism

The stationary translational compliance multipliers corresponding to the wrench axes are given in Table 2.

Table 2: Compliance magnitudes and corresponding wrench axes of the cross pivot flexure

Corresp. wrench	Translational compliance [a_{fi}]
\mathbf{w}_{f1}	$2.50 \cdot 10^{-07}$ m/N
\mathbf{w}_{f2}	$2.00 \cdot 10^{-08}$ m/N
\mathbf{w}_{f3}	$2.00 \cdot 10^{-08}$ m/N

The largest translational compliance multiplier is underlined and corresponds to wrench \mathbf{w}_{f1} . The stationary rotational compliance multipliers and the pitches corresponding to the twist axes are given in Table 3.

Table 3: Compliance magnitudes and corresponding twist axes of the cross pivot flexure

Corresp. twist	Rotational comp. [a_{γ_i}]	Pitch [h_i]
$\mathbf{T}_{\gamma 1}$	$1.06 \cdot 10^{-03}$ rad/Nm	$7.50 \cdot 10^{-03}$ m
$\mathbf{T}_{\gamma 2}$	$1.06 \cdot 10^{-03}$ rad/Nm	$7.50 \cdot 10^{-03}$ m
$\mathbf{T}_{\gamma 3}$	<u>$4.80 \cdot 10^{-01}$ rad/Nm</u>	$0.00 \cdot 10^{-00}$ m

The largest rotational compliance multiplier is underlined and corresponds to twist axis $\mathbf{T}_{\gamma 3}$. As discussed the compliance multipliers in Tables 2 and 3 cannot be compared directly, therefore the unified compliance matrices are introduced. Figure 6 shows compliance vectors along the twist and wrench axes with unified compliance magnitudes \tilde{a}_f resulting from the RasT approach.

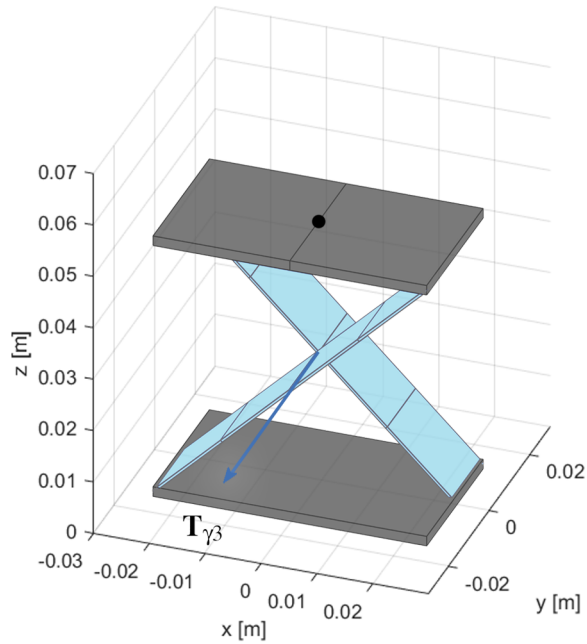


Fig. 6: Unified compliance vectors of the cross pivot flexure mechanism

As can be seen in Figure 6, the largest vector by orders of magnitude is in the direction of twist axis $\mathbf{T}_{\gamma 3}$ as is expected, originating from the crossing of the flexures in the y-direction parallel to these flexures. The other compliance vectors are too small to visualise using linear magnitude representation. The corresponding comparable unified compliance magnitudes are given in Table 4.

Table 4: Twist and wrench axes with corresponding unified compliance magnitudes of the cross pivot flexure mechanism

Corresp. axes	Unified compliance [\tilde{a}_{fi}]
\mathbf{w}_{f1}	$2.50 \cdot 10^{-07}$ m/N
\mathbf{w}_{f2}	$2.00 \cdot 10^{-08}$ m/N
\mathbf{w}_{f3}	$2.00 \cdot 10^{-08}$ m/N
$\mathbf{T}_{\gamma 1}$	$8.08 \cdot 10^{-07}$ m/N
$\mathbf{T}_{\gamma 2}$	$5.99 \cdot 10^{-08}$ m/N
$\mathbf{T}_{\gamma 3}$	<u>$3.38 \cdot 10^{-04}$ m/N</u>

As can be seen in Table 4, the multipliers are at least three orders smaller than the most underlined multiplier corresponding to the most dominant rotational degree of freedom. The cross flexure mechanism is thus dominantly rotational compliant which is consistent with the objective of the design. The total relative degree of freedom order based on the unified compliance multipliers following from the RasT approach is given as,

$$\mathbf{T}_{\gamma 3} \gg \mathbf{T}_{\gamma 1} > \mathbf{w}_{f1} > \mathbf{T}_{\gamma 2} > \mathbf{w}_{f3}/\mathbf{w}_{f2} \quad (38)$$

Double parallel flexure mechanism

The second mechanism is designed to be predominately translationally compliant, a double parallel flexure mechanism with an intermediate body. Figure 7 shows the twist and wrench compliant axes of the mechanism.

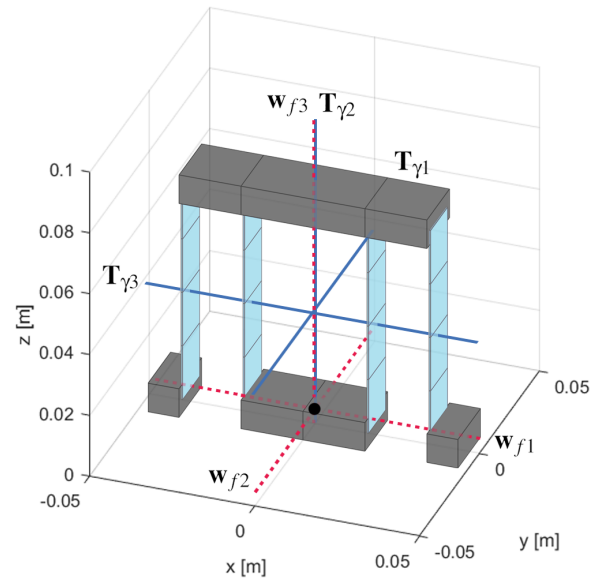


Fig. 7: Principal compliance directions of the double parallel flexure mechanism

The translational compliance multipliers corresponding to the wrench axes are given in Table 5 and the rotational compliance multipliers and the pitches corresponding to the twist axes are given in Table 6.

Table 5: Compliance magnitudes and corresponding wrench axes of the double parallel flexure mechanism

Corresp. wrench	Translational Compliance [a_{fi}]
\mathbf{w}_{f1}	<u>$4.50 \cdot 10^{-04}$ m/N</u>
\mathbf{w}_{f2}	$5.00 \cdot 10^{-07}$ m/N
\mathbf{w}_{f3}	$2.00 \cdot 10^{-08}$ m/N

Table 6: Compliance magnitudes and corresponding twist axes of the double parallel flexure mechanism

Corresp. twist	Rotational Compliance [a_{γ_i}]	Pitch [h_i]
$\mathbf{T}_{\gamma1}$	$3.12 \cdot 10^{-05}$ rad/Nm	0.00 m
$\mathbf{T}_{\gamma2}$	$7.80 \cdot 10^{-04}$ rad/Nm	0.00 m
$\mathbf{T}_{\gamma3}$	<u>$1.07 \cdot 10^{-03}$ rad/Nm</u>	0.00 m

The largest translational and rotational compliance multipliers are underlined and correspond to wrench \mathbf{w}_{f1} and twist $\mathbf{T}_{\gamma3}$. The compliance multipliers in Tables 5 and 6 can only be compared directly using the unified compliances \tilde{a}_γ and \tilde{a}_f . Figure 8 shows the unified compliance vectors along the twist and wrench axes with the corresponding unified compliances as magnitudes.

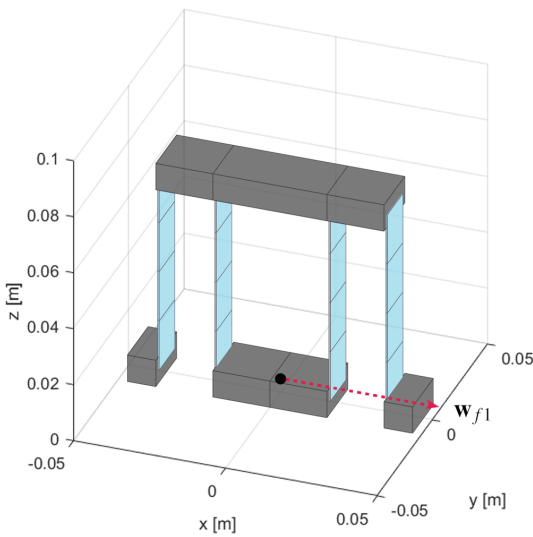


Fig. 8: Unified compliance vectors of the double parallel flexure mechanism

As can be seen in Figure 8, the largest compliance vector is in the direction of wrench axis \mathbf{w}_{f1} as is expected. It originates from the point of interest in the x-direction perpendicular to the face of the flexures. The other compliance vectors are too small to visualise using linear magnitude representation. The corresponding unified compliance magnitudes resulting from both approaches are given in Table 7.

Table 7: Twist and wrench axes with corresponding unified compliances of the double parallel flexure mechanism

Corresp. axis	Unified compl. [\tilde{a}_{fi}]	Unified compl. [\tilde{a}_{γ_i}]
\mathbf{w}_{f1}	<u>$4.50 \cdot 10^{-4}$ m/N</u>	<u>3.20×10^1 rad/Nm</u>
\mathbf{w}_{f2}	$5.00 \cdot 10^{-7}$ m/N	$3.56 \cdot 10^{-4}$ rad/Nm
\mathbf{w}_{f3}	$2.00 \cdot 10^{-8}$ m/N	-
$\mathbf{T}_{\gamma1}$	$4.40 \cdot 10^{-8}$ m/N	$3.12 \cdot 10^{-5}$ rad/Nm
$\mathbf{T}_{\gamma2}$	-	$7.80 \cdot 10^{-4}$ rad/Nm
$\mathbf{T}_{\gamma3}$	<u>$1.50 \cdot 10^{-6}$ m/N</u>	<u>$1.07 \cdot 10^{-3}$ rad/Nm</u>

As can be seen in Table 4, resulting from both approaches, the largest unified compliance magnitude, corresponding to the most dominant degree of freedom, is at least two orders larger than the other magnitudes. The double flexure mechanism is thus dominantly translational compliant consistent with the objective of the design. The total degree of freedom order based on the unified compliance multipliers \tilde{a}_{fi} following from the RasT approach is,

$$\mathbf{w}_{f1} \gg \mathbf{T}_{\gamma3} > \mathbf{w}_{f2} > \mathbf{T}_{\gamma1} > \mathbf{w}_{f3} \quad (39)$$

As discussed in Section 4.3, the fully decoupled rotational degree of freedom $\mathbf{T}_{\gamma2}$ is a non-evaluable value using the RasT approach. More insight is accumulated using the TasR approach. The total degree of freedom order based on the unified compliance multipliers \tilde{a}_{γ_i} following from the TasR approach is,

$$\mathbf{w}_{f1} \gg \mathbf{T}_{\gamma3} > \mathbf{T}_{\gamma2} > \mathbf{w}_{f2} > \mathbf{T}_{\gamma1} \quad (40)$$

where the multiplier corresponding to wrench \mathbf{w}_{f3} cannot be evaluated. Apart from the unevaluated degrees of freedom both approaches show the same order of compliance. The order based on both the RasT and the TasR approach can be interpreted as,

$$\mathbf{w}_{f1} \gg \mathbf{T}_{\gamma3} > \mathbf{T}_{\gamma2} > \mathbf{w}_{f2} > \mathbf{T}_{\gamma1} > \mathbf{w}_{f3} \quad (41)$$

6 Non-linear characterization

The visualisation using the unified compliance matrices \tilde{a}_f and \tilde{a}_γ , introduced in Section 5.1.1, can be used to characterize the non-linear behaviour of compliant mechanisms.

A displacement of the point of interest can be analysed incrementally. For each quasi-static-equilibrium the wrench and twist axes with the corresponding unified compliance multiplier matrices can be determined. This section shows the non-linear analysis of the introduced cross pivot flexure mechanism and two shell mechanisms using the unified compliances \bar{a}_f following from the RasT approach.

Cross pivot flexure mechanism non-linear

The point of interest of the cross pivot flexure mechanism introduced in Section 5.1.1 is subjected to a counter-clockwise $\pi/3$ radian rotation around the y -direction. Figure 9 shows the unified stiffness visualisation applied to the cross pivot flexure mechanism. The initial mechanism and compliance vectors are more transparent.

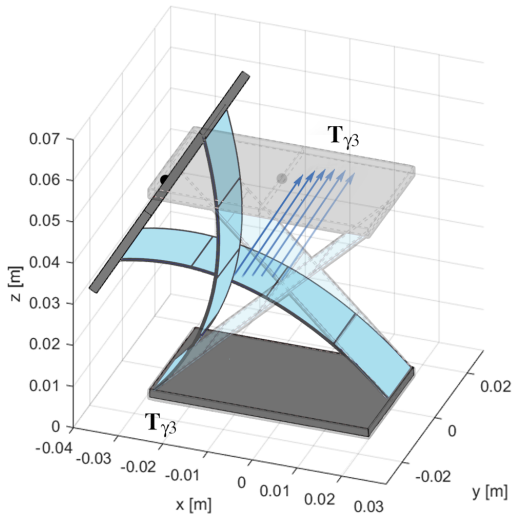


Fig. 9: Unified compliance vectors along a rotation of the point of interest around the y -axis range of motion

Only the unified compliance vector corresponding to twist \mathbf{T}_{γ_3} appears in Figure 9, since the other compliance magnitudes corresponding to the degrees of freedom are too small to visualise using linear magnitude representation. The vector magnitude corresponding to twist \mathbf{T}_{γ_3} is constant at $3.38 \cdot 10^4$ m/N during the rotation, but shows axis drift. The power of the characterization becomes more apparent in compliant shell mechanisms, as they have even less predictable and distinguishable degrees of freedom.

Single corrugated compliant shell

The first shell mechanism was introduced in Section 3, a moderately single corrugated shell mechanism. The mechanism is fully constrained at the bottom and the point of interest is in the centre of the opposing side, indicated by a black dot. Figure 10 shows the unified compliance visualisation applied to the single corrugated compliant shell mechanism. It shows the largest compliance vector corresponding

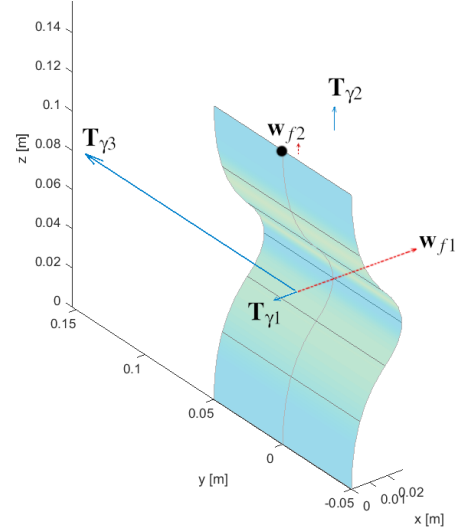


Fig. 10: Unified compliance vectors cross pivot

to twist \mathbf{T}_{γ_3} , which means that the largest compliance direction is a screw around the direction of twist \mathbf{T}_{γ_3} . The second largest compliance vector corresponds to wrench \mathbf{w}_{f1} which is a pure translation parallel to the direction of wrench \mathbf{w}_{f1} . The other unified compliance magnitudes are relatively small, intuitively explainable by the larger moment of inertia of the corresponding cross section. The total initial relative degree order based on the unified compliance multipliers \bar{a}_f following from the RasT approach is given as,

$$\mathbf{T}_{\gamma_3} > \mathbf{w}_{f1} > \mathbf{T}_{\gamma_2} > \mathbf{T}_{\gamma_1} > \mathbf{w}_{f2} > \mathbf{w}_{f3} \quad (42)$$

What is of specific interest is how these unified compliance vectors change over a large range of motion. Figure 11 shows the initial mechanism configuration from Figure 10 being deformed. The point of interest is subjected to a displacement along the positive x -axis direction. All other degrees of freedom are unconstrained. The compliance vectors are shown per quasi-static-equilibrium state during the displacement of the point of interest, as shown in Figure 11. The path of the point of interest is indicated with a black line. The initial configuration and compliance vectors are represented more transparently. Additionally, for visibility, only the four largest vectors are shown. Excluding the directional information of the vectors the magnitudes can be represented in a two-dimensional plot. The unified compliances \bar{a}_f against the absolute displacement of the point of interest are shown in Figure 12.

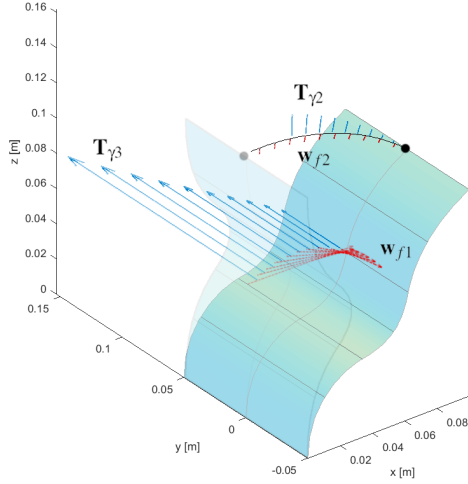


Fig. 11: Unified compliance vectors during displacement

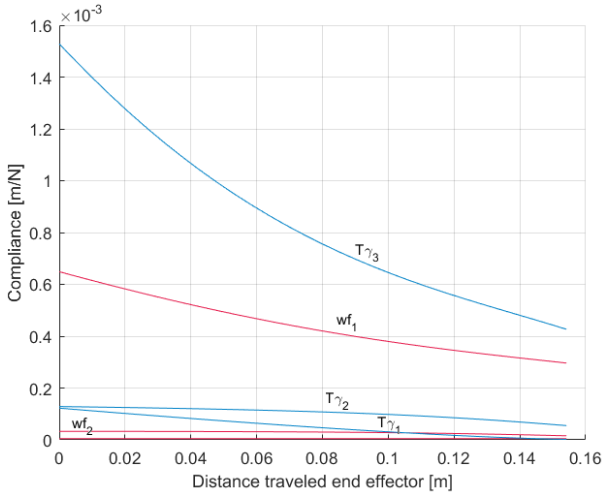


Fig. 12: Magnitude plot unified compliance over range of motion of the single corrugated shell

The initial values on the left of the graph represent the initial compliances shown in Figure 10. As shown, the mechanism is predominantly rotational compliant. Figure 12 shows that these statements remain valid along the displacement of the point of interest. As discussed in Section 2, the unified compliances are derived from the tangent stiffness matrix. The tangent stiffness matrix is composed of a physical stiffness and a geometrical stiffness matrix.

The change of vector directions and magnitude ratios are relatively constant. The directions of both wrench w_{f1} and twist $T_{\gamma 3}$ relative to the point of interest remain similar along the deformation. w_{f1} stays perpendicular to the flexure mechanism and $T_{\gamma 3}$ stays parallel to the face of the shell. The compliance magnitudes related to the twist and wrench axes in the direction of displacement are decreasing along the motion, which is explained by, build up, internal stress. Despite the assumed linear material behaviour, described by Hookes Law in the the physical stiffness

matrix, the mechanism exhibits non-linear behaviour. This behaviour is induced by the non-linear geometry stiffness matrix. However, the physical stiffness matrix is dominant since the overall shape of the mechanism does not undergo significant changes. The behaviour of the mechanism described in Figure 12 is relatively linear compared to the following extruded spiral shell mechanisms, where the unified compliance magnitude order switches during a translation along the x-axis.

Extruded spiral compliant shell

The second mechanism is an extruded spiral compliant shell mechanism. The material properties are identical to the single corrugated shell mechanism. The 2mm thick geometry is defined by NURBS [12], a third polynomial follows a 3×5 grid. Five coordinates are placed on three planes in $y = -0.05$, $y = 0$ and $y = 0.05$. The x and z coordinates are defined in Table 8.

Table 8: NURB coordinates extruded spiral shell

Point	1	2	3	4	5
x	0.00	-0.03	0.00	0.03	0.00
z	0.00	0.04	0.08	0.06	0.04

The mechanism is fully constrained at the bottom and the point of interest is in the centre of the opposing side, indicated by a black dot. The initial configuration is shown in Figure 13.

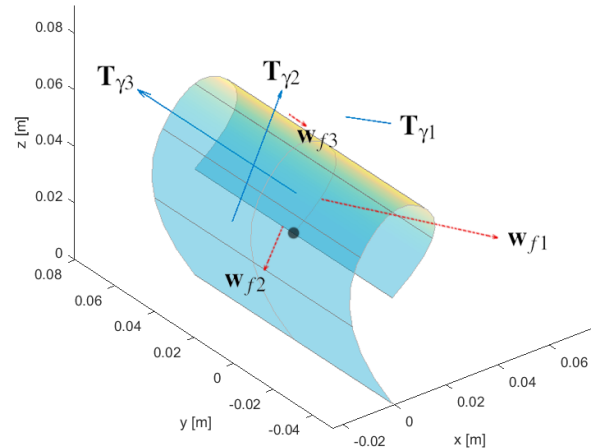


Fig. 13: Unified compliance vectors of the spiral shell mechanism

The total initial degree of freedom order based on the unified compliance multipliers \tilde{a}_f following from the RasT

approach is,

$$\mathbf{T}_{\gamma_3} > \mathbf{w}_{f1} > \mathbf{T}_{\gamma_2} > \mathbf{T}_{\gamma_1} > \mathbf{w}_{f2} > \mathbf{w}_{f3} \quad (43)$$

Although the mechanism is still a developable surface, predicting the locations and magnitudes of the compliance vectors is already more challenging compared to the previous shell mechanism. The two largest vectors are twist \mathbf{T}_{γ_3} and wrench \mathbf{w}_{f1} . As in the previous example these vectors are visualised during a displacement of the point of interest. The initial configuration of the mechanism is depicted in Figure 13. The point of interest is translated along the x-axis, while motion in the other directions is unconstrained, as can be seen in Figure 14.

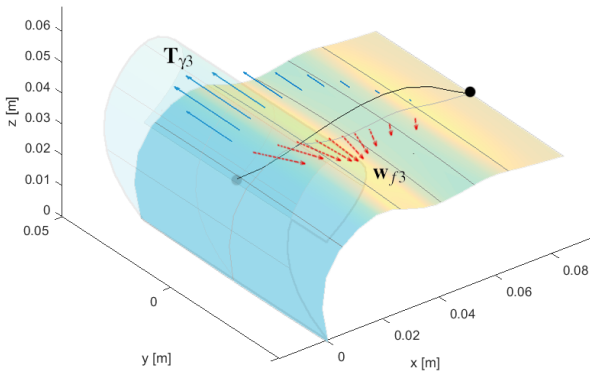


Fig. 14: Unified compliance vectors of the spiral shell mechanism during motion

The most significant difference with the previous shell mechanism is the non-linear behaviour of the compliance magnitudes, which results in a changing compliance magnitude order during the displacement. This behaviour is represented in Figure 15 which shows the unified compliance against absolute displacement of the point of interest.

The magnitude of the compliance directions behaves highly non-linear along the translational trajectory of the point of interest. The direction of twist \mathbf{T}_{γ_3} stays the same along the deformation, while the direction of wrench \mathbf{w}_{f1} changes substantially relative to the face of the mechanism. As discussed in the previous shell example, the non-linearity cannot be due to the stress building up, since this is defined by Hookes linear law. The non-linearity is due to the geometric stiffness matrix. The change in magnitudes is significant, resulting in a changing order of the unified compliances along the motion. In this example half of the compliance magnitudes increase initially, as the mechanism unfolds and undergoes significant geometrical changes. The decreasing geometry stiffness matrix change is more significant than the linearly increasing physical stiffness matrix halfway trough the motion, when the mechanism is unfolded. From then on the geometry stays relatively similar, thus less non-linearity is in-

duced by the geometry change. The increased physical stiffness becomes the most predominant factor and the unified compliance start to decrease at the end of the motion.

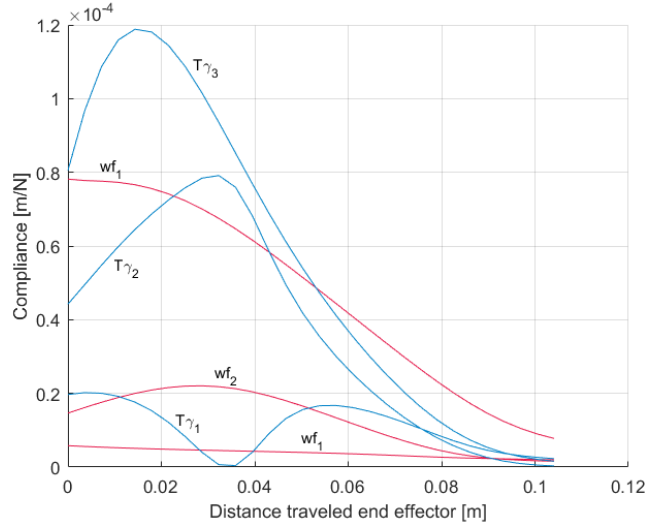


Fig. 15: Magnitude graph unified compliance over range of motion of the spiral shell mechanism

7 Discussion

The characterization presented in this paper has benefits compared to existing methods. Most characterizations do not address the coupling between rotations and translations [4] and are only able to separately compare rotational degrees of freedom and translational degrees of freedom, within one mechanism [6]. To compare rotational and translational compliances with each other it is necessary to introduce a unification variable. Where existing methods introduce arbitrarily chosen unification variables [9], this paper introduces two consistently derived physically meaningful unification lengths which include coupling, thus allowing the fair comparison of rotational and translational compliances within and between mechanisms.

We derived two unification lengths based on two approaches. The unification length resulting from the RasT approach, based on Plücker coordinates, is derived independently and yielded similar results as Lin's [8] research, based on hybrid coordinates, used to optimize graspers. Lin does not recognize the limitations of the results that became apparent when used to characterize the behaviour of non-linear compliant shell elements. We eliminate these limitations by introducing both the RasT and the TasR approach. Both Lin's derivation and the introduced potential energy method are more straightforward than the introduced virtual load method, however they give less insight into the actual kinematics. The virtual load method includes sub-steps with physical relevance, these sub-steps themselves can form the basis for designs. Thorough knowledge of the composition of these sub-steps provides the opportunity to vary parameters in an intelligent manner to reach specific objectives.

Additionally, energy, in any form, is a scalar quantity. By introducing the principle of potential energy all valuable directional information is lost.

8 Conclusion

This paper introduces a method for the characterization of non-linear behaviour for large deflections in complex compliant mechanisms that considers coupling and allows the comparison of stiffness between all six degrees of freedom. The characterization is based on consistently derived non-arbitrary unification variables based on equivalent compliance by virtual load and potential energy, therefore allows the comparison of compliance between degrees of freedom of different mechanisms. With this introduced comprehensive comparison the opportunity rises to order all degrees of freedom, within and between mechanisms in terms of compliance. The most predominant degrees of freedom can now be identified along the trajectory of large deflections of compliant mechanisms. The characterization, presented in this paper, can be done for any mechanism which has a symmetric positive definite non-singular compliance matrix. This includes both compliant flexure and shell mechanisms.

Acknowledgements

The writers would like to acknowledge NSF No. IIS - 1527133 as well as STW (HTSM-2012 12814: ShellMech) for the financial support of this project.

References

- [1] Seffen, K. A., 2012. "Compliant shell mechanisms". *Phil. Trans. R. Soc. A*, **370**(1965), pp. 2010–2026.
- [2] Pellegrino, S., 2005. "Bistable shell structures". In Proc. 46th AIAA/ASME/ASCE/AHS/ASC Structures, Structural Dynamics and Materials Conf., Austin, TX, 18–21 April 2005.
- [3] Radaelli, G., and Herder, J. L., 2014. "Isogeometric shape optimization for compliant mechanisms with prescribed load paths". *Proceedings ASME IDETC/CIE*.
- [4] Kim, C. J., 2005. "A conceptual approach to the computational synthesis of compliant mechanisms". PhD thesis.
- [5] J.P.A. Nijssen, G. Radaelli, C. K., and Herder, J., 2016. "Design and analysis of a shell mechanism based two-fold force controlled scoliosis brace".
- [6] J.P.A. Nijssen, G. Radaelli, C. K., and Herder, J., 2016. "Overview and kinematic characterization of compliant shell mechanism building blocks".
- [7] Lipkin, H., and Patterson, T., 1992. "Geometric properties of modelled robot elasticity: Part idecomposition". In Proceedings of ASME Design Technical Conferences, pp. 187–193.
- [8] Lin, Q., Burdick, J. W., and Rimon, E., 2000. "A stiffness-based quality measure for compliant grasps and fixtures". *IEEE Transactions on Robotics and Automation*, **16**(6), pp. 675–688.
- [9] Teichmann, M., 1996. "A grasp metric invariant under rigid motions". In Robotics and Automation, 1996. Proceedings., 1996 IEEE International Conference on, Vol. 3, IEEE, pp. 2143–2148.
- [10] Chasles, M., 1830. "Note sur les propriétés générales du système de deux corps semblables entr'eux et placés d'une manière quelconque dans l'espace; et sur le déplacement fini ou infiniment petit d'un corps solide libre". *Bulletin des Sciences Mathématiques, Férussac*, **14**, pp. 321–26.
- [11] Murray, R. M., Li, Z., and Sastry, S. S., 1994. *A mathematical introduction to robotic manipulation*. CRC press.
- [12] Piegl, L., and Tiller, W., 2012. *The NURBS book*. Springer Science & Business Media.
- [13] Jonker, J., and Meijaard, J., 1990. "Spacarc computer program for dynamic analysis of flexible spatial mechanisms and manipulators". *Multibody systems handbook*, **8**, pp. 123–143.

4

Characterization Experiment

Experimental Determination and Validation of Critical Components of the Unified Stiffness

This chapter supports the theory presented in Chapter 3, therefore creating a stronger basis for the subsequent Chapter 5.

1 Introduction

The goal of the experiment, presented in this Chapter, is to physically demonstrate and validate critical components of the theory presented in Chapter 3. The experiment validates relevant components of Lipkin's eigen-decomposition [1], with the objective to experimentally determine the unified stiffness of one eigen-wrench w_{fi} and one eigen-twist T_{γ_i} based on the TasR approach.

2 Experimental Design

The experiment was conducted on a physical compliant shell mechanism and was compared with a computational model based on an isogeometric analysis framework [2]. The eigen-twist and eigen-wrench of the physical model were analysed in a universal tester with two separate experiments. Both the eigen-twist and eigen-wrench were identified by applying various twists on the top edge of the clamped-free physical model.

To determine both the RasT and TasR unified stiffness the components of one eigen-twist and eigen-wrench of Lipkin's eigen-decomposition were determined both computationally and experimentally. The eigen-twist components to be determined were:

- Direction vector $[\gamma_i/|\gamma_i|]$
- Location vector $[r_i]$
- Pitch $[h_i]$
- Rotational stiffness $[k_{\gamma_i}]$

The eigen-wrench components to be determined were:

- Direction vector $[\tau_i/|\tau_i|]$
- Location vector $[b_i]$
- Pitch equivalent $[d_i]$
- Translational stiffness $[k_{f_i}]$

2.1 Experiment I: Eigen-twist analysis

To find the eigen-twist we varied the location vector magnitude variable of a gradually applied twist, while keeping the angular displacement γ and pitch h constant. For each applied twist we measured the loads in all 6 directions and determined:

- α The angle between the induced moment τ_i and the applied rotation γ_i
- k_{rot} The rotational stiffness in the direction of the applied rotation γ_i .

When the conditions $\alpha = 0$ and $k_{rot} = k_{\gamma_i}$ are met this indicate:

- The applied twist direction vector $\gamma_i/|\gamma_i|$, location vector r_i and pitch h_i correspond to an eigen-twist, since the induced wrench contains a moment τ_i parallel to the applied rotation γ_i .
- The calculated stiffness k_{rot} in the direction of the applied rotation γ_i equals the stationary rotational stiffness multiplier k_{γ_i} corresponding to an the eigen-twist.

2.2 Experiment II: Eigen-wrench analysis

To find the eigen-wrench we applied a pure translational twist. We measured the loads in all 6 directions and determined:

- β The angle between the induced force f_i and the applied translation δ_i
- k_{tran} The translational stiffness in the direction of the applied translation δ_i .

When the conditions $\beta = 0$ and $k_{tran} = k_{f_i}$ are met these results indicate:

- The induced wrench direction vector $\gamma_i/|\gamma_i|$, location vector b_i and equivalent pitch d_i correspond to an eigen-wrench, since the wrench contains a force τ_i parallel to the applied translation δ_i .
- The calculated stiffness in the direction of the applied translation δ_i equals the stationary rotational stiffness multiplier k_{f_i} corresponding to an the eigen-wrench.

3 Methods and Materials

This section presents the physical and computational model, the introduced variables and the measurement set-up.

3.1 Physical model

A shell mechanism was fabricated from a Polyethylene terephthalate glycol-modified (PETG) 3mm thick sheet using vacuum thermoforming. PETG is a clear amorphous thermoplastic, with a Young Modulus of 2.1 GPa and a Poisson ratio is 0.4. The mold for vacuum forming was 3D printed from ABS. The sheet was trimmed manually after vacuum thermoforming. The designed compliant shell mechanism was extended 20mm at the top and bottom edge to provide a surface to clamp the model to the ground and universal tester. The model is clamped with 3mm thick metal plates which are fastened using two M3 bolts. The metal plates also ensure the same boundary conditions along the edges. The Youngs Modulus of Steel is 200GPa, this ensured that the clamps stiffness is much greater than the shell mechanism. The thickness of the physical model turned out lower than the original sheet, due to stretching during vacuum thermoforming. The resulting average thickness of multiple sampling points was 2.6mm. The physical model and extensions are shown in Figure 1.

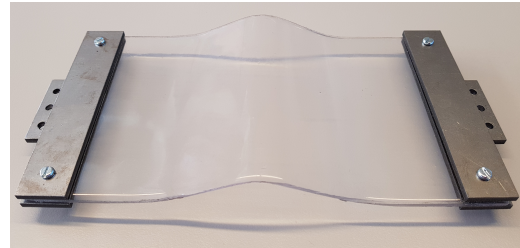


Fig. 1: Fabricated shell

3.2 Pre-Analysis Computational Model

The fabricated shell was computationally modelled based on an isogeometric analysis framework [2], with an assumed uniform thickness. The computational model is fully constrained along the bottom edge. The point of interest is located on the stiff modelled top edge at which C_t is determined is indicated by a black dot, as can be seen in Figure 2. Figure 2 includes one eigen-wrench w_{f3} and one eigen-twist $T_{\gamma3}$ plotted with their corresponding RasT unified stiffness magnitude based on Chapter 3. Due to the symmetry of the model in the $y=0$ and $z = 0.75$ surfaces, both the eigen-wrench and the eigen-twist are parallel to the z -axis and located along $y=0$.

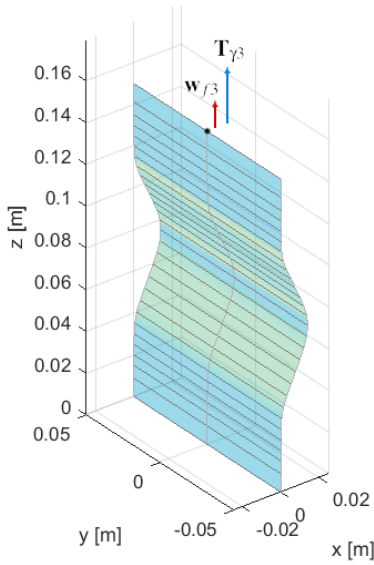


Fig. 2: Modelled eigen-wrench and eigen-twist axes with unified stiffness magnitude

The components of the modelled eigen-twist are given in Table 2.

Table 1: Eigen-twist $T_{\gamma3}$ components

Direction	$[0,0,1]$
Location vector	$[1.05 \cdot 10^{-2}, 0, 0]$ m
Pitch	$2.53 \cdot 10^{-12} \approx 0$
Rotational stiffness	4.32 Nm/rad
RasT Unified stiffness	$3.91 \cdot 10^4$ N/m
TasR Unified stiffness	4.33 Nm/rad

The components of the modelled eigen-wrench are given in Table 2.

Table 2: Eigen-wrench w_{f3} components

Direction	$[0,0,1]$
Location vector	$[4.20 \cdot 10^{-3}, 0, 0]$ m
Equivalent pitch	0
Translational stiffness	$8.26 \cdot 10^4$ N/m
RasT Unified stiffness	$8.26 \cdot 10^4$ N/m
TasR Unified stiffness	1.47 Nm/rad

3.3 Variables

The applied twists are varied based on the pre-analysis, with the objective to meet the conditions defined in section 2.1. The applied twist are varied by varying the location vector for different trails, while keeping the rotational direction and pitch constant. The pre-analysis indicated that the eigen-twist is parallel to the z -axis and the location vector is parallel to the x -axis, due to symmetry in the x - and y -direction. The pre-analysis also indicated an eigen-twist pitch of zero. We assumed that the vacuum thermoforming process did not introduce asymmetry and that therefore these indications remain valid in the physical model. To find the location vector corresponding to the eigen-twist only the location vector magnitude $|r_i|$ was varied while keeping the vector direction parallel to the x -axis. Figure 3 shows the influence of two different location vector magnitudes on the point of interest's arc-trajectory. The assumptions made in this section are validated as incorrect assumptions will not lead to the localisation of the eigen-twist.

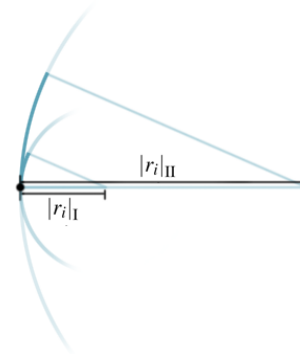


Fig. 3: Top view arc-trajectory point of interest, based on different twist location vector magnitudes

For each twist with different location vector magnitude, three trails were executed with an increasing small angular displacement up to 0.053 rad and zero pitch. To locate the eigen-wrench, based on the pre-analysis, the location independent pure translation along the z -axis was applied. Three trials were executed with an increasing small translation up to 1.1 mm. The deformations were small and gradually ap-

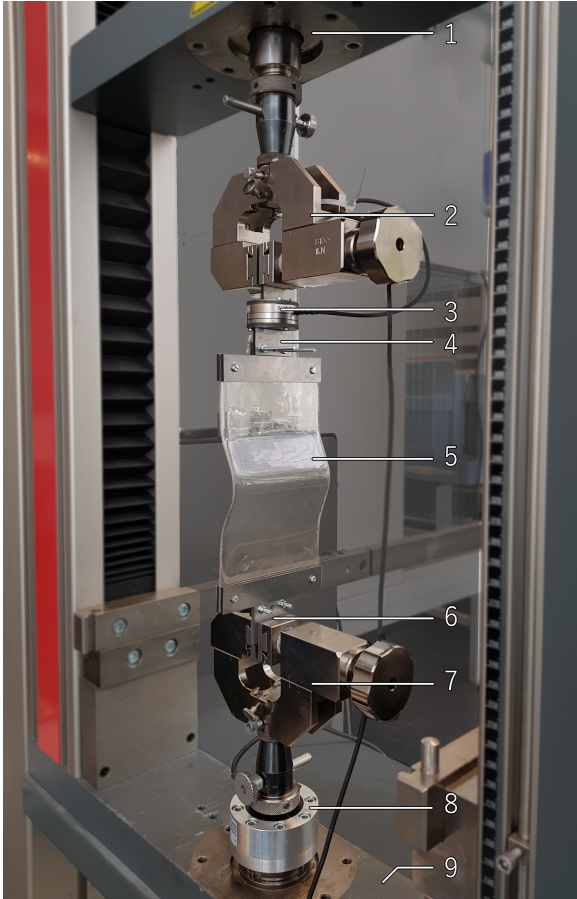


Fig. 4: Measurement setup

plied over the course of 60 seconds, since we were researching instantaneous properties of the undeformed shell mechanism.

3.4 Measurement Set-up

The universal tester Zwick Z005 forms the basis for the measurement set-up, which can be seen in Figure 4. From top to bottom the set-up consists of:

1. Zwick Z005 Universal tester displacement inducer
2. Top Bench vice
3. ATI Mini40-2 6-DoF load cell
4. Top offset bracket
5. Physical model
6. Bottom offset bracket
7. Bottom Bench vice
8. Zwick HBM-T20WM/KAF-TC 1-DoF load cell
9. Zwick Z005 Universal tester ground

The Zwick Z005 Universal tester is able to apply a displacement or a rotation (1) on the top bench vice (2). The top bench vice is connected through the ATI Mini40-2 6-DoF load cell (3) to the top bracket (4). The clamped extensions of the physical model (5) are connected to the 3mm thick steel brackets (4,6). The bottom bracket (6) is connected to the bottom bench vice (7). The bottom bench vice is con-

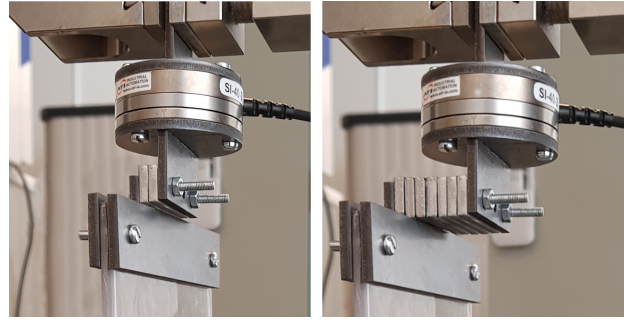


Fig. 5: Top bracket with offset spacers for eigen-twist analysis

nected through a 1-DoF load cell (8) to the ground (9). For the eigen-twist analysis, the 1-DoF load cell is the Zwick HBM-T20WM. For the eigen-wrench analysis, the 1-DoF load cell is the Zwick KAF-TC. The z-axes of all load cells are in line with the rotational axis of the universal tester displacement inducer. The ATI40 load cell is connected to a LabVIEW[®] program. The Zwick load cells are connected to testXpert[®].

The brackets have a variable offset for the eigen-twist analysis, which can be seen with different offsets in Figure 5. The offsets vary the location vector magnitude $|r_i|$ of the applied twists. The offset in the brackets is varied by varying the amount and thickness of the used steel plates. During the trials, there was no difference in offset between the top and bottom bracket.

3.5 Resolution and Calibration

The ATI Mini40-2 has the lowest resolution of the used load cells, given in Table 3.

Table 3: Resolution ATI Mini40

Axis	Resolution
Fx,Fy	$1.00 \cdot 10^{-2}$ N
Fz	$2.00 \cdot 10^{-2}$ N
Tx,Ty,Tz	$2.50 \cdot 10^{-4}$ Nm

The ATI Mini 40 load cell was calibrated in the universal tester using the redundant measurement direction of the Zwick load cells. Both 1-DoF Zwick load cells measured values are within the permissible tolerances according to DIN EN ISO 7500-1. The redundant measurement directions were also used to synchronise the measured Zwick data and ATI load cell data during the trials.

4 Results and Discussion

This section provides the results of the experiment trails. The results are compared to the original model, as can be

seen in Tables 4 and 5. The results are listed below and will be discussed in the subsequent sections.

Table 4: Eigen-twist T_{f3} components

	Model	Experiment
Location vec. length	$1.05 \cdot 10^{-2}$ m	$1.0 \cdot 10^{-2}$ m
Pitch	≈ 0 m	0 m
Rotational stiffness	4.33 Nm/rad	4.29 Nm/rad
RasT Unif. stiffness	$3.91 \cdot 10^4$ N/m	$4.3 \cdot 10^4$ N/m
TasR Unif. stiffness	4.33 Nm/rad	4.3 Nm/rad

The RasT and TasR unified stiffness of the corresponding eigen-twist respectively differ +9.21% and -0.93%.

Table 5: Eigen-wrench w_{f3} components

	Model	Experiment
Location vec. length	$4.20 \cdot 10^{-3}$ m	$3.90 \cdot 10^{-2}$ m
Equivalent Pitch	≈ 0 m	$5.00 \cdot 10^{-4}$ m
Translational stiffness	$8.26 \cdot 10^4$ N/m	$7.95 \cdot 10^4$ N/m
RasT Unif. stiffness	$8.26 \cdot 10^4$ N/m	$7.95 \cdot 10^4$ N/m
TasR Unif. stiffness	1.47 Nm/rad	1.23 Nm/rad

The RasT and TasR unified stiffness of the corresponding eigen-wrench respectively differ +3.90% and -13.90%.

4.1 Discrepancy factors

The potential factors influencing the discrepancy between the modelled and experimentally determined eigen-twist and eigen-wrench components are explained in the following sections and listed below.

- The production process: Uneven stretching during vacuum thermoforming introduces thickness variation and anisotropic material behaviour of the physical model. The option for a varying thickness and anisotropic material behaviour is not incorporated in the computational model.
- Unwanted introduced compliance and slack in the measurement set-up: The universal tester is mainly designed to test force and torque parallel to the z-axis. It is likely that the universal testers translational and rotational compliance is greater in the x- and y-direction compared to the z-direction. To illustrate the sensitivity of the strict constraints an adjusted model is introduced which allows small rotations < 0.01 rad in the x- and y-direction. The allowed small rotations are arbitrary

chosen, the adjusted model is therefore unreliable and not used to determine the quantitative data presented in Tables 4 and 5. The option to actually add compliance, friction or slack in the constraint directions is not incorporated in the computational model.

- Unaccounted pre-loading: Pre-bending and resulting pre-loading is known to increase compliance [3]. The measurement set-up potentially introduces pre-bending.
- Material behaviour: The Youngs modulus of the material used for the physical model is based on literature, while the actual material properties are potentially different. The Youngs modulus can be adjusted for in the computational model. However, because multiple potentially opposing effects are present, as described above, and the actual material behaviour is unknown adjusting for material properties does not give a more reliable model.

4.2 Eigentwist: Moment angle for various location vector magnitudes

The angle α between the induced moment and the applied rotation for varying location vector magnitudes is given in Figure 6. A zero α angle indicates a location vector magnitude corresponding to an eigentwist, since this indicates that the applied rotation is parallel to the induced moment. The angle α of the computational model is zero at a magnitude of 10.50mm, in accordance with Table 2. The angle α of the average measurement fit of the three trails is zero at a magnitude of 10mm. This shows that the computational and measured eigen-twist location vector magnitude differs 0.5mm. This discrepancy is potentially introduced by the production process, as a non-uniform thickness and anisotropic material behaviour influence the local compliance of the physical model. The measurement fit moment angles are smaller than the modelled moment angles, this is potentially explained by unwanted introduced compliance and slack in the measurement set-up. Greater introduced compliance and slack in the x- and y-direction compared to the z-direction will result in lower calculated moment angles α . The more accurate adjusted model that illustrates the sensitivity of the strictly modelled constraints supports this assumption. Furthermore unaccounted pre-loading potentially reduces the stiffness of the physical model.

4.3 Eigentwist: Rotational stiffness for various location vector magnitudes

The rotational stiffness in the direction of the applied rotation is determined by evaluating the slope of the induced parallel moment. The rotational stiffness for varying location vector magnitudes is given in Figure 7, which shows that the rotational stiffness K_{zz} of the model has a minimum at a magnitude of 10.5mm. The average measurement fit of the three trails shows that rotational stiffness K_{zz} of the measurements has a minimum at a magnitude of 10mm. The lowest rotational stiffness indicates the location vector magnitude corresponding to the eigen-twist. The location vector magnitudes are in accordance with the results of Figure 6 and Table 2.

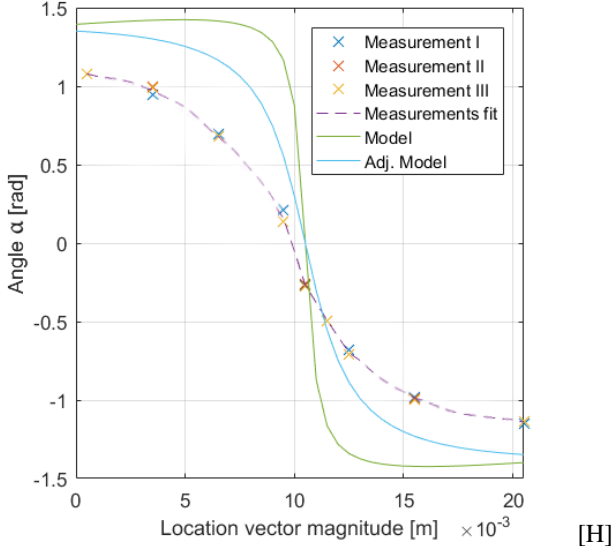


Fig. 6: Moment angle with varying x-axis offset

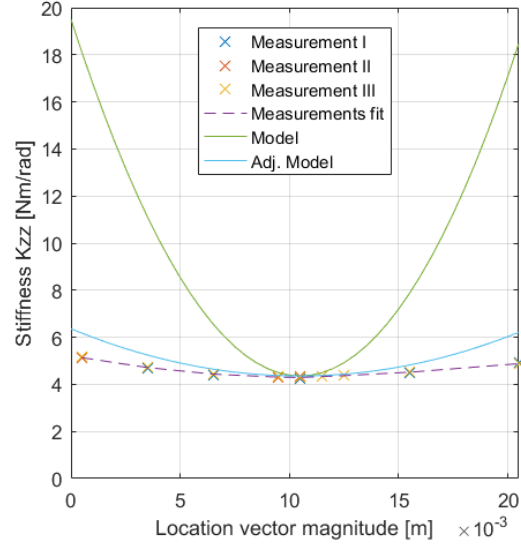


Fig. 7: Stiffness K_{zz} with varying x-axis offset

The computationally modelled and physical model stiffness curve diverge when deviating from the location vector magnitude corresponding to the eigen-twist. Similar to the observations in Figure 6, this could be explained by introduced compliance in the measurement set-up. Measurement deviating from the location vector magnitude rely more on the constraints in x- and y-direction of the measurement set-up, since introduced compliance and slack in the x- and y-direction would be most apparent for larger moments in their corresponding directions. This would also explain why the effect is the smallest at the location vector magnitude corresponding to the eigen-twist, as the induced moment is parallel to the z-axis for this magnitude. The more accurate adjusted model that illustrates the sensitivity of the strictly modelled constraints supports this assumption. The small rotational stiffness difference at the eigen-twist location vector magnitude could be explained by the constraints, production process or the assumed material properties. This material properties are not adjusted in the model, since multiple potentially opposing factors are present influencing the accuracy of the rotational stiffness.

Figures 6 and 7 both indicate independently that the eigen-twist location vector magnitude of the model is 10.5mm and the of the measurements is 10mm.

4.4 Eigentwist: Induced moments against angle of applied twist

The moments along the increasing rotation as a result of the, modelled and experimentally determined, eigen-twists can be seen in Figure 8. The measured data shown is the interpolated average data of the trails at the offsets 9.5mm and 10.5mm, since no measurement trails were executed at a 10mm offset. The angle between the measured induced moment and the z-axis is $0.034 \approx 0$ rad.

The initial slopes of the induced moments T_z deter-

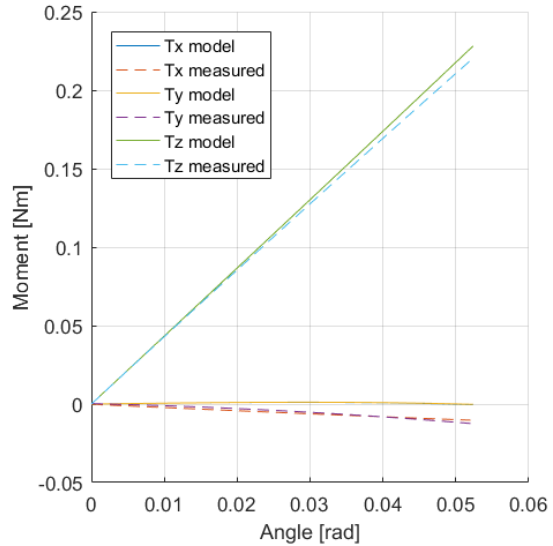


Fig. 8: Moments along angular deformation at 10 mm measurement and 10.5 mm model offset

mine the stiffnesses corresponding to the modelled and experimentally determined eigen-twists. The unified stiffness can be determined based on eigen-twist the location vector magnitude and the corresponding rotational stiffness. The measured and modelled rotational stiffness and unified stiffnesses are given in Table ???. The modelled and experimentally determined unified stiffnesses differ as a result of different location vector magnitudes and corresponding stiffnesses, which are, in their turn explained in the interpretations of Figures 6 and 7.

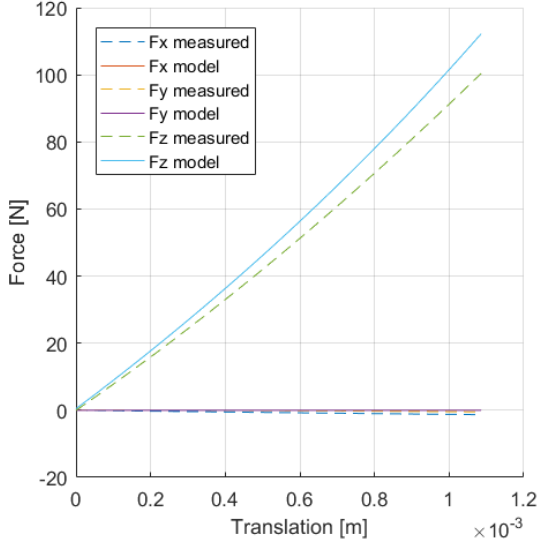


Fig. 9: Forces along the translational deformation

4.5 Eigenwrench: Induced load against translation

The forces along the translation as a result of the applied twist can be seen in Figure 9. The angle β between the induced force and the applied translation is $0.01 \approx 0$ rad. The initial slopes of the induced forces F_z determine the stiffnesses corresponding to the modelled and experimentally determined eigen-wrenches. The equivalent pitch and the location vector of the eigen-wrench can be determined from Figures 9 and 10. The location vector is defined by the ratio between T_y and F_z . The experimentally determined location vector $b_i = 3.9mm$. The ratio between T_x and F_z determines the equivalent pitch $d_i = 3.9mm$. The experimentally determined equivalent pitch $d_i = 0.5mm$. The angle $\beta \approx 0$ indicates that the induced wrench is an eigen-wrench. The stiffness resulting from the measurements is lower than the modelled stiffness, which could be explained by introduced compliance in the measurement set-up.

4.6 General

The experiment showed that the unified stiffness of an eigen-wrench and eigen-twist can be determined experimentally. However this is done by calculations based on measured twists and induced wrenches. To truly validate the theory presented in Chapter 3 an additional experiment is necessary. This additional experiment should measure the unified stiffnesses in a more direction manner, independent of Lipkin's eigen-decomposition. Subsequently the results of this additional experiment can be compared with the experiment presented in this Chapter. This comparison would be the final step in the validation of the unified stiffness.

The modelled and measured results differ, explained by introduced compliance, slack and pre-loading due to the measurement set-up. As well as thickness variation and anisotropic material behaviour of the physical model as a result of uneven stretching during vacuum thermoforming.

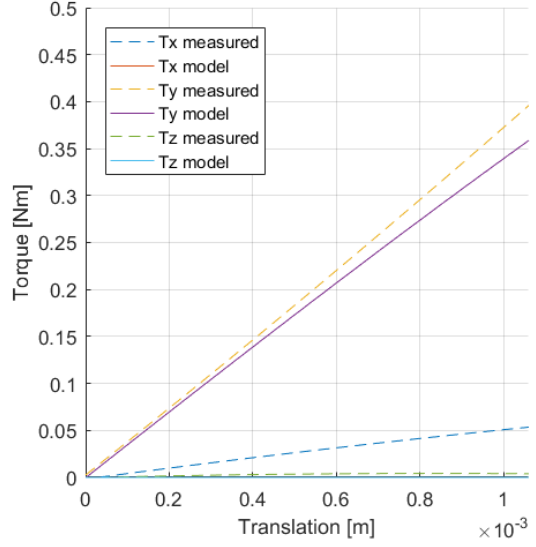


Fig. 10: Moments along the translational deformation

Both introduced compliance and slack in the measurement set-up and thickness variation and anisotropic material behaviour are not integrated into the computational model used. The arbitrary adjusted model illustrated the substantial sensitivity of the strict constraints. It is recommended to do a thorough sensitivity analysis on the presented phenomena influencing the discrepancy between the computationally and experimentally determined unified stiffnesses. It would also be recommended to validate the assumed material properties using a tensile test. It is also recommended to increase the quantitative reliability of the experiment by prioritizing the stiffness in the x and y rotational and translational direction of the measurement set-up.

The presented strategy to experimentally determine and validate all components of the unified stiffness can be used to construct one eigen-twist and one eigen-wrench. The experiment has the potential to fully determine Lipkin's eigen-decomposition. The complete eigen-decomposition can be used to construct the 6x6 tangent stiffness matrix of a spatial compliant mechanism. To determine all eigen-twists and eigen-wrenches the measurement set-up displacement inducer must be extended with four additional DoF's.

5 Conclusion

The experiment has shown that the unified stiffness, corresponding to an eigen-twist and eigen-wrench of a physical model can be determined experimentally within the same order of magnitude as the computational model. The measured qualitative behaviour of the physical model is similar to the computational model but the quantitative data indicates divergence at measurements deviating from the eigentwist location. However, the discrepancies between the measured and computationally modelled data are substantial. The discrepancies can be partially explained by the measurement set-up design and the production process of the physical

model.

References

- [1] Lipkin, H., and Patterson, T., 1992. “Geometric properties of modelled robot elasticity: Part idecomposition”. In Proceedings of ASME Design Technical Conferences, pp. 187–193.
- [2] Cottrell, J. A., Hughes, T. J., and Bazilevs, Y., 2009. *Isogeometric analysis: toward integration of CAD and FEA*. John Wiley & Sons.
- [3] Dunning, A., Tolou, N., Pluimers, P., Kluit, L., and Herder, J., 2012. “Bistable compliant mechanisms: Corrected finite element modeling for stiffness tuning and preloading incorporation”. *Journal of Mechanical Design*, **134**(8), p. 084502.

5

Characterization Library

Paper: Compliant Shell Building Block Characterization Library Utilizing Unified Stiffness

This paper is to be submitted to the ASME Journal of Mechanisms and Robotics (JMR) or the Elsevier Journal of Mechanism and Machine Theory (MMT).

Unified Non-Linear Characterization applied to Compliant Shell Mechanism Building Blocks

Joost R. Leemans¹, Charles J. Kim², Werner W.P.J. van de Sande¹ and Just L. Herder¹

¹ *Department of Precision and Microsystems Engineering, Delft University of Technology*

² *Department of Mechanical Engineering, Bucknell University*

Compliant shell mechanisms are valuable building blocks for spatial mechanisms design, due to their unique kinematics and geometry. To match building blocks and design specifications this paper introduces a library of promising building blocks which are characterized using a unified stiffness method and in this paper introduced definitions, which allows for a full compliance comparison between all translational and rotational kinematic degrees of freedom within and between building blocks, while accounting for coupling and geometric non-linear behaviour.

1 Introduction

Compliant shell mechanisms are spatially curved thin-walled structures used to transmit or transfer loads, motion or energy through elastic deformation [1]. The main benefits of compliant shell mechanisms, as stated by Howell [2] and Radaelli [3], are easy assembly, no wear, no backlash, low friction, easy assembly and no need for lubrication. Additional benefits are easy cleaning and possibly appealing aesthetics.

In related research shell elements are described and characterized both computationally as can be seen in work of Kim [4] and Radaelli & Herder [5] and analytically, as can be seen in the work of Seffen [6], Pellegrino [7]. Lipkin & Patterson [8] first introduced an eigen-decomposition to characterize principal kinematic rotational and translational degrees of freedom axes and corresponding stiffness while including coupling, utilizing Plücker coordinates [9]. Based on this eigen-decomposition, Leemans [10] introduced the unified stiffness characterization method.

Libraries of building blocks provide the opportunity to match building blocks with design specifications [11]. While libraries are presented in previous work [1], no library of building blocks is available that captures non-linear behaviour, coupling and unified stiffness. Such a library would be valuable since a thorough description of non-linear behaviour is necessary for designs subjected to large deformations. Furthermore, including the unified stiffness allows for a physically meaningful and consistent comparison between all degrees of freedom within and between mechanisms. The comparison provides the possibility to order all relative kinematic degrees of freedom of the building blocks in terms of compliance. With the introduction of a systematic degree of compliance order rises the opportunity

to consistently classify different types of degrees of freedom as either constraints or freedom directions.

In this paper, we introduce definitions utilizing the unified stiffness, on which a characterization framework is based. This characterization framework is applied on promising building blocks introduced by Nijssen [1].

The paper is organized as follows, section 2 contains background theory on the eigen-decompositions and the unified stiffness characterization. Section 3 introduces definitions, utilizing the unified stiffness. Section 4 presents the characterization framework and the characterized building blocks with interpretation and generalization. Section 5 discusses the contributions made by this paper. A brief summary is given and a general conclusion is drawn in Section 6.

2 Background

This section provides background information on eigen-decompositions and the unified stiffness characterization method as described in the work of Lipkin & Patterson [8] and Leemans [10].

2.1 Eigen-decomposition

Any symmetric positive definite non-singular tangent stiffness K_t and tangent compliance matrix C_t can be decomposed into an eigen-system as described by Lipkin & Patterson [8]. The eigen-decomposition describes three translational and three rotational principal axes, with corresponding stationary multiplier values of the translational and rotational stiffness. Lipkin's eigen-decomposition of the tangent stiffness matrix K_t is defined as,

$$K_t = [\hat{\mathbf{w}}_f \ \hat{\mathbf{w}}_\gamma] \begin{bmatrix} k_f & 0 \\ 0 & k_\gamma \end{bmatrix} \begin{bmatrix} \hat{\mathbf{w}}_f \\ \hat{\mathbf{w}}_\gamma \end{bmatrix} \quad (1)$$

and the resulting tangent compliance matrix eigen-decomposition is defined as,

$$C_t = [\hat{\mathbf{T}}_f \ \hat{\mathbf{T}}_\gamma] \begin{bmatrix} a_f & 0 \\ 0 & a_\gamma \end{bmatrix} \begin{bmatrix} \hat{\mathbf{T}}_f \\ \hat{\mathbf{T}}_\gamma \end{bmatrix} \quad (2)$$

where for $i = 1, 2, 3$ multipliers $k_{\gamma i} > 0$ and $a_{\gamma i} > 0$ are the angular stiffnesses and compliances in the directions of the

γ_i , multipliers $k_{f_i} > 0$ and $a_{f_i} > 0$ are the translational stiffnesses and compliances in the directions of the f_i . \mathbf{w}_f are the eigen-wrenches, these directions are also known as the wrench or principal translational kinematic degrees of freedom axes, defined as

$$\mathbf{w}_{f_i} = \begin{bmatrix} \vec{f}_i \\ \vec{c}_i \end{bmatrix}, \quad i = 1, 2, 3 \quad (3)$$

Applying an eigen-wrench \mathbf{w}_{f_i} leads to an induced twist \mathbf{T}_{f_i} a pure translational displacement parallel to the force direction \vec{f}_i . \mathbf{T}_γ are the eigen-twists, these directions are also known as the twist or principal rotational kinematic degrees of freedom axes, defined as

$$\mathbf{T}_{\gamma_i} = \begin{bmatrix} \vec{\delta}_i \\ \vec{\gamma}_i \end{bmatrix}, \quad i = 1, 2, 3 \quad (4)$$

Applying an eigen-twist \mathbf{T}_{γ_i} leads to an induced wrench \mathbf{w}_{γ_i} a pure moment parallel to the rotational direction $\vec{\gamma}_i$

2.2 Unified stiffness

Leemans [10] introduced a characterization based on unified stiffness which takes into account coupling and allows comparison of compliance between all six degrees of freedom of mechanisms. With this comprehensive comparison the opportunity rises to order all degrees of freedom, within and between mechanisms in terms of compliance.

The diagonal matrices of the decompositions in Equations 1 and 2 consist of the compliance and stiffness stationary multipliers corresponding to the eigen-wrench and eigen-twist axes. Considering the decomposition in Equation 2, the upper three stationary multipliers a_f are the translational compliances and the lower three stationary multipliers a_γ are the rotational compliances. To enable a meaningful comparison between rotational and translational stationary multipliers two approaches are introduced. The most intuitive and widely applicable is the RasT approach which expresses the rotational compliance as an equivalent translational compliance at the point of interest resulting in the RasT unification equation,

$$\tilde{a}_{f_i} = \chi_i^2 a_{\gamma_i} \quad (5)$$

where χ_i is the unification variable,

$$\chi_i = \sqrt{h_i^2 + |r_i|^2} \quad (6)$$

3 Quantification definitions

To quantify the relations of the degrees of freedom we introduce new definitions utilizing the unified stiffness.

With the availability of the comprehensive comparison between the degrees of freedom the opportunity rises to order all the compliances corresponding to these degrees of freedom. The degrees of compliance (DC) correspond to the de degrees of freedom of a mechanism in decreasing order given as,

$$DC_1 > DC_2 > DC_3 > DC_4 > DC_5 > DC_6. \quad (7)$$

In addition to the degree of compliance order we can compare the ordered degrees of compliance, by defining the degree of compliance ratio's. All compliances are normalized with respect to the primary compliance DC_1 of the mechanism. The degree of compliance ratio's η_{DC_i} are given as,

$$\eta_{DC_i} = \frac{DC_i}{DC_1} \quad i = 1, 2, \dots, 6 \quad (8)$$

To determine the amount of freedom and constraint directions of a mechanism in a consistent manner we introduce the degree of freedom threshold t . Which counts the amount of degrees of freedom of which the degree of compliance ratio is larger than a specified threshold. Based on the degree of freedom threshold t we introduce the number of threshold freedom directions FD_t defined as,

$$FD_t = COUNTIF(\eta_{DC_i} > \frac{1}{t}) \quad i = 1, 2, \dots, 6 \quad (9)$$

and the number of threshold constraint directions in 3-dimensional space \mathbb{R}^3 is defined as,

$$CD_t = 6 - FD_t \quad (10)$$

A threshold of $t = 10$ would find the amount of degrees of freedom whose corresponding unified compliances are larger than one-tenth of the primary compliance, thus the same order of magnitude. Defining the amount of threshold freedom and constraint directions is solely possible due to the unified stiffness characterization.

To compare the compliances of mechanisms in a group of building blocks we introduce the normalized primary compliance. Which is the primary compliance of a specified mechanism normalized with respect to the primary compliance of the most compliant building block in the, to be compared, building block group. The normalized primary degrees of compliance are given as,

$$|\eta_{DC_i}| = \frac{DC_1}{MAX(DC_1)} \quad (11)$$

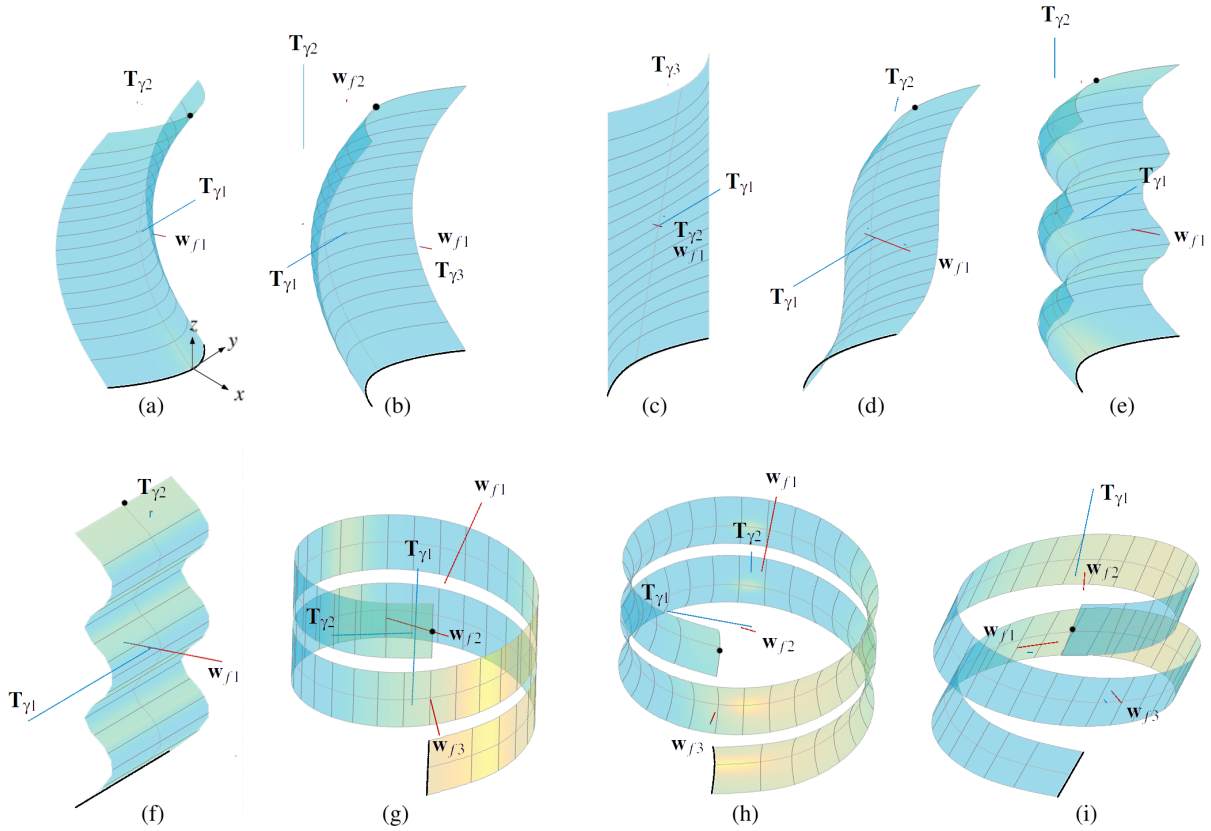


Fig. 1: Overview of the initial state unified compliances and directions

4 Characterization

This section introduces a characterization framework, based on the unified stiffness and the introduced quantification definitions. The characterization is applied to promising building blocks introduced by Nijssen [1]. The dimension of the building blocks are in the same order of magnitude as they fit in the same box. The physically feasible building blocks are illustrated in Figure 1. The surface equations and the affect of the corresponding parameters are described in Appendix 6. This section provides an interpretation and generalization of the characterization results.

4.1 Linear characterization

The shell mechanisms are evaluated using an isogeometric analysis, all with the same linear material properties; the Young Modulus is 2.9 GPa and the Poisson ratio is 0.38. The 2mm thick geometries are translated into NURBS [12]. All mechanisms are fully constraint along one edge, indicated in Figure 1 by black lines. The opposing edges are modelled infinite stiff along the edge and the point of interests connected to these edges are indicated with black dots. The tangent stiffness matrices are determined with respect to these points of interest.

Figure 1 shows all building blocks characterized using the RasT unified stiffness characterization. The direction of a blue unified compliance vector represents an eigen-twist direction. The direction of a red unified compliance vec-

tor represents an eigen-wrench direction. The magnitudes of the vectors represent the corresponding unified compliances. Larger compliance vectors represent greater compliance of the corresponding degrees of freedom.

Due to the different order of magnitudes of the unified compliances, the vector magnitudes are not represented on the same scale. To gain insight into the relation of the compliances between the building blocks we compare and order the primary compliances of all building blocks. By using, the in section 3 introduced, normalized primary compliances, as can be seen in Table 1. The normalized primary degrees of compliance ratios are ordered in increasing compliance order.

Table 1: Normalized primary compliances

B. block	$ \eta_{DC_1} $
A) Hyperbolic parabolic	$5.63 \cdot 10^{-03}$
B) Double parabolic	$6.02 \cdot 10^{-03}$
D) Shoe surface	$1.27 \cdot 10^{-02}$
C) Parabolic canoid	$1.36 \cdot 10^{-02}$
E) Double corrugated	$1.51 \cdot 10^{-02}$
F) Single corrugated	$7.00 \cdot 10^{-02}$
H) Sinusoidal helix	$2.65 \cdot 10^{-01}$
G) Helix	$3.99 \cdot 10^{-01}$
I) Evolvent helicoid	1.00

Large differences in primary compliance are observed. Although mechanism A to F and G to I are of similar size it shows that the primary compliance differs at least one order of magnitude. Explained by the larger arc-length of the helix based mechanisms, defined by the shortest distance from the point of interest to the base, through the surface.

Table 2 shows the compliance type order per building block and the in section 3 introduced amount threshold freedom directions FD_t with $t = 10$ in the undeformed configuration.

Where Table 1 provides the comparison between building blocks, Table 2 provides the comparison of degrees of freedom within the building blocks. All building blocks except for the Sinusoidal Helix have an eigentwist direction as primary compliance. All building blocks except for the Parabolic Canoid have more than one FD_{10} .

4.2 Non-linear characterization

In this section we describe the non-linear behaviour of the shell building blocks in terms of the unified stiffness and the introduced definitions. The building blocks are actuated under influence of wrenches that initially result in the displacement in the direction of the initial three primary compliance axes, while being held fixed along a boundary. The three primary actuations are referred to as *Act. w_{DC_1}* , *Act. w_{DC_2}* and *Act. w_{DC_3}* .

The results of all building blocks, introduced in section 4, are captured graphically in an library shown Appendix B of which one is presented in Figure 2 and discussed in detail. The behaviour of all building blocks is described by discussing unique behaviour. The three actuations are listed, followed by a colon and a short description of the behaviour of the threshold 10 freedom directions (FD_{10}). Subsequently, the behaviour of the building blocks is generalized.

Table 2: Normalized primary compliances

B. Block	Compliance type order	FD_{10}
A)	$\mathbf{T}_1 > \mathbf{w}_1 > \mathbf{T}_2 > \mathbf{T}_3 > \mathbf{w}_2 > \mathbf{w}_3$	2
B)	$\mathbf{T}_1 > \mathbf{T}_2 > \mathbf{w}_1 > \mathbf{T}_3 > \mathbf{w}_2 > \mathbf{w}_3$	3
D)	$\mathbf{T}_1 > \mathbf{w}_1 > \mathbf{T}_2 > \mathbf{T}_3 > \mathbf{w}_2 > \mathbf{w}_3$	2
C)	$\mathbf{T}_1 > \mathbf{w}_1 > \mathbf{w}_2 > \mathbf{T}_2 > \mathbf{T}_3 > \mathbf{w}_3$	1
E)	$\mathbf{T}_1 > \mathbf{w}_1 > \mathbf{T}_2 > \mathbf{T}_3 > \mathbf{w}_2 > \mathbf{w}_3$	3
F)	$\mathbf{T}_1 > \mathbf{w}_1 > \mathbf{T}_2 > \mathbf{w}_2 > \mathbf{T}_3 > \mathbf{w}_3$	2
H)	$\mathbf{w}_1 > \mathbf{T}_1 > \mathbf{T}_2 > \mathbf{T}_3 > \mathbf{w}_2 > \mathbf{w}_3$	6
G)	$\mathbf{T}_1 > \mathbf{w}_1 > \mathbf{T}_2 > \mathbf{T}_3 > \mathbf{w}_2 > \mathbf{w}_3$	6
I)	$\mathbf{T}_1 > \mathbf{w}_1 > \mathbf{w}_2 > \mathbf{w}_3 > \mathbf{T}_2 > \mathbf{T}_3$	4

The full characterization framework is based on the RasT unified stiffness approach and the introduced definitions, which shows; The describing equation with parameters description. The initial degree of compliance type order. The six degrees of freedom directions with unified compliances in the initial undeformed configuration. The three most dominant compliance vectors are shown during the three primary actuations. Three graphs showing the stationary unified compliances corresponding to the six degree of freedom directions against the travelled path of the point of interest along three primary actuations.

A) Hyperbolic parabolic: This building block characterization is shown in Figure 2. The Hyperbolic parabolic initially has one distinctive freedom direction, parallel to the y-axis, since η_{DC_2} is 0.15. Interestingly the eigentwist T_1 has limited axis drift along actuation w_{DC_1} , while the stiffness is not increasing. Actuation w_{DC_2} initially results in the translation in the direction of w_1 , however due to parasitic movement the resulting point of interest path is similar to actuation w_{DC_1} . The threshold 10 freedom direction behaviour during three primary actuations are given as,

Act. w_{DC_1} : FD_{10} of two and type order remains the same.

The compliance of T_1 and w_1 increases at a rate so that η_{DC_2} remains 0.15.

Act. w_{DC_2} : FD_{10} of two and type order remains the same.

While the compliance of T_2 increases it is insufficient to become a FD_{10} .

Act. w_{DC_3} : FD_{10} becomes three, due to an increasing compliance of T_2 and T_3 and stiffening of T_1 .

B) Double parabolic: Interestingly the double parabolic shows similar initial behaviour to the Hyperbolic parabolic except for the fact that the double parabolic has an extra FD_{10} along the z-axis with an η_{DC_2} of 0.76 in the initial state.

w_{DC1}: FD_{10} changes from three to two, due to an increasing T_1 compliance.

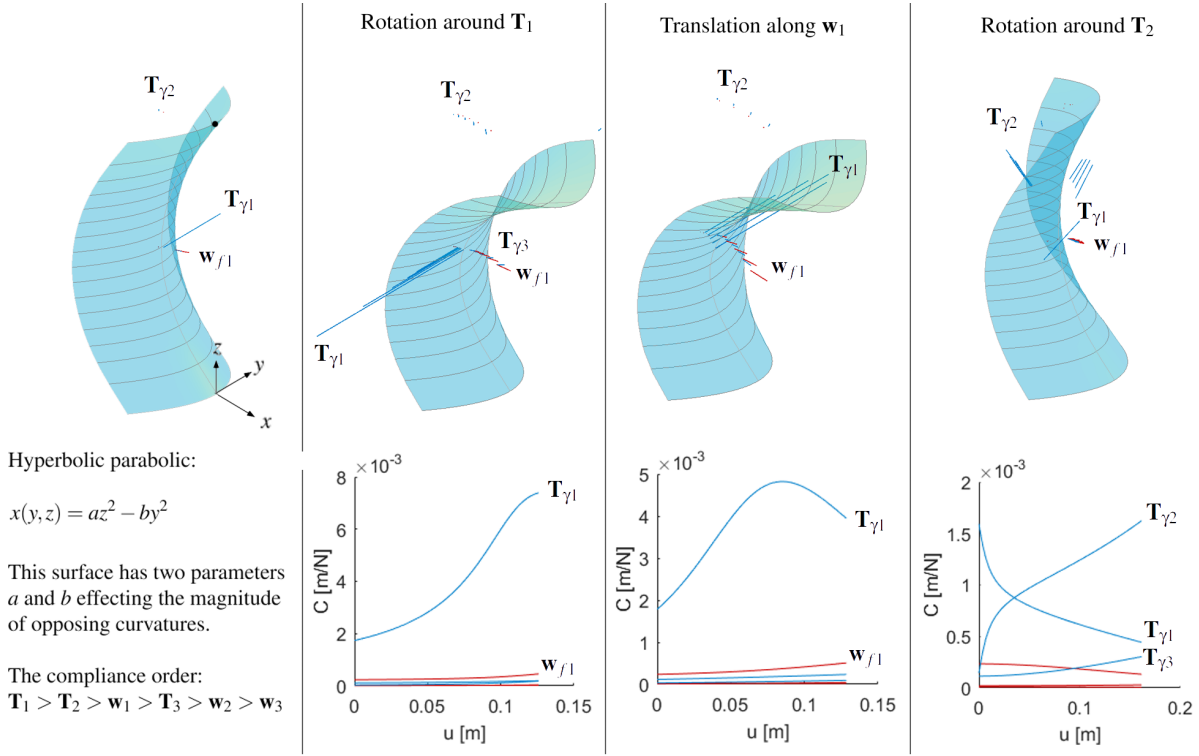


Fig. 2: Characterized Hyperbolic parabolic building block

w_{DC_2} : FD_{10} remains three, however due to a stiffening of T_1 the type order switches to T_1, T_2, w_1 .

w_{DC_3} : FD_{10} and type order remains the same.

C) Parabolic canoid: This building block which has the clearest distinction between freedom and constrained directions. As stated in Table 2 the building block has one FD_{10} . With a threshold $t = 100$ only has two FD_{100} . The tertiary compliance w_2 is thus at least 100 times less compliant than the primary compliance T_1 .

w_{DC_1} : FD_{10} of two and type order remains the same.

w_{DC_2} : FD_{10} changes from one to two, due to an increasing w_1 compliance.

w_{DC_3} : FD_{10} changes from one to two, due to an increasing T_1 compliance.

D) Shoe surface: Unique for this surface is that deformation in all three degrees of freedom results in a significant increasing secondary compliance, as it results in a type order rearrangement.

w_{DC_1} : FD_{10} changes from two to three, due to an increasing T_2 compliance, the type order switches to T_1, T_2, w_1 .

w_{DC_2} : FD_{10} changes from two to three, due to an increasing T_2 compliance, the type order switches to T_2, T_1, w_1 .

w_{DC_3} : FD_{10} remains two, however T_1 stiffens significantly, while T_2 and T_3 become more compliant, the resulting type order becomes T_2, T_3 .

E) Double corrugated: This building blocks shows the following behaviour.

w_{DC_1} : FD_{10} changes from three to two, due to an exponentially increasing T_2 compliance, while the other stay relatively constant. The type order switches to T_2, T_1 .

w_{DC_2} : FD_{10} changes from three to four, due to an increasing T_2 compliance and stiffening of T_3 the type order switches to T_2, T_1, w_1, T_3 .

w_{DC_3} : FD_{10} changes from three to four, as the compliance of T_3 slightly increases.

F) Single corrugated: This building block is the most compliant building block which is not based on the Helix.

w_{DC_1} : FD_{10} remains two, all value stay relatively constant.

w_{DC_2} : FD_{10} remains two, all value stay relatively constant.

w_{DC_3} : FD_{10} remains two, however the T_2 compliance increases exponentially while T_1 stiffens.

G) Helix: This building blocks shows minimal axis drift of the the primary and secondary compliance vectors T_1 and w_2 , while deforming in their directions, due to the circular symmetry.

w_{DC_1} : FD_{10} of six becomes four, since the T_1 compliance increases.

w_{DC_2} : FD_{10} remains six, since T_1 stiffens.

w_{DC_3} : FD_{10} remains six, since T_1 stiffens.

H) Sinusoidal helix: This building block shows similar behaviour as the regular helix, except for a smaller rotational compliance in the z -direction due to the single corrugation. Resulting in the only translational primary compliant building block.

w_{DC_1} : FD_{10} remains six, all value stay relatively constant, except for a switch in order of T_3 and T_2 .

w_{DC_2} : FD_{10} remains six, but T_1 and w_1 switch due to an increase of w_1 compliance.

w_{DC_3} : FD_{10} of six becomes four, since both T_1 and T_3 increase in compliance, the type order becomes T_1, w_2, T_3, w_2 .

I) Evolvent helicoid: This building blocks has a distinctive primary compliance T_1 as η_{DC_2} is 0.37, with minimal axis-drift during the corresponding deformation.

w_{DC_1} : FD_{10} remains four, all value stay relatively constant.

w_{DC_2} : FD_{10} of four becomes 6, since T_1 stiffens.

w_{DC_3} : FD_{10} of four becomes 6, since T_1 stiffens.

4.3 Generalization

The eigen-decomposition directions and corresponding stationary multipliers are derived from the compliance and stiffness matrix. Both the stiffness and compliance matrices are comprised of two matrices, considering the compliance matrix this is given as,

$$C_t = C_p + C_g \quad (12)$$

where C_p is the physical compliance matrix describing the initial compliance in undeformed configuration, which is described in Section 4.1. C_g is the geometrical stiffness matrix describing the compliance as a result of deformation, which described in Section 4.2. The physical compliance matrix is based on, assumed linear, material behaviour. While the geometric compliance matrix is based on the changing geometry, which behaves non-linearly. Similar statements can be made regarding the stiffness matrix. Non-linear behaviour of the compliance multipliers is therefore solely the result from the changing geometry.

Two important geometric phenomena are observed that cause change in compliance as a result of deformation at the point of interest. This includes change in:

- Second moment of area
- Mechanism length

These two phenomena are described in the next two subsections.

4.4 Second moment of area

Compared to compression, tension and shear, bending dominates the determination of primary compliance directions and magnitudes in compliant shell mechanisms [3]. The second moment of area contributes significantly to the corresponding bending compliance.

The second moment of inertia is a local geometrical property of cross-section with respect to an axis defined by the cross-sectional area and shape. The cross-sectional area stays relatively constant in shell deformations, while the cross sectional shape can vary significantly under deformation.

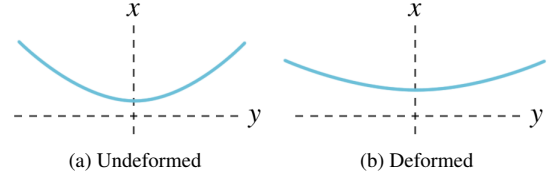


Fig. 3: Reduced second moment of area I_{min} cross section xy -plane at height T_1 of the double parabolic illustrated

The global bending compliance is defined by the integral of the local bending compliances along the length of the mechanism. More compliant segments of the mechanisms will therefore take account for more deformation [3].

Actuation in the primary compliance direction of the double parabolic, as shown in Figure 2, illustrates the locally reduced minimum second moment of area at height T_1 . The Hyperbolic Parabolic deforms to the most favourable deformation state under the applied load. As the mechanism deforms the surface curvature parallel to T_1 decreases. This decreasing second surface curvature results in a locally decreasing second moment of area. The locally decreasing minimum second moment of area contributes to a globally decreasing primary compliance magnitude.

This is evidenced by the change in cross sectional shape of the double parabolic shown in Figure 3 but also numerically shown in Figure 2.

4.5 Mechanisms length

A changing mechanisms length also contributes significantly to bending compliance. The mechanisms length is defined as the shortest distance between the point of interest and the point of constraint. Longer mechanisms enable greater strain energy absorption and facilitate larger displacements and rotations with lower stresses and are more compliant [13].

The global bending compliance is defined by the integral of the local bending compliances along the length of the mechanism. Therefore, not considering the varying second moment of area, elongation of a mechanism contributes to the bending compliance.

The deformation in the primary compliance direction of the two corrugated shells, presented in Figure 1, illustrates the effect of the mechanism length on the compliance. The corrugations along the z -axis between the single and the double corrugated shell are mirrored. Actuation in the same direction around T_1 for both corrugated shells has different effects on the mechanism length. Where actuation in the same direction around T_1 for the single corrugated shell increases the average corrugation curvature, the opposite behaviour is observed in the double corrugated shell. The change in curvature of both mechanism influences the mechanism length.

The increased mechanism length of the single corrugated shell, presented in Figure 1, actuated in the primary compliance direction is illustrated in Figure 3.

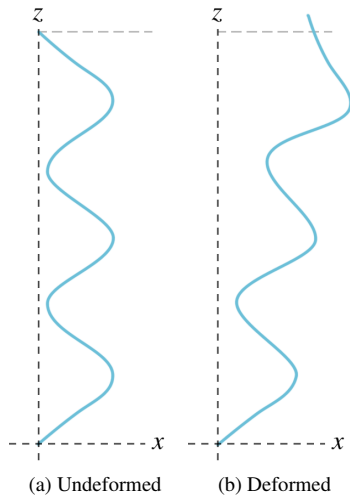


Fig. 4: Increased mechanism length illustrated at the zx -plane cross section of the single corrugated shell

5 Discussion

While compliance ellipsoids capture and illustrate behaviour intuitively [1], they do not address the coupling between translations and rotations. Additionally, due to different units, the rotational and translational ellipsoids are not comparable.

The unified stiffness characterization method, used in this paper, addresses coupling and is able to compare all degrees of freedom within and between mechanism [10].

In this paper, we introduced degree of compliance ratios which are able to quantify the relation between all six degrees of freedom in terms of compliance. The threshold freedom direction allows for a consistent freedom and constraint direction assessment of multiple building blocks. The normalized primary compliance ratio is used to quantify the relationship between all building blocks in terms of primary compliance. These definitions could not be defined without the introduction of the unified stiffness method.

To create a more meaningful comparison between building blocks, for further research, we would recommend normalizing the shell size with respect to their shortest internal length, defined by the shortest distance through the mechanism from the point of interest to the constraint edge. This would make the research variable, the geometrical shape, a larger differentiator in terms of compliance.

Presenting the behaviour of six degrees of freedom under large deformations on paper is limited due to space. More information can be accumulated in Appendix B. The principles of the characterization framework can be used include behaviour along the deformation in both directions of all the degrees of freedom.

Applying the eigen-decomposition, the unified stiffness, the degree of compliance ratio's and the threshold freedom directions on the promising building blocks results in a valuable library, containing uniquely described behaviour, such as zero axis drift, parasitic movement, increasing compli-

ances during deformation and distinctive single degrees of freedom shells.

6 Conclusion

This paper introduces definitions which give deeper insight in spatial compliant shell mechanism behaviour in an intuitively manner. A characterization framework is introduced, based on new definitions, able to capture the behaviour of all six kinematic degrees of freedom during the deformation in the three primary compliance directions. The characterization framework is applied to promising building blocks and results in interesting and unique described behaviour useful for spatial mechanism design subjected to large deformations. The observed behaviour is generalized based on the characterization by identifying important factors influencing the compliance.

Acknowledgements

The authors gratefully acknowledge support from NSF No. IIS - 1527133 as well as STW (HTSM-2012 12814: ShellMech) for the financial support of this project.

References

- [1] J.P.A. Nijssen, G. Radaelli, C. K., and Herder, J., 2016. "Overview and kinematic characterization of compliant shell mechanism building blocks".
- [2] Howell, L. L., 2001. *Compliant mechanisms*. John Wiley & Sons.
- [3] Radaelli, G., and Herder, J., 2017. "Gravity balanced compliant shell mechanisms". *International Journal of Solids and Structures*, **118**, pp. 78–88.
- [4] Kim, C. J., 2005. "A conceptual approach to the computational synthesis of compliant mechanisms.". PhD thesis.
- [5] Radaelli, G., and Herder, J. L., 2014. "Isogeometric shape optimization for compliant mechanisms with prescribed load paths". *Proceedings ASME IDETC/CIE*.
- [6] Seffen, K. A., 2012. "Compliant shell mechanisms". *Phil. Trans. R. Soc. A*, **370**(1965), pp. 2010–2026.
- [7] Pellegrino, S., 2005. "Bistable shell structures". In Proc. 46th AIAA/ASME/ASCE/AHS/ASC Structures, Structural Dynamics and Materials Conf., Austin, TX, 18â 21 April 2005.
- [8] Lipkin, H., and Patterson, T., 1992. "Geometric properties of modelled robot elasticity: Part idecomposition". In Proceedings of ASME Design Technical Conferences, pp. 187–193.
- [9] Chasles, M., 1830. "Note sur les propriétés générales du système de deux corps semblables entr'eux et placés d'une manière quelconque dans l'espace; et sur le déplacement fini ou infiniment petit d'un corps solide libre". *Bulletin des Sciences Mathématiques, Férussac*, **14**, pp. 321–26.
- [10] J.R. Leemans, C.J. Kim, W. v. d. S., and Herder, J., 2018. "Unified stiffness characterization of non-linear

compliant shell mechanisms”. *Proceedings AMSE IDETC/CIE*.

- [11] J.P.A. Nijssen, G. Radaelli, C. K., and Herder, J., 2016. “Design and analysis of a shell mechanism based two-fold force controlled scoliosis brace”.
- [12] Piegl, L., and Tiller, W., 2012. *The NURBS book*. Springer Science & Business Media.
- [13] Jutte, C. V., and Kota, S., 2008. “Design of nonlinear springs for prescribed load-displacement functions”. *Journal of Mechanical Design*, **130**(8), p. 081403.
- [14] Krivoschapko, S. *Encyclopedia of analytical surfaces*.
- [15] Norman, A., Seffen, K., and Guest, S., 2008. “Multistable corrugated shells”. In Proceedings of the Royal Society of London A: Mathematical, Physical and Engineering Sciences, Vol. 464, The Royal Society, pp. 1653–1672.
- [16] Norman, A., Seffen, K., and Guest, S., 2009. “Morphing of curved corrugated shells”. *International Journal of Solids and Structures*, **46**(7-8), pp. 1624–1633.
- [17] Gurevich, I., and Jolanta, T., 2015. “1.2. 1 catalan surfaces”. *Encyclopedia of Analytical Surfaces*, **2007**, p. 77.

Appendix A: Building block surface equations

A) Hyperbolic parabolic: The surface equation is given as,

$$x(y, z) = az^2 - by^2 \quad (13)$$

This negative Gaussian curvature surface has parameters a and b , which affect the magnitude of the two curvatures.

B) Double parabolic: The surface equation is given as,

$$x(y, z) = az^2 + by^2 \quad (14)$$

This positive Gaussian curvature surface has parameters a and b , which affect the magnitude of the two curvatures.

C) Parabolic Conoid: The surface equation as described in [14] is defined as,

$$x(y, z) = z\sqrt{\frac{a^2 - y^2}{2}} \quad (15)$$

The a parameter affects the slope of the centreline.

D) Shoe surface: The surface equation as described in [15] is given as,

$$x(y, z) = a\frac{z^3}{2} + b\frac{y^2}{2} \quad (16)$$

The a parameter affects the cubic curvature and b parameter affects the parabolic curvature.

E) Double corrugated shell: The surface equation as described in [16] is given as,

$$x(y, z) = -a(y - b)^2 - c\cos\left(\frac{n\pi z}{d}\right) + ab^2 \quad (17)$$

Where a is the height of the second curve, b is half the width, c is half of the amplitude of the corrugation and n effects the number of corrugations.

F) Single corrugated shell: The surface equation as described in [14] is given as,

$$x(y, z) = -c\cos\left(\frac{n\pi z}{d}\right) \quad (18)$$

The n parameter effects the number of corrugations, the c parameter effects the amplitude of the corrugation and d effects the width of a corrugation.

G) The Helix: The surface equation given in [14] is described by the following system of equations,

$$x(u, v) = a\cos(v) \quad (19)$$

$$y(u, v) = a\sin(v) \quad (20)$$

$$z(u, v) = cv + u \quad (21)$$

Where u and v effect the width and length of the helix. The a parameter defines the radius of the helix and c the distance between the revolutions.

H) Sinusoidal helix: The surface equation described by the following system of equations,

$$x(u, v) = (a + c\cos\left(\frac{n\pi v}{d}\right))\cos(u) \quad (22)$$

$$y(u, v) = (a + c\cos\left(\frac{n\pi v}{d}\right))\sin(u) \quad (23)$$

$$z(u, v) = bu - v \quad (24)$$

The a parameter defines the radius, c the corrugation height, d the corrugations amplitude and n the amount of corrugations.

I) Evolvent helicoid: The surface equation given in [17] is described by the following system of equations,

$$x(u, v) = a\cos(v) - au\sin\left(\frac{v}{m}\right) \quad (25)$$

$$y(u, v) = a\cos(v) - au\cos\left(\frac{v}{m}\right) \quad (26)$$

$$z(u, v) = bv + \frac{bu}{m} \quad (27)$$

Where u and v effect the width and length of the helix. The a parameter defines the radius of the mechanism and m the the height and angle of the spiral.

Discussion

This discussion is subdivided into categories discussing the design strategy, characterization theory, experiment and library and finally the potential for generalization of this work. Each sections discussing a chapter starts with a paragraph stating general and thesis specific contributions, followed by a paragraph recommending future work.

Design strategy

Previous research into compliant scoliosis braces utilizing compliant mechanisms, did not account for brace-tissue interaction, resulting in difficult to validate braces [6, 15]. To increase the ability to validate the brace, the in Chapter 2 proposed strategy does take into account brace-tissue interaction. This allows potential designs that follow from the proposed strategy to be validated in terms of correction efficiency using BraceSim [2].

In the current work, we take brace-tissue interaction into account at the cost of omitting the promising force-controlled correction strategy [1]. After validation of a displacement-based compliant scoliosis brace, it is recommended to research the potential of including a force-controlled correction strategy. Chapter 2 introduces a case study to illustrate the presented strategy. However, the case study patients motion characteristics were unavailable, therefore completed by the scaled motion characteristics of a patient with a similar spinal curvature. This is based on the assumption that both patients have similar bend characteristics and that the captured motion characteristics can be scaled. Ideally both the correction and motion analysis is done on the same patient to avoid the necessity of this assumption. The load design specifications are based on BraceSim, which analyses the efficiency of the brace in neutral posture. However, since the compliant scoliosis allows the patient to bent, the correctional loads in bent positions should also be researched. This can be done experimentally or by modifying the finite element model of our collaborators from the École Polytechnique de Montréal [2]. To translate the design specifications into a final design, Chapter 2 recommends research into characterization theory and synthesis methods of non-linear compliant shell mechanisms. The development and utilization of characterization theory is presented in Chapters 3, 4 and 5.

Characterization Framework & Theory

Systematic design methods to design shell mechanisms that satisfy the presented design specifications are not available in the literature. Therefore chapter 3 introduced a non-linear characterization method for compliant shell mechanisms that potentially leads to a design method for these mechanisms. The characterization method formulated in this work has benefits compared to existing methods. Previously available characterization methods did not address the coupling between rotations and translations [8]. Furthermore available methods were only able to separately compare rotational kinematic degrees of freedom and translational kinematic degrees of freedom, within one mechanism [6]. This work has enabled the comparison of rotational and translational compliances with each other by introducing a unification variable. Existing methods introduced arbitrarily chosen unification variables [17], while this work introduced two consistently derived physically meaningful unification lengths which include coupling. The presented characterization theory has the potential to be used to develop a synthesis method to design compliant shell mechanisms which could match the design specifications presented in 2.

Since the presented characterization can be applied on mechanisms subjected to large deformations it is recommended to research the influence of material non-linearities in addition to the described geometrical non-linearities. Chapter 3 recommends to experimentally validate the characterization theory and utilize the characterization theory to develop a library of systematically characterized mechanisms. This is addressed in Chapters 4 and 5.

Characterization Experiment

This demonstrates the feasibility of producing compliant shell mechanisms with modelled unified stiffness characteristics. However, there is a difference observed in the modelled and measured quantitative results, explained by unwanted pre-loading and introduced compliance in the measurement set-up. As well as anisotropy and thickness variation of the physical model as a result of the production process.

It is recommended to do a sensitivity analysis on the presented effects influencing the discrepancy between the computationally and experimentally determined unified stiffness. It is therefore recommended to integrate these effects into the computational model. Furthermore, it is recommended to validate the assumed material properties using a tensile test. To reduce the result discrepancy between the physical and computational model, the measurement set-up should be designed with more focus on stiffness in the x and y rotational and translational direction. The presented strategy to experimentally determine the unified stiffness has the potential to fully determine Lipkin's eigen-decomposition. [11]. A complete eigen-decomposition can be used to construct the 6x6 tangent stiffness and compliance matrix of a spatial compliant mechanism. The determination of all eigen-twists and eigen-wrenches could be achieved by extending the displacement inducer with four additional degrees of freedom.

Characterization Framework & Library

The consistent comparison between all six kinematic degrees of freedom leads to the, in chapter 5, introduced definitions. These definitions define relationships of compliant mechanism properties not described in the literature. This includes compliance ratios, which are able to quantify the relation in terms of compliance between all six degrees of freedom. The threshold freedom direction, which allows for a consistent freedom and constraint direction assessment of multiple building blocks. The normalized primary compliance ratio, which is used to quantify the relationship between different building blocks in terms of primary compliance. The non-linear characterization theory presented in Chapter 3 and the introduced definition resulted in a characterization framework. Where previous libraries did not take into account coupling and non-linearity this library does [6]. However, the comprehensive library is associated with an increase in interpretation difficulty. The library contains compliant shell mechanism which potentially can be used to match the design specifications presented in Chapter 2.

In this work, the sizes of the shell mechanisms are normalized to allow for a fair comparison by fitting them into the same box. In future work, we would recommend normalizing the size with respect to their shortest internal length, defined by the shortest distance through the mechanism from the point of interest to the constraint edge. This would make the research variable, the geometrical shape, a larger differentiator in terms of compliance. It is also recommended to research the influence of material non-linearities in addition to the described geometrical non-linearities. Further research is necessary to develop a synthesis method to design with the presented compliant shell mechanisms. Such a synthesis method could be utilized to match compliant shell mechanisms with the design specifications presented in Chapter 2.

Generalization

Non-linearity is often avoided in engineering and treated as failure mode, while it can provide interesting and desired behaviour. Embracing non-linearity enlarges the design-space and enables cutting-edge designs. This work is focused on non-linear shell mechanisms, however, the characterization theory and framework potentially leads to systematic synthesis method for any non-linear static spatial compliant mechanism. This potential is briefly discussed in preliminary work shown in Appendix F. Further research is necessary for series, parallel and hybrid conjunctions of building blocks. A systematic synthesis method for non-linear spatial compliant mechanisms could be used to create conceptual designs. Using shape and size optimization algorithms conceptual designs could be optimized to reduce the last discrepancy between actual and desired behaviour. The potential of the work presented can be used, but is not limited, to the design a compliant scoliosis brace.

Conclusion

This work has presented a strategy to reduce the complexity of a bio-mechanical compliant brace design problem into an isolated mechanical engineering problem. The main kinematic qualitative functional requirements are converted into quantitative design specifications for a spatial compliant mechanism, as shown through an example patient. In future work generated concepts, based on the design specifications, can be validated using proven BraceSim software.

A comprehensive characterization method is introduced that takes non-linear behaviour into account, considers coupling and allows the comparison of stiffness between all six degrees of freedom. The characterization allows the comparison of compliance between degrees of freedom of within and between mechanisms. With this introduced comprehensive comparison the opportunity rises to order all degrees of freedom, within and between mechanisms in terms of compliance. The most predominant degrees of freedom can now be identified along the trajectory of large deflections of compliant mechanisms. The characterization, presented in this paper, can be done for any mechanism which has a symmetric positive definite non-singular compliance matrix. This includes both compliant flexure and shell mechanisms. An experiment has shown that the unified stiffness corresponding to an eigen-twist and eigen-wrench of physical and computational model can be determined experimentally within the same order of magnitude.

Furthermore, this work introduces definitions which give a deeper insight into spatial compliant shell mechanism behaviour in an intuitive manner. A characterization framework, based on the introduced characterization method and the introduced definitions, able to capture the behaviour of all six kinematic degrees of freedom along the trajectory of deformation in the three primary compliance directions. The characterization framework is applied to promising building blocks and results in interesting and unique described behaviour useful for spatial mechanism design subjected to large deformations. The observed behaviour is generalized based on the characterization by identifying important phenomena influencing the compliance.

In conclusion, by translating the main functional requirements of a compliant scoliosis brace into design specifications of a compliant shell mechanism. Together with the introduction of characterization theory, an experiment and a characterized library of compliant shell mechanisms, which potentially leads to a synthesis method. This therefore work enhances the design process of a compliant scoliosis brace.

II

Appendix

A

Additional Paper Linear Characterization Theory

Paper: Unified Rotational and Translational Stiffness Characterization of Compliant Mechanisms

This paper is accepted and will be published at the ASME 2018 International Design Engineering Technical Conferences & Computers and Information in Engineering Conference IDETC/CIE 2018.

DETC2018-85251

**DRAFT: UNIFIED ROTATIONAL AND TRANSLATIONAL STIFFNESS
CHARACTERIZATION OF COMPLIANT SHELL MECHANISMS**

Joost R. Leemans

Dep. of Precision and Microsystems Engineering
Delft University of Technology
Delft, Zuid-Holland 2628CD
The Netherlands
Email: j.r.leemans@tudelft.nl

Charles J. Kim*

Dep. of Mechanical Engineering
Bucknell University
Lewisburg, Pennsylvania 17837
Email: cjk019@bucknell.edu

Werner W.P.J. van de Sande

Dep. of Precision and Microsystems Engineering
Delft University of Technology
Delft, Zuid-Holland 2628CD
The Netherlands
Email: w.w.p.j.vandeSande@tudelft.nl

Just L. Herder

Dep. of Precision and Microsystems Engineering
Delft University of Technology
Delft, Zuid-Holland 2628CD
The Netherlands
Email: j.l.Herder@tudelft.nl

ABSTRACT

Compliant shell mechanisms utilize spatially curved thin-walled structures to transfer or transmit force, motion or energy through elastic deformation. To design with spatial mechanisms designers need comprehensive characterization methods, while existing methods fall short of meaningful comparisons between rotational and translational degrees of freedom. This paper presents two approaches, both of which are based on the principle of virtual loads and potential energy, utilizing properties of screw theory, Plücker coordinates and an eigen-decomposition, leading to two unification lengths that can be used to compare and visualize all six degrees of freedom directions and magnitudes of compliant mechanisms in a non-arbitrary physically meaningful manner.

INTRODUCTION

The spatial geometry of compliant shell elements makes them useful as building blocks for spatial mechanism design. Researching the behaviour of compliant shell elements is done both analytically, as can be seen in the work of Seffen [1], Pellegrino [2] and computationally as can be seen in work of Radaelli & Herder [3,4]. The difficulty of characterizing compliant shell mechanisms lies in the intertwined kinematics and kinetics.

To design mechanisms designers need insight into their kinematics. In the field of rigid body mechanisms this is often characterised by the exact degrees of freedom describing the constraint and free motion directions. Compliant shell mechanisms do not have clear distinctive constraint and free motion directions, since motion tendencies are determined by the relative compliance of the mechanisms.

In order to characterize compliant shell mechanisms we shall discuss the relative compliances of the kinematic degrees of freedom, for spatial compliant mechanisms defined by Nijssen [5] as,

*Address all correspondence to this author.

”The motion tendency of a mechanism in 3D space, defined by the relationship between the three rotational and three translational compliances”

Relative compliances refer to the compliance ratios between the relative kinematic degrees of freedom. From here on referred to as the degrees of freedom. Determining and utilizing these degrees of freedom has proven useful in the characterization and synthesis of spatial mechanisms [4–6].

In related work, different methods are used to characterize the degrees of freedom of compliant mechanisms. Existing methods do not address the coupling between translations and rotations and thus discuss the rotations and translation separately, for example, by using compliance ellipsoids [4]. Methods to characterize principal compliance axes while including coupling were first introduced by Lipkin & Patterson [7], utilizing Plücker coordinates. Lin [8] introduced an independent derivation of principal compliance axes using hybrid coordinates. Two incomparable principle rotational and translational compliance directions and corresponding magnitude multiplier groups, containing all six degrees of freedom result from Lin and Lipkin’s derivation. A full comparison and order of the six degrees of freedom would give deeper insight into kinematic characteristics, such as the determination of whether a mechanism is predominantly rotational or translational compliant. Methods to convert these multiplier groups into compatible units, introduce arbitrarily defined characteristic lengths [9], lacking a physical consistent meaning. This leads to non-robust solutions, since this arbitrarily chosen length represents a different physical distance per analysis. Consequently the resulting unified compliances are not comparable between mechanisms.

A method with comparable results to a section of this paper is introduced by Lin [8]. Lin’s derivation is based on a geometrical interpretation of hybrid coordinates to derive principal stiffness axes. The corresponding stiffnesses are converted to similar units based on the principle of potential energy. By introducing the principle of potential energy all directional information is lost, since energy is a scalar quantity. Lin’s method is used to optimize the gripping force of graspers, instead of characterizing compliant mechanisms.

This paper presents two approaches that utilize properties of screw theory, Plücker coordinates and Lipkin’s eigen-decomposition which lead to unified compliances. The unified compliances, consisting of two multiplier groups with identical units, facilitates a comparison between all six degrees of freedom compliance magnitudes in a non-arbitrarily insightful manner while including coupling. The unification is utilized in a spatial characterization compliant mechanisms.

After the introduction the paper continues, in Section , with background theory on Plücker coordinates, stiffness matrices and Lipkin’s eigen-decomposition. Section visualises Lipkin’s

eigen-decomposition. The background theory and visualisation are used to determine two approaches that lead to the unification of the compliances in Section . The unification is used to present a visual characterization of the kinematic behaviour of two well-known compliant flexure mechanisms as illustrated in Section . Section discusses the contribution made by this paper. A brief summary is given and a general conclusion is drawn in Section .

BACKGROUND

According to Chasles’ theorem [10] a displacement in three-dimensional space can be expressed in Plücker coordinates vector form as a twist \mathbf{T} containing linear $\vec{\delta}$ and angular $\vec{\gamma}$ displacements defined as,

$$\mathbf{T} = \begin{bmatrix} \vec{\delta}_i \\ \vec{\gamma}_i \end{bmatrix} = \begin{bmatrix} (\vec{r}_i \times \vec{\gamma}_i) + h_i \vec{\gamma}_i \\ \vec{\gamma}_i \end{bmatrix}, \quad i = 1, 2, 3 \quad (1)$$

This form expresses the translation in terms of a combination of angular displacement $\vec{\gamma}$ and the 3×1 location vector \vec{r}_i and h the pitch scalar. The Plücker coordinates in vector form are visualised in Figure 1

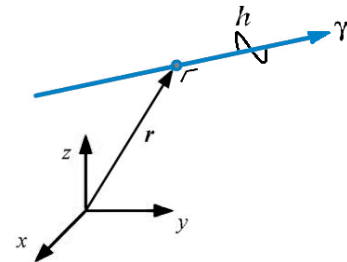


FIGURE 1: VISUAL REPRESENTATION OF THE PLÜCKER COORDINATES IN VECTOR FORM

The magnitude of the twist is defined as,

$$|\mathbf{T}| = \begin{cases} \sqrt{\vec{\delta} \cdot \vec{\delta}} & \text{if } \gamma = 0 \\ \sqrt{\vec{\gamma} \cdot \vec{\gamma}} & \text{otherwise} \end{cases} \quad (2)$$

and the direction of the twist is defined as the direction of the angular deformation. The dual of Chasles’ theorem is Poinot’s theorem. It states that any wrench can be constructed by a force and torque along the same axis [11]. In Plücker coordinate vector form the wrench \vec{w} contains the linear forces \vec{f} and the moment

couples $\vec{\tau}$ defined as,

$$\mathbf{w} = \begin{bmatrix} \vec{f}_i \\ \vec{\tau}_i \end{bmatrix} = \begin{bmatrix} \vec{f}_i \\ (\vec{b}_i \times \vec{f}_i) + d_i \vec{f}_i \end{bmatrix}, \quad i = 1, 2, 3 \quad (3)$$

where \vec{b}_i is the 3×1 location vector pitch d_i is the ratio of angular torque to linear force. The magnitude of the wrench is defined as,

$$|\mathbf{w}| = \begin{cases} \sqrt{\vec{\tau} \cdot \vec{\tau}} & \text{if } f = 0 \\ \sqrt{\vec{f} \cdot \vec{f}} & \text{otherwise} \end{cases} \quad (4)$$

and the direction of the wrench is seen as the direction of the force.

The relationship between the displacement and load of a specific point of interest can be described by the secant stiffness matrix \mathbf{K}_s or its inverse, the secant compliance matrix \mathbf{C}_s respectively, expressed as

$$\vec{w} = \mathbf{K}_s \Delta \vec{T}, \quad \Delta \vec{T} = \mathbf{C}_s \vec{w} \quad (5)$$

where \mathbf{K}_s and \mathbf{C}_s are the 6×6 secant stiffness and secant compliance matrix and $\Delta \vec{T}$ is an incremental displacement step. A secant matrix describing an infinitesimal incremental step is known as the tangent matrix, and it is defined as

$$K_t = \lim_{\Delta \vec{T} \rightarrow 0} K_s, \quad C_t = \lim_{\Delta \vec{T} \rightarrow 0} C_s \quad (6)$$

The tangent matrices describe a linearised configuration-dependant relation between the displacement and the load. The tangent stiffness and compliance matrices are composed of a physical and geometrical stiffness and compliance matrix. Non-linear behaviour can be analysed by using either the secant stiffness matrix or by making an incremental linearised analysis of each quasi-static-equilibrium based on the tangent stiffness matrix.

Any symmetric positive definite non-singular tangent stiffness K_t and tangent compliance matrix C_t can be decomposed into an eigen-system as described by Lipkin & Patterson [7]. The eigen-decomposition describes three translational and three rotational principal axes, with corresponding stationary multiplier values of the translational and rotational stiffness. Lipkin's eigen-decomposition of the tangent stiffness matrix K_t is defined as,

$$K_t = [\hat{\mathbf{w}}_f \ \hat{\mathbf{w}}_\gamma] \begin{bmatrix} k_f & 0 \\ 0 & k_\gamma \end{bmatrix} \begin{bmatrix} \hat{\mathbf{w}}_f \\ \hat{\mathbf{w}}_\gamma \end{bmatrix} \quad (7)$$

and the resulting tangent compliance matrix eigen-decomposition is defined as,

$$C_t = [\hat{\mathbf{T}}_f \ \hat{\mathbf{T}}_\gamma] \begin{bmatrix} a_f & 0 \\ 0 & a_\gamma \end{bmatrix} \begin{bmatrix} \hat{\mathbf{T}}_f \\ \hat{\mathbf{T}}_\gamma \end{bmatrix} \quad (8)$$

where for $i = 1, 2, 3$ multipliers $k_{\gamma i} > 0$ are the angular stiffnesses in the directions of the γ_i , multipliers $k_{f i} > 0$ are the translational stiffnesses in the directions of the f_i . The inverse of a translational stiffness gives the translational compliance,

$$a_{f i} = \frac{1}{k_{f i}} \quad (9)$$

and the inverse of a rotational stiffness gives the rotational compliance,

$$a_{\gamma i} = \frac{1}{k_{\gamma i}} \quad (10)$$

\mathbf{w}_f are the eigen-wrenches, these directions are also known as the wrench axes, defined as

$$\mathbf{w}_{f i} = \begin{bmatrix} \vec{f}_i \\ \vec{\tau}_i \end{bmatrix}, \quad i = 1, 2, 3 \quad (11)$$

Applying an eigen-wrench $\mathbf{w}_{f i}$ leads to an induced twist $\mathbf{T}_{f i}$ a pure translational displacement parallel to the force direction \vec{f}_i , the induced twists \mathbf{T}_f are defined as

$$\mathbf{T}_{f i} = \begin{bmatrix} a_{f i} \vec{f}_i \\ 0 \end{bmatrix}, \quad i = 1, 2, 3 \quad (12)$$

\mathbf{T}_γ are the eigen-twists, these directions are also known as the twist axes, defined as

$$\mathbf{T}_{\gamma i} = \begin{bmatrix} \vec{\delta}_i \\ \vec{\gamma}_i \end{bmatrix}, \quad i = 1, 2, 3 \quad (13)$$

Applying an eigen-twist $\mathbf{T}_{\gamma i}$ leads to an induced wrench $\mathbf{w}_{\gamma i}$ a pure moment parallel to the rotational direction $\vec{\gamma}_i$, the induced wrenches \mathbf{w}_γ are defined as

$$\mathbf{w}_{\gamma i} = \begin{bmatrix} 0 \\ k_{\gamma i} \vec{\gamma}_i \end{bmatrix}, \quad i = 1, 2, 3 \quad (14)$$

The above wrenches and twists are normalized with respect to the defined magnitudes to be used in the eigen-decompositions of Eqns. 7 and 8.

$$\hat{\mathbf{T}} = \frac{\mathbf{T}}{|\mathbf{T}|} \quad (15)$$

and

$$\hat{\mathbf{w}} = \frac{\mathbf{w}}{|\mathbf{w}|} \quad (16)$$

After the normalization of the twist and wrench eigen-decomposition described in Eqns. 2 and 4, the direct magnitude relation is lost. In terms of magnitude, the induced twists and wrenches are no longer a direct result of the eigen-wrenches and eigen-twists. After normalization, only the directional relations remain valid.

VISUALISATION OF THE EIGEN-DECOMPOSITION

To increase the understanding of the wrench and twist axes the eigen-decompositions is visualised. Nijssen [6] already plotted the three eigen-twist directions. In this section we introduce the visualisation of the eigen-wrench directions and include the corresponding stationary compliance multipliers. A compliant shell mechanism example is introduced which is fully constrained along the bottom edge and the point of interest at which C_f is determined is indicated by a black dot, as can be seen in Figure 2.

The acrylic-plastic shell mechanism is analysed as an IGA shell, with the following material properties; the Young Modulus is 3.2 GPa, the Poisson ratio is 0.35. The 2mm thick geometry is defined by NURBS [12], a third polynomial follows a 3×5 grid. Five coordinates are placed on three planes in $y = -0.05$, $y = 0$ and $y = 0.05$. The x and z coordinates are defined in Table 8.

TABLE 1: NURB COORDINATES CORRUGATED SHELL

Point	1	2	3	4	5
x	0.00	0.00	0.04	0.00	0.00
z	0.00	0.04	0.08	0.11	0.15

The three principle eigen-twist directions are shown in Figure 2a. A rotation of the point of interest around a twist axis plus a translation along this axis leads to pure parallel moments around this twist axes.

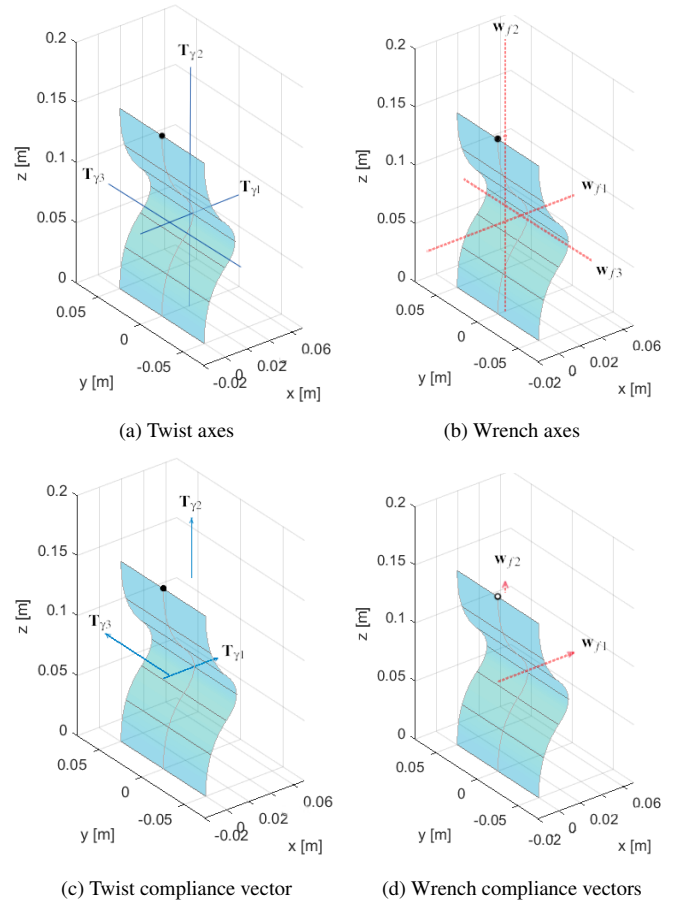


FIGURE 2: VISUAL REPRESENTATION EIGEN-DECOMPOSITION

The three principle eigen-wrench directions can be seen in Figure 2b. A force along a wrench axis plus a moment around this axis leads to a pure translation along the wrench axis.

Figures 2a and 2b both provide information on the twist and wrench spatial directions, while excluding the compliance and stiffness multipliers. Thus these figures do not show the magnitude of compliance corresponding to these directions. By plotting vectors along the directions of the wrench and twist axes with the length of their corresponding stationary compliance multipliers, both the direction and magnitude of compliance are visualised in an intuitive manner.

Figure 2c shows the vectors along the twist axes with the magnitude of the corresponding rotational compliance multipliers a_γ . The longer the vector the larger the rotational compliance around the twist axis that the vector represents.

Figure 2d shows the vectors along the wrench axes with the magnitude of the corresponding translational compliance multipliers a_f . The longer the vector the larger the translational com-

pliance along the wrench axis that the vector represents.

Figures 2d and 2c both provide the directional information of the twist and wrench axes and the corresponding compliance magnitude. In itself these are useful characterizations, however, the magnitudes of these vectors cannot be compared between the two Figures, as further discussed in Section .

UNIFICATION METHODS

The diagonal matrices of the decompositions in Eqns. 7 and 8 consist of the compliance and stiffness stationary multipliers corresponding to the wrench and twist axes. Considering the decomposition in Eqn. 8, the upper three stationary multipliers a_f are the translational compliances given as length per force, corresponding to a translation parallel to the wrench axis. The lower three stationary multipliers a_γ are the rotational compliances given as angle divided by force multiplied by length, corresponding to the rotation around the twist axis. The rotational and translational multipliers are not directly comparable due to their different units. To enable this comparison, we utilize unification variables, which will be defined based on equivalent compliance by virtual load or potential energy.

We will discuss two unification approaches, by converting the units of a_{f_i} into a_{γ_i} and the units of a_{γ_i} into a_{f_i} . The conversion of the units of a_{γ_i} into a_{f_i} can be done by expressing rotational compliance as an equivalent translational compliance at the point of interest using a unification length χ_i . The conversion of the units of a_{f_i} into a_{γ_i} can be done by expressing translational compliance at the point of interest as an equivalent rotational compliance using a unification length Ψ_i . In Equation form the unification approaches are given as,

$$\tilde{a}_{f_i} = \chi_i^2 a_{\gamma_i} \quad (17)$$

and,

$$\tilde{a}_{\gamma_i} = \frac{a_{f_i}}{\Psi_i^2} \quad (18)$$

We introduce two methods to obtain the unification lengths. The first method utilizes virtual load and displacements and the second method is based on the principle of potential energy. The strengths and weaknesses of both methods are discussed in Section .

RasT: Rotational as equivalent Translational compliance

The first approach expresses rotational compliance as an equivalent translational compliance at the point of interest. We call this the RasT approach. Both the virtual loads and potential energy are used separately to determine unification length χ_i .

The RasT approach using the virtual load method.

Converting the rotational compliance into an equivalent translational compliance at the point of interest using the virtual load method can be done in three consecutive steps.

- I Express δ_{eq_i} , an equivalent translation at the point of interest in terms of rotation around the twist axis.
- II Express F_{eq_i} , an equivalent virtual force at the point of interest in terms of the induced counteracting pure parallel moment couple corresponding to a rotation around the twist axis.
- III Express an equivalent translational compliance \tilde{a}_{f_i} , by dividing the expressions above to obtain the equivalent translational compliance. That is,

$$\tilde{a}_{f_i} = \frac{\delta_{eq_i}}{F_{eq_i}} \quad (19)$$

Figures 3 and 4 both show the point of interest of a spatial compliant mechanism as indicated by the black dot and one of the three principal twist axes \mathbf{T}_{γ_i} indicated by the blue line, used to explain the three steps.

Step I: Express δ_{eq_i} , equivalent translation. The equivalent translation at the point of interest is expressed in terms of a screw around the twist axis. The total translation corresponding to a rotation θ_i is a combination of displacement along the arc length around the twist axis δ_{r_i} and a translation along the twist axis δ_{h_i} . The resulting equivalent translation δ_{eq_i} , a path along a cylinder, is illustrated in Figure 3.

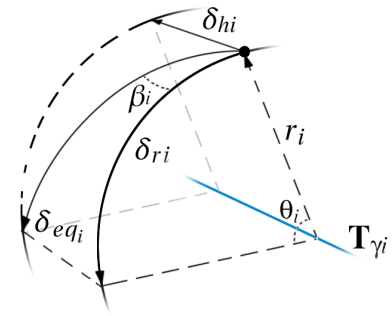


FIGURE 3: EQUIVALENT TRANSLATION GEOMETRY

The displacement along the arc at a radius can be expressed as the rotation multiplied by the radius, the arc-length. The radius that defines the displacement along the arc is the shortest distance between the point of interest and the twist axis. This length is defined in Plücker coordinates as the location vector r_i as shown

in Figure 1. The displacement along the arc-length is thus given as,

$$\delta_{ri} = |r_i|\theta_i \quad (20)$$

The point of interest translates along the twist axis, due to the pitch h_i , given by the pitch times the rotation,

$$\delta_{hi} = h_i\theta_i \quad (21)$$

The resulting displacement due to the two perpendicular displacements on a cylinder is calculated using the Pythagorean theorem. The equivalent translation expressed in terms of the corresponding rotation is thus given as,

$$\delta_{eqi} = \sqrt{(h_i^2 + |r_i|^2)}\theta_i \quad (22)$$

Step II: Express F_{eqi} , equivalent virtual force. The equivalent virtual force at the point of interest in the opposite direction of the equivalent displacement is expressed in terms of the induced moment corresponding to a rotation around the twist axis.

This is done by defining a virtual force F_m at distance r_i with a magnitude and direction which results in the same moment magnitude as the pure moment parallel corresponding to a rotation. By decomposing this virtual moment force vector, with one of the components in the direction of the equivalent translation determined in step I, the equivalent virtual force F_{eq} can be defined. The introduced virtual moment force vector F_m is given as,

$$F_{mi} = \frac{M_i}{|r_i|} \quad (23)$$

The geometry required to decompose the virtual moment force F_m to the equivalent virtual force F_{eq} in the opposite direction of the point of interest displacement is shown in Figure 4.

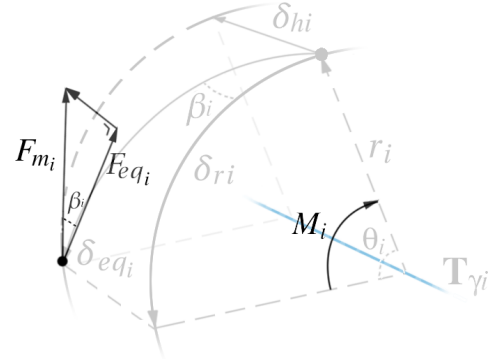


FIGURE 4: Equivalent virtual force geometry

where β is the angle between δ_{eqi} and $\delta_{\gamma ri}$, since the alternate interior angles between two parallel lines are equal, β_i also defines the angle between F_{mi} and F_{eqi} , which is defined as,

$$\beta_i = \frac{F_{mi}}{F_{eqi}} = \frac{\delta_{eqi}}{\delta_{\gamma ri}} = \frac{\sqrt{(h_i^2 + |r_i|^2)}\theta_i}{|r_i|\theta_i} \quad (24)$$

By combining Eqn. 23 and 24, the equivalent virtual force expressed in terms of the corresponding moment can be given as,

$$F_{eqi} = \frac{M_i}{\sqrt{(h_i^2 + |r_i|^2)}} \quad (25)$$

Step III: Express \tilde{a}_{fi} , the equivalent translational compliance. The third step is to substitute 22 and 25 with 19,

$$a_{fi} = \frac{\delta_{eqi}}{F_{eqi}} = (h_i^2 + |r_i|^2) \frac{\theta_i}{M_i} \quad (26)$$

The unification length χ_i follows from Eqn. 17 and 26,

$$\chi_i = \sqrt{h_i^2 + |r_i|^2} \quad (27)$$

The RasT approach using the potential energy method. To unify the rotational compliance multipliers $a_{\gamma i}$ into equivalent translational compliance multipliers \tilde{a}_{fi} the principle of potential energy can be used as well. The rotational energy is compared with the corresponding virtual equivalent translational energy due to the rotation.

The eigentwist induces a pure moment around the twist axis, therefore the corresponding potential energy is solely dependent

on the rotational stiffness and rotation. The potential energy of the eigentwist is defined as,

$$U_{\gamma_i} = \frac{1}{2} k_{\gamma_i} \theta_i^2 \quad (28)$$

By introducing an equivalent translational stiffness \tilde{k}_{f_i} and the equivalent translation δ_{eq_i} corresponding to the rotation given in Eqn. 22, we can express the stored energy as,

$$\frac{1}{2} k_{\gamma_i} \theta_i^2 = \frac{1}{2} \tilde{k}_{f_i} \delta_{eq_i}^2 \quad (29)$$

By substituting Eqn. 22 with 29 the equivalent translational stiffness can be defined as,

$$\tilde{k}_{f_i} = \frac{k_{\gamma_i}}{(h_i^2 + |r_i|^2)} \quad (30)$$

The inverse of the translational and rotational stiffness results in the translational and rotational compliance, as stated in Eqn. 9 and 10. The equivalent translational compliance of the rotational compliance is thus given as,

$$\tilde{a}_{f_i} = (h_i^2 + |r_i|^2) a_{\gamma_i} \quad (31)$$

From 17 and 31 follows the unification length,

$$\chi_i = \sqrt{h_i^2 + |r_i|^2} \quad (32)$$

which exactly matches Eqn. 27.

TasR: Translational as equivalent Rotational compliance

The second approach expresses the translational compliance as an equivalent rotational compliance, which we call the TasR approach. Converting the translational compliance into an equivalent rotational compliance at the point of interest can be done using both the TasR equivalent of the virtual load and the potential energy RasT approach. The virtual load method TasR equivalent steps are:

- I Express θ_{eq_i} , an equivalent rotation at the point of interest in terms of a translation parallel to the wrench axis.
- II Express M_{eq_i} , an equivalent virtual moment at the point of interest in terms of the counteracting force corresponding to a translation parallel to the wrench axis.

- III Express an equivalent rotational compliance \tilde{a}_{γ_i} , by dividing the expressions above to obtain the equivalent translational compliance.

The potential energy method TasR equivalent is done by introducing an equivalent rotational stiffness. This stiffness is defined in terms of the translational stiffness corresponding to the wrenches.

Both the virtual load and the potential energy TasR equivalent of the RasT methods result into the unification length,

$$\psi_i = \sqrt{|d_i^2| + b_i^2} \quad (33)$$

which has the same form as the unification length expressed in Eqn. 32.

Approach and method comparison

Both the virtual load method and the potential energy method result into the same unification lengths. The potential energy method is more straightforward, however, it gives less insight into the actual kinematics compared to the virtual load method. While the end results of both methods yield similar conclusions, the virtual load method includes interesting sub-steps with physical relevance. The sub-step results in themselves can form the basis for specific designs. Knowledge of the composition of the sub-steps provides the opportunity to vary parameters in an intelligent manner to achieve specific objectives. In addition, energy in any form is a scalar quantity. Using the introduced potential energy method all directional information is excluded.

The RasT unification approach characterizes a mechanism as if a point of interest will be displaced using solely forces. The RasT approach is physically comparable as if the point of interest is displaced, along the wrench and around the twist axis, using a ball-and-socket-joint while evaluating the travelled path and the reaction force. Consequently using the RasT approach pure decoupled rotations around the point of interest are impossible to excite, therefore the RasT approach cannot evaluate the corresponding compliance multipliers. The TasR approach characterizes a mechanism as if the less intuitive opposite is the case, when a point of interest will be displaced solely using torques. Consequently using the TasR approach the unified compliance values corresponding to eigen-wrenches that are pure forces in line with the point of interest cannot be evaluated.

In order to bypass degrees of freedom that are non-evaluable one could use either the TasR or RasT approach. If both approaches result in non-evaluable degrees of freedom magnitudes the combination of the two will give the best characterization. The RasT approach is more intuitive and accounts for the coupling of the rotations and translations by including twist pitch, hence Section will focus on this approach. However, both approaches in their context, separately or combined, are

a powerful characterization for comparing all six degrees of freedom.

CHARACTERIZATION

This Section shows the effectiveness and strength of the ability to characterize and compare all six degrees of freedom using the introduced unification lengths.

Unified compliance matrix

The unification lengths χ_i and Ψ_i result in unified stationary compliance multipliers, which can be represented in matrix form. In the case of the RasT approach, the unification length of Eqn. 27 is substituted with Eqn. 8. The rotational compliance multipliers are multiplied by the unification length squared ($h_i^2 + |r_i|^2$), which results in the equivalent translational compliance. In matrix form this produces the diagonal unified stationary translational compliance multiplier matrix $\tilde{\mathbf{a}}_f$ given as,

$$\tilde{\mathbf{a}}_f = \begin{bmatrix} a_{fi} & 0 \\ 0 & (|r_i|^2 + h_i^2)a_{\gamma i} \end{bmatrix} \quad (34)$$

In the case of the TasR approach, the unification length of Eqn. 33 substituted with Eqn. 8 the unified rotational compliance multiplier matrix $\tilde{\mathbf{a}}_\gamma$ is given as,

$$\tilde{\mathbf{a}}_\gamma = \begin{bmatrix} \frac{a_{fi}}{|b_i|^2 + d_i^2} & 0 \\ 0 & a_{\gamma i} \end{bmatrix} \quad (35)$$

To put it in the original context, the complete eigen-decomposition of the tangent compliance matrix, including the new unified compliance matrix for the RasT approach becomes,

$$\mathbf{C}_t = \begin{bmatrix} \hat{\mathbf{T}}_f & \hat{\mathbf{T}}_\gamma \end{bmatrix} \begin{bmatrix} I & 0 \\ 0 & \frac{1}{\sqrt{|r_i|^2 + h_i^2}} \end{bmatrix} \tilde{\mathbf{a}}_f \begin{bmatrix} I & 0 \\ 0 & \frac{1}{\sqrt{|r_i|^2 + h_i^2}} \end{bmatrix} \begin{bmatrix} \hat{\mathbf{T}}_f \\ \hat{\mathbf{T}}_\gamma \end{bmatrix} \quad (36)$$

and for the TasR approach the complete decomposition is given as,

$$\mathbf{C}_t = \begin{bmatrix} \hat{\mathbf{T}}_f & \hat{\mathbf{T}}_\gamma \end{bmatrix} \begin{bmatrix} |b_i|^2 + d_i^2 & 0 \\ 0 & I \end{bmatrix} \tilde{\mathbf{a}}_\gamma \begin{bmatrix} |b_i|^2 + d_i^2 & 0 \\ 0 & I \end{bmatrix} \begin{bmatrix} \hat{\mathbf{T}}_f \\ \hat{\mathbf{T}}_\gamma \end{bmatrix} \quad (37)$$

The Direction and unified compliance magnitude visualised. Vectors in the direction of the eigen-twists $\hat{\mathbf{T}}_i$ and the eigen-wrenches $\hat{\mathbf{w}}_i$ with the length of their corresponding values in the unified compliance matrix $\tilde{\mathbf{a}}_f$ or $\tilde{\mathbf{a}}_\gamma$ visualise the

comparable compliance directions. Using this visualisation the dominant compliance directions become evident.

The power of this method is shown through two well-described compliant flexure mechanisms. The first is designed to be predominately rotationally compliant, a cross pivot flexure mechanism. The second designed is to be predominately translationally compliant, a double parallel flexure mechanism with an intermediate body. The visualisation using the unified compliance matrix confirms the expected behaviour of these well-described mechanisms.

Both mechanisms are analysed in SPACAR, which is a program for dynamic analysis of flexible spatial mechanisms and manipulators [13]. The mechanisms contain blue spring steel flexures with the following properties; the Young Modulus is 500 MPa, the Poisson ratio is 0.3 and the geometry is $75 \times 15 \times 0.5$ mm.

Cross pivot flexure mechanism

The cross pivot flexure mechanism consists of two perpendicular flexures and two parallel rigid bodies. The lower rigid body is fully constrained and the centre of the upper rigid body is considered to be the point of interest. Using SPACAR the 6x6 tangent compliance matrix \mathbf{C}_t is determined. The introduced, in Section , visualisation of Lipkin's eigen-decomposition is applied. Figure 5 shows the twist and wrench compliant axes of the mechanism.

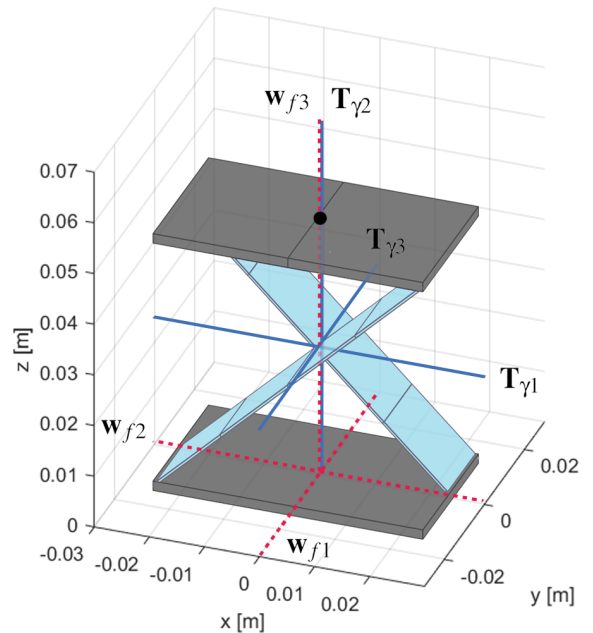


FIGURE 5: PRINCIPAL COMPLIANCE DIRECTIONS OF THE CROSS PIVOT FLEXURE MECHANISM

The stationary translational compliance multipliers corresponding to the wrench axes are given in Table 2.

TABLE 2: COMPLIANCE MAGNITUDES AND CORRESPONDING WRENCH AXES OF THE CROSS PIVOT FLEXURE

Corresp. wrench	Translational compliance [a_{fi}]
\mathbf{w}_{f1}	<u>$2.50 \cdot 10^{-07}$ m/N</u>
\mathbf{w}_{f2}	$2.00 \cdot 10^{-08}$ m/N
\mathbf{w}_{f3}	$2.00 \cdot 10^{-08}$ m/N

The largest translational compliance multiplier is underlined and corresponds to wrench \mathbf{w}_{f1} . The stationary rotational compliance multipliers and the pitches corresponding to the twist axes are given in Table 3.

TABLE 3: COMPLIANCE MAGNITUDES AND CORRESPONDING TWIST AXES OF THE CROSS PIVOT FLEXURE

Corresp. twist	Rotational comp. [a_{γ_i}]	Pitch [h_i]
$\mathbf{T}_{\gamma1}$	$1.06 \cdot 10^{-03}$ rad/Nm	$7.50 \cdot 10^{-03}$ m
$\mathbf{T}_{\gamma2}$	$1.06 \cdot 10^{-03}$ rad/Nm	$7.50 \cdot 10^{-03}$ m
$\mathbf{T}_{\gamma3}$	<u>$4.80 \cdot 10^{-01}$ rad/Nm</u>	$0.00 \cdot 10^{-00}$ m

The largest rotational compliance multiplier is underlined and corresponds to twist axis $\mathbf{T}_{\gamma3}$. As discussed, the compliance multipliers in Tables 2 and 3 cannot be compared directly, therefore the unified compliance matrices are introduced. Figure 6 shows compliance vectors along the twist and wrench axes with unified compliance magnitudes \tilde{a}_f resulting from the RasT approach.

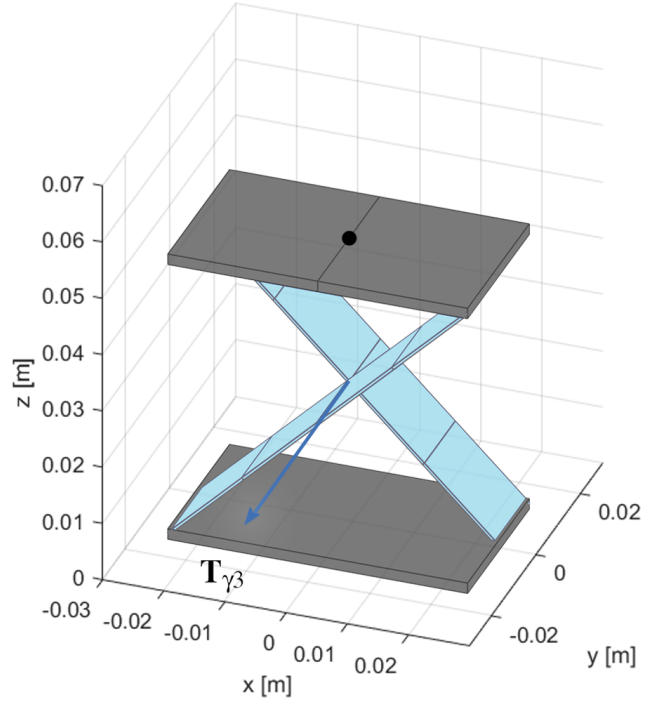


FIGURE 6: UNIFIED COMPLIANCE VECTORS OF THE CROSS PIVOT FLEXURE MECHANISM

As can be seen in Figure 6, the largest vector by orders of magnitude is in the direction of twist axis $\mathbf{T}_{\gamma3}$ as is expected, originating from the crossing of the flexures in the y-direction parallel to these flexures. The other compliance vectors are too small to visualise using linear magnitude representation. The corresponding comparable unified compliance magnitudes are given in Table 4.

TABLE 4: TWIST AND WRENCH AXES WITH CORRESPONDING UNIFIED COMPLIANCE MAGNITUDES OF THE CROSS PIVOT FLEXURE MECHANISM

Corresp. axes	Unified compliance [\tilde{a}_{fi}]
\mathbf{w}_{f1}	$2.50 \cdot 10^{-07}$ m/N
\mathbf{w}_{f2}	$2.00 \cdot 10^{-08}$ m/N
\mathbf{w}_{f3}	$2.00 \cdot 10^{-08}$ m/N
$\mathbf{T}_{\gamma1}$	$8.08 \cdot 10^{-07}$ m/N
$\mathbf{T}_{\gamma2}$	$5.99 \cdot 10^{-08}$ m/N
$\mathbf{T}_{\gamma3}$	<u>$3.38 \cdot 10^{-04}$ m/N</u>

As can be seen in Table 4, the multipliers are at least three orders smaller than the most underlined multiplier corresponding to the most dominant rotational degree of freedom. The cross flexure mechanism is thus dominantly rotational compliant which is consistent with the objective of the design. The total relative degree of freedom order based on the unified compliance multipliers following from the RasT approach is given as,

$$\mathbf{T}_{\gamma 3} \gg \mathbf{T}_{\gamma 1} > \mathbf{w}_{f1} > \mathbf{T}_{\gamma 2} > \mathbf{w}_{f3}/\mathbf{w}_{f2} \quad (38)$$

Double parallel flexure mechanism

The second mechanism is designed to be predominately translationally compliant, a double parallel flexure mechanism with an intermediate body. Figure 7 shows the twist and wrench axes of the mechanism.

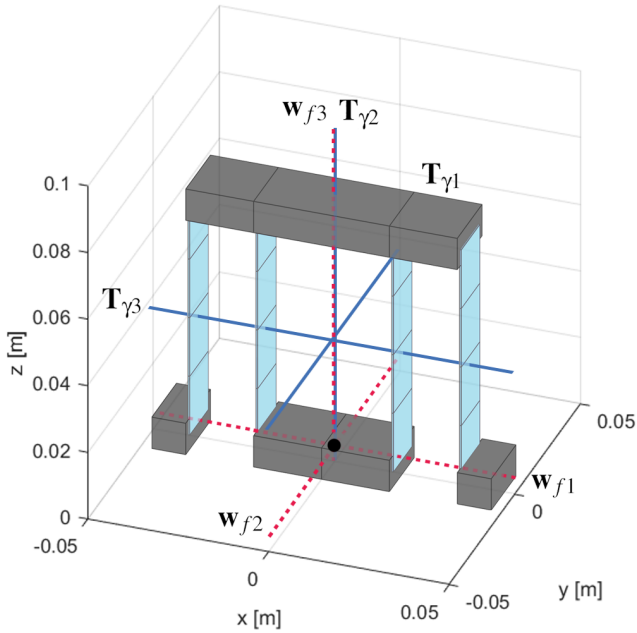


FIGURE 7: PRINCIPAL COMPLIANCE DIRECTIONS OF THE DOUBLE PARALLEL FLEXURE MECHANISM

The translational compliance multipliers corresponding to the wrench axes are given in Table 5 and the rotational compliance multipliers and the pitches corresponding to the twist axes are given in Table 6.

TABLE 5: COMPLIANCE MAGNITUDES AND CORRESPONDING WRENCH AXES OF THE DOUBLE PARALLEL FLEXURE MECHANISM

Corresp. wrench	Translational Compliance [a_{fi}]
\mathbf{w}_{f1}	<u>$4.50 \cdot 10^{-04}$ m/N</u>
\mathbf{w}_{f2}	$5.00 \cdot 10^{-07}$ m/N
\mathbf{w}_{f3}	$2.00 \cdot 10^{-08}$ m/N

TABLE 6: COMPLIANCE MAGNITUDES AND CORRESPONDING TWIST AXES OF THE DOUBLE PARALLEL FLEXURE MECHANISM

Corresp. twist	Rotational Compliance [$a_{\gamma i}$]	Pitch [h_i]
$\mathbf{T}_{\gamma 1}$	$3.12 \cdot 10^{-05}$ rad/Nm	0.00 m
$\mathbf{T}_{\gamma 2}$	$7.80 \cdot 10^{-04}$ rad/Nm	0.00 m
$\mathbf{T}_{\gamma 3}$	<u>$1.07 \cdot 10^{-03}$ rad/Nm</u>	0.00 m

The largest translational and rotational compliance multipliers are underlined and correspond to wrench \mathbf{w}_{f1} and twist $\mathbf{T}_{\gamma 3}$. The compliance multipliers in Tables 5 and 6 can only be compared directly using the unified compliances \tilde{a}_{γ} and \tilde{a}_f . Figure 8 shows the unified compliance vectors along the twist and wrench axes with the corresponding unified compliances as magnitudes. As can be seen in Figure 8, the largest compliance vector is in the direction of wrench axis \mathbf{w}_{f1} as is expected. It originates from the point of interest in the x-direction perpendicular to the face of the flexures. The other compliance vectors are too small to visualise using linear magnitude representation. The corresponding unified compliance magnitudes resulting from both approaches are given in Table 7. As can be seen in Table 4, resulting from both approaches, the largest unified compliance magnitude, corresponding to the most dominant degree of freedom, is at least two orders larger than the other magnitudes. The double flexure mechanism is thus dominantly translational compliant consistent with the objective of the design. The total degree of freedom order based on the unified compliance multipliers \tilde{a}_{fi} following from the RasT approach is,

$$\mathbf{w}_{f1} \gg \mathbf{T}_{\gamma 3} > \mathbf{w}_{f2} > \mathbf{T}_{\gamma 1} > \mathbf{w}_{f3} \quad (39)$$

As discussed in Section , the fully decoupled rotational degree of freedom $\mathbf{T}_{\gamma 2}$ is a non-evaluable value using the RasT approach.

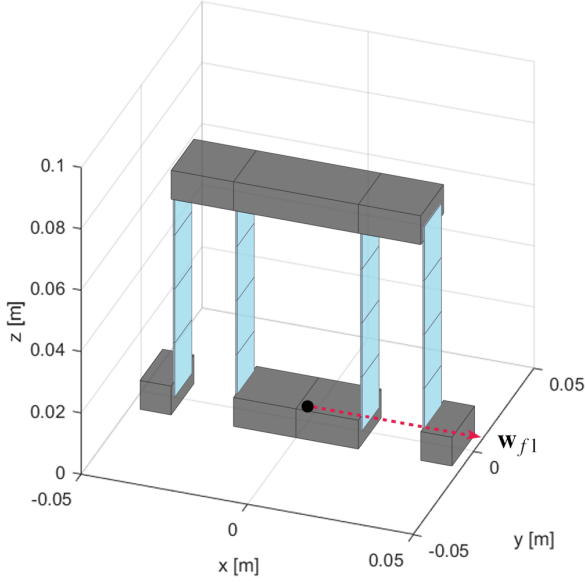


FIGURE 8: UNIFIED COMPLIANCE VECTORS OF THE DOUBLE PARALLEL FLEXURE MECHANISM

TABLE 7: TWIST AND WRENCH AXES WITH CORRESPONDING UNIFIED COMPLIANCES OF THE DOUBLE PARALLEL FLEXURE MECHANISM

Corresp. axis	Unified compl. [\tilde{a}_{fi}]	Unified compl. [\tilde{a}_{γ_i}]
\mathbf{w}_{f1}	$4.50 \cdot 10^{-4}$ m/N	3.20×10^1 rad/Nm
\mathbf{w}_{f2}	$5.00 \cdot 10^{-7}$ m/N	$3.56 \cdot 10^{-4}$ rad/Nm
\mathbf{w}_{f3}	$2.00 \cdot 10^{-8}$ m/N	-
$\mathbf{T}_{\gamma 1}$	$4.40 \cdot 10^{-8}$ m/N	$3.12 \cdot 10^{-5}$ rad/Nm
$\mathbf{T}_{\gamma 2}$	-	$7.80 \cdot 10^{-4}$ rad/Nm
$\mathbf{T}_{\gamma 3}$	$1.50 \cdot 10^{-6}$ m/N	$1.07 \cdot 10^{-3}$ rad/Nm

More insight is accumulated using the TasR approach. The total degree of freedom order based on the unified compliance multipliers \tilde{a}_{γ_i} following from the TasR approach is,

$$\mathbf{w}_{f1} \gg \mathbf{T}_{\gamma 3} > \mathbf{T}_{\gamma 2} > \mathbf{w}_{f2} > \mathbf{T}_{\gamma 1} \quad (40)$$

where the multiplier corresponding to wrench \mathbf{w}_{f3} cannot be evaluated. Apart from the unevaluated degrees of freedom both approaches show the same order of compliance. The order based on both the RasT and the TasR approach can be interpreted as,

$$\mathbf{w}_{f1} \gg \mathbf{T}_{\gamma 3} > \mathbf{T}_{\gamma 2} > \mathbf{w}_{f2} > \mathbf{T}_{\gamma 1} > \mathbf{w}_{f3} \quad (41)$$

Single corrugated compliant shell

The first shell mechanism was introduced in Section , a moderately single corrugated shell mechanism. The mechanism is fully constrained at the bottom and the point of interest is in the centre of the opposing side, indicated by a black dot. Figure 9 shows the unified compliance visualisation applied to the single corrugated compliant shell mechanism.

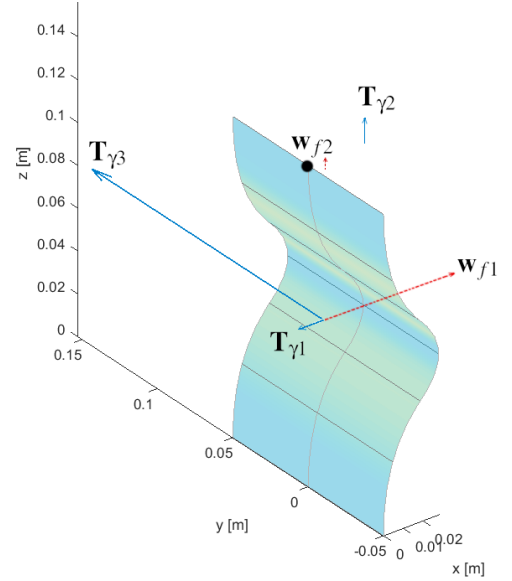


FIGURE 9: UNIFIED COMPLIANCE VECTORS CROSS PIVOT

It shows the largest compliance vector corresponding to twist $\mathbf{T}_{\gamma 3}$, which means that the largest compliance direction is a screw around the direction of twist $\mathbf{T}_{\gamma 3}$. The second largest compliance vector corresponds to wrench \mathbf{w}_{f1} which is a pure translation parallel to the direction of wrench \mathbf{w}_{f1} . The other unified compliance magnitudes are relatively small, intuitively explainable by the larger moment of inertia of the corresponding cross section. The total initial relative degree order based on the unified compliance multipliers \tilde{a}_f following from the RasT approach is given as,

$$\mathbf{T}_{\gamma 3} > \mathbf{w}_{f1} > \mathbf{T}_{\gamma 2} > \mathbf{T}_{\gamma 1} > \mathbf{w}_{f2} > \mathbf{w}_{f3} \quad (42)$$

Extruded spiral compliant shell

The second mechanism is an extruded spiral compliant shell mechanism. The material properties are identical to the single corrugated shell mechanism. The 2mm thick geometry is defined by NURBS [12], a third polynomial follows a 3×5 grid.

Five coordinates are placed on three planes in $y = -0.05$, $y = 0$ and $y = 0.05$. The x and z coordinates are defined in Table 8.

TABLE 8: NURB COORDINATES EXTRUDED SPIRAL SHELL

Point	1	2	3	4	5
x	0.00	-0.03	0.00	0.03	0.00
z	0.00	0.04	0.08	0.06	0.04

The mechanism is fully constrained at the bottom and the point of interest is in the centre of the opposing side, indicated by a black dot. The initial configuration is shown in Figure 10.

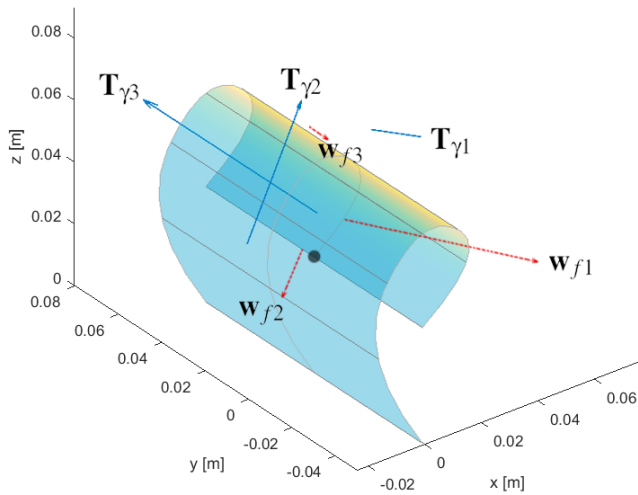


FIGURE 10: UNIFIED COMPLIANCE VECTORS OF THE SPIRAL SHELL MECHANISM

The total initial degree of freedom order based on the unified compliance multipliers \bar{a}_f following from the RasT approach is,

$$\mathbf{T}_{\gamma 3} > \mathbf{w}_{f1} > \mathbf{T}_{\gamma 2} > \mathbf{T}_{\gamma 1} > \mathbf{w}_{f2} > \mathbf{w}_{f3} \quad (43)$$

Although the mechanism is still a developable surface, predicting the locations and magnitudes of the compliance vectors is already more challenging compared to the previous shell mechanism.

DISCUSSION

The characterization presented in this paper has benefits compared to existing methods. Most characterizations do not address the coupling between rotations and translations [4] and are only able to separately compare rotational degrees of freedom and translational degrees of freedom, within one mechanism [6]. To compare rotational and translational compliances with each other it is necessary to introduce a unification variable. Where existing methods introduce arbitrarily chosen unification variables [9], this paper introduces two consistently derived physically meaningful unification lengths which include coupling, thus allowing the fair comparison of rotational and translational compliances within and between mechanisms.

We derived two unification lengths based on two approaches. The unification length resulting from the RasT approach, based on Plücker coordinates, is derived independently and yielded similar results as Lin's [8] research, based on hybrid coordinates, used to optimize graspers. Lin does not recognize the limitations of the results that became apparent when used to characterize compliant shell elements. We eliminate these limitations by introducing both the RasT and the TasR approach. Both Lin's derivation and the introduced potential energy method are more straightforward than the introduced virtual load method, however they give less insight into the actual kinematics. The virtual load method includes sub-steps with physical relevance, these sub-steps themselves can form the basis for designs. Thorough knowledge of the composition of these sub-steps provides the opportunity to vary parameters in an intelligent manner to reach specific objectives. Additionally, energy, in any form, is a scalar quantity. By introducing the principle of potential energy all valuable directional information is lost.

CONCLUSION

This paper introduces a method for the characterization of complex compliant mechanisms that considers coupling and allows the comparison of stiffness between all six degrees of freedom. The characterization is based on consistently derived non-arbitrary unification variables based on equivalent compliance by virtual load and potential energy, therefore allows the comparison of compliance between degrees of freedom of different mechanisms. With this introduced comprehensive comparison the opportunity rises to order all degrees of freedom, within and between mechanisms in terms of compliance. Although this paper is focussed on compliant shell elements, the characterization presented can be done for any mechanism which has a symmetric positive definite non-singular compliance matrix. This includes both compliant flexure and shell mechanisms.

ACKNOWLEDGMENT

The writers would like to acknowledge NSF No. IIS - 1527133 as well as STW (HTSM-2012 12814: ShellMech) for the financial support of this project.

REFERENCES

- [1] Seffen, K. A., 2012. “Compliant shell mechanisms”. *Phil. Trans. R. Soc. A*, **370**(1965), pp. 2010–2026.
- [2] Pellegrino, S., 2005. “Bistable shell structures”. In Proc. 46th AIAA/ASME/ASCE/AHS/ASC Structures, Structural Dynamics and Materials Conf., Austin, TX, 18â 21 April 2005.
- [3] Radaelli, G., and Herder, J. L., 2014. “Isogeometric shape optimization for compliant mechanisms with prescribed load paths”. *Proceedings ASME IDETC/CIE*.
- [4] Kim, C. J., 2005. “A conceptual approach to the computational synthesis of compliant mechanisms.”. PhD thesis.
- [5] J.P.A. Nijssen, G. Radaelli, C. K., and Herder, J., 2016. “Design and analysis of a shell mechanism based two-fold force controlled scoliosis brace”.
- [6] J.P.A. Nijssen, G. Radaelli, C. K., and Herder, J., 2016. “Overview and kinematic characterization of compliant shell mechanism building blocks”.
- [7] Lipkin, H., and Patterson, T., 1992. “Geometric properties of modelled robot elasticity: Part idecomposition”. In Proceedings of ASME Design Technical Conferences, pp. 187–193.
- [8] Lin, Q., Burdick, J. W., and Rimon, E., 2000. “A stiffness-based quality measure for compliant grasps and fixtures”. *IEEE Transactions on Robotics and Automation*, **16**(6), pp. 675–688.
- [9] Teichmann, M., 1996. “A grasp metric invariant under rigid motions”. In Robotics and Automation, 1996. Proceedings., 1996 IEEE International Conference on, Vol. 3, IEEE, pp. 2143–2148.
- [10] Chasles, M., 1830. “Note sur les propriétés générales du système de deux corps semblables entr’eux et placés d’une manière quelconque dans l’espace; et sur le déplacement fini ou infiniment petit d’un corps solide libre”. *Bulletin des Sciences Mathématiques, Férussac*, **14**, pp. 321–26.
- [11] Murray, R. M., Li, Z., and Sastry, S. S., 1994. *A mathematical introduction to robotic manipulation*. CRC press.
- [12] Piegl, L., and Tiller, W., 2012. *The NURBS book*. Springer Science & Business Media.
- [13] Jonker, J., and Meijaard, J., 1990. “Spacarc computer program for dynamic analysis of flexible spatial mechanisms and manipulators”. *Multibody systems handbook*, **8**, pp. 123–143.

B

Non-linear characterization library of promising building blocks

This appendix provides the fully characterized building blocks.

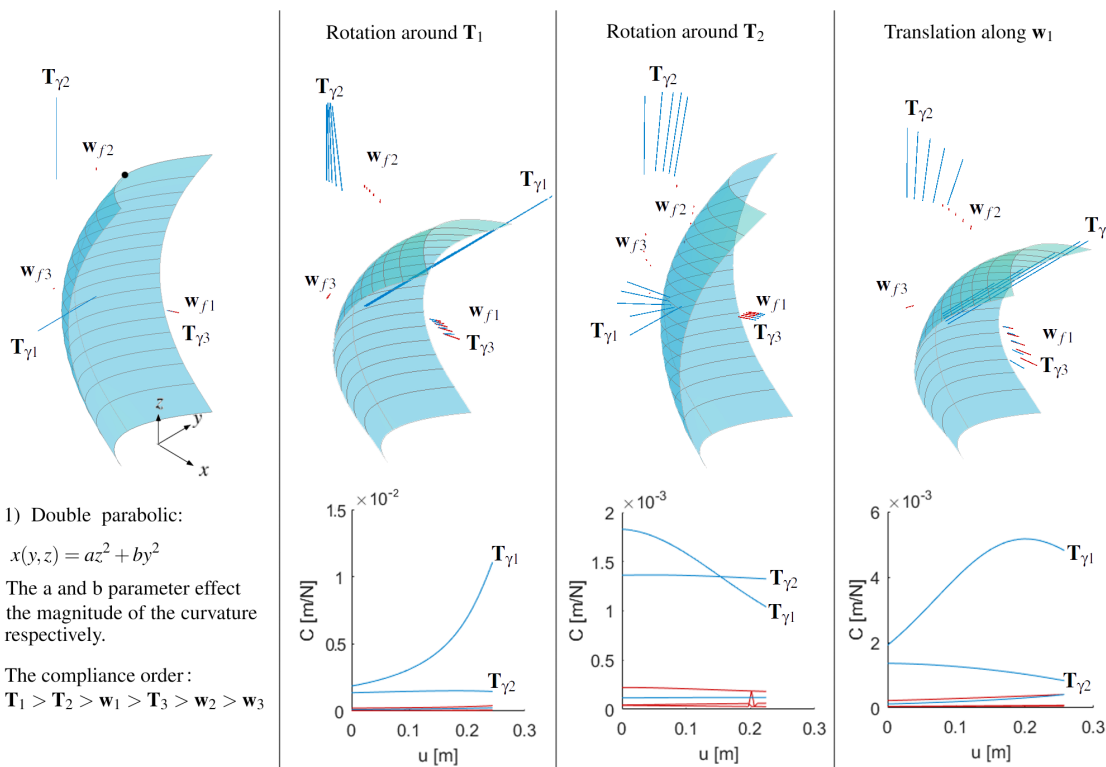


Figure B.1: Characterised Double parabolic building block

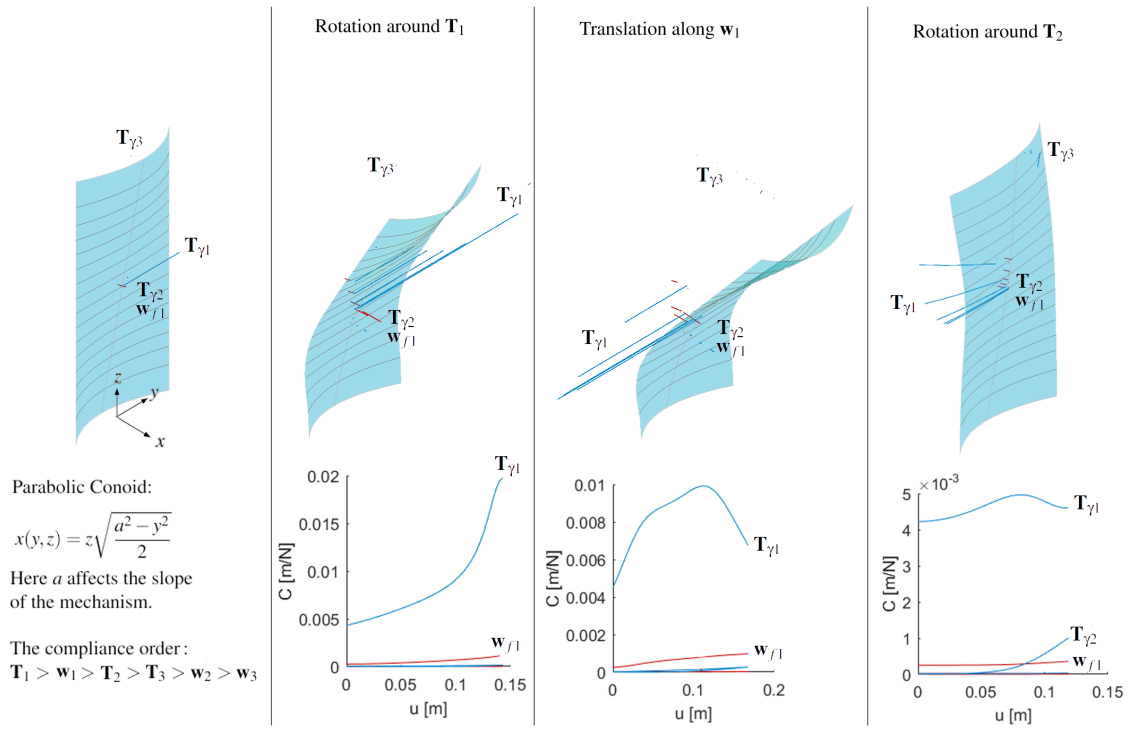


Figure B.2: Characterized Parabolic Canoid building block

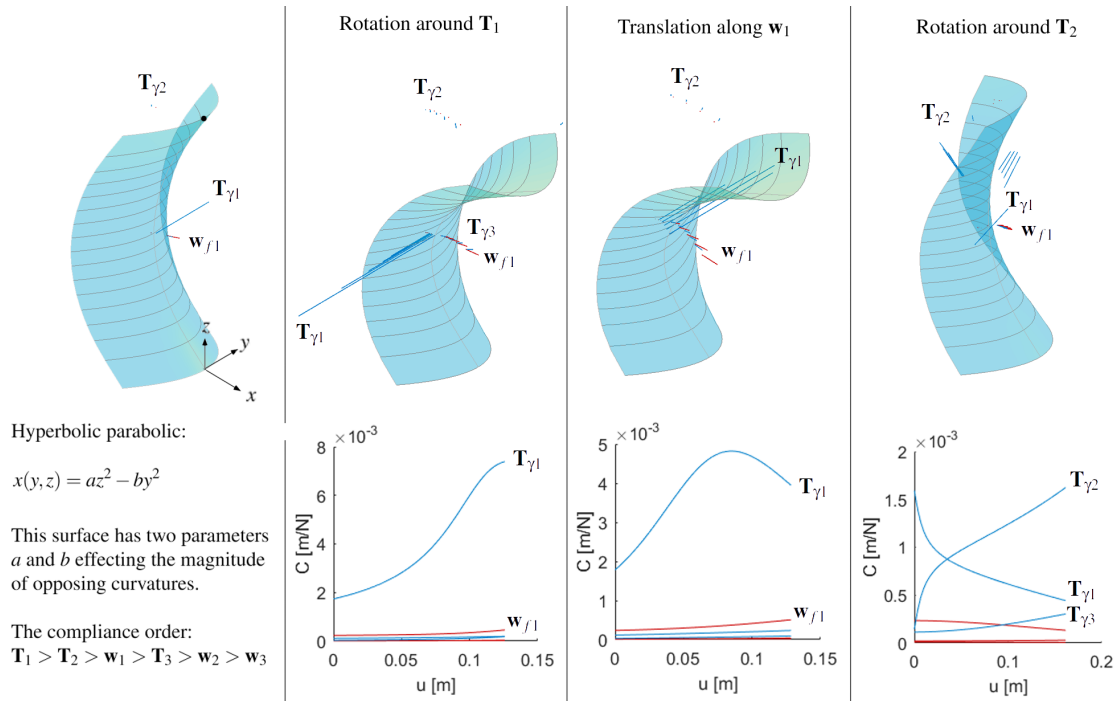


Figure B.3: Characterized Hyperbolic parabolic building block

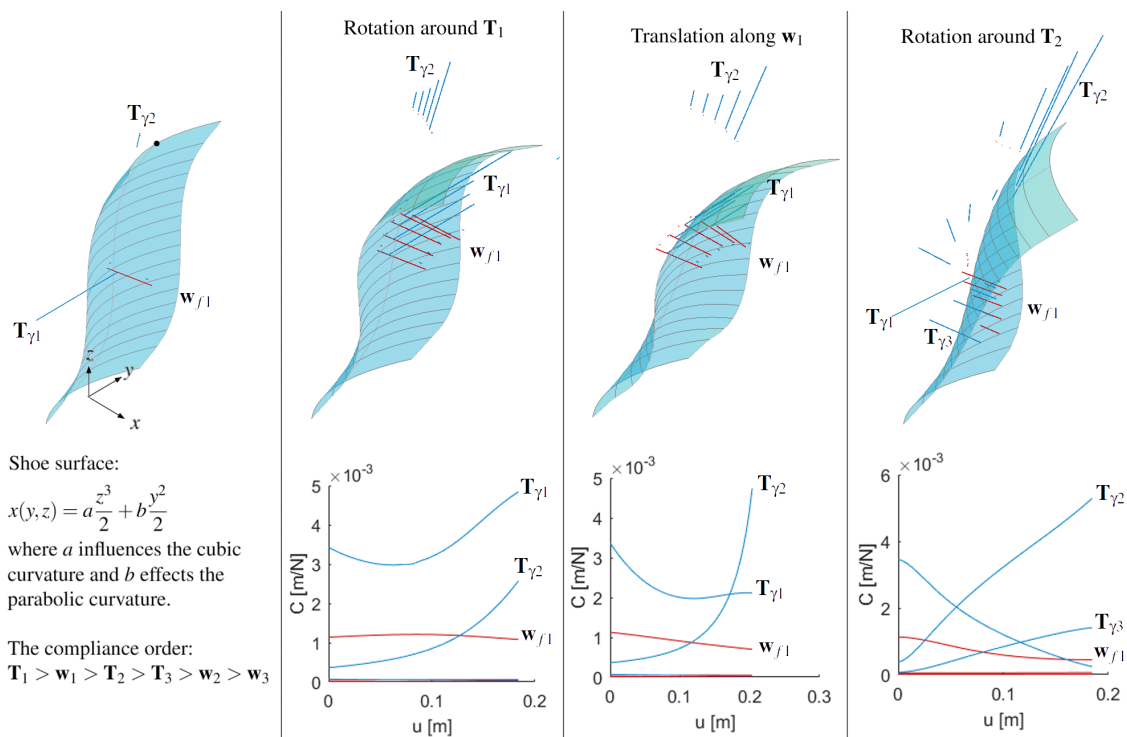


Figure B.4: Characterized Shoe surface building block

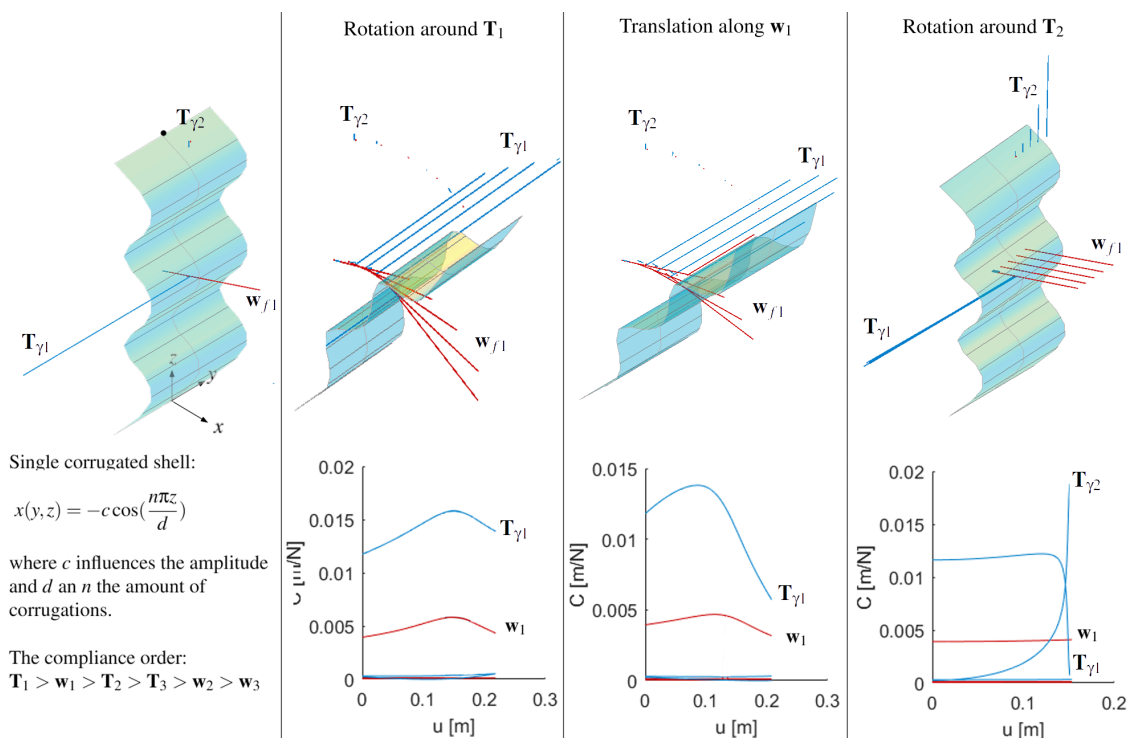


Figure B.5: Characterized Single Corrugated building block

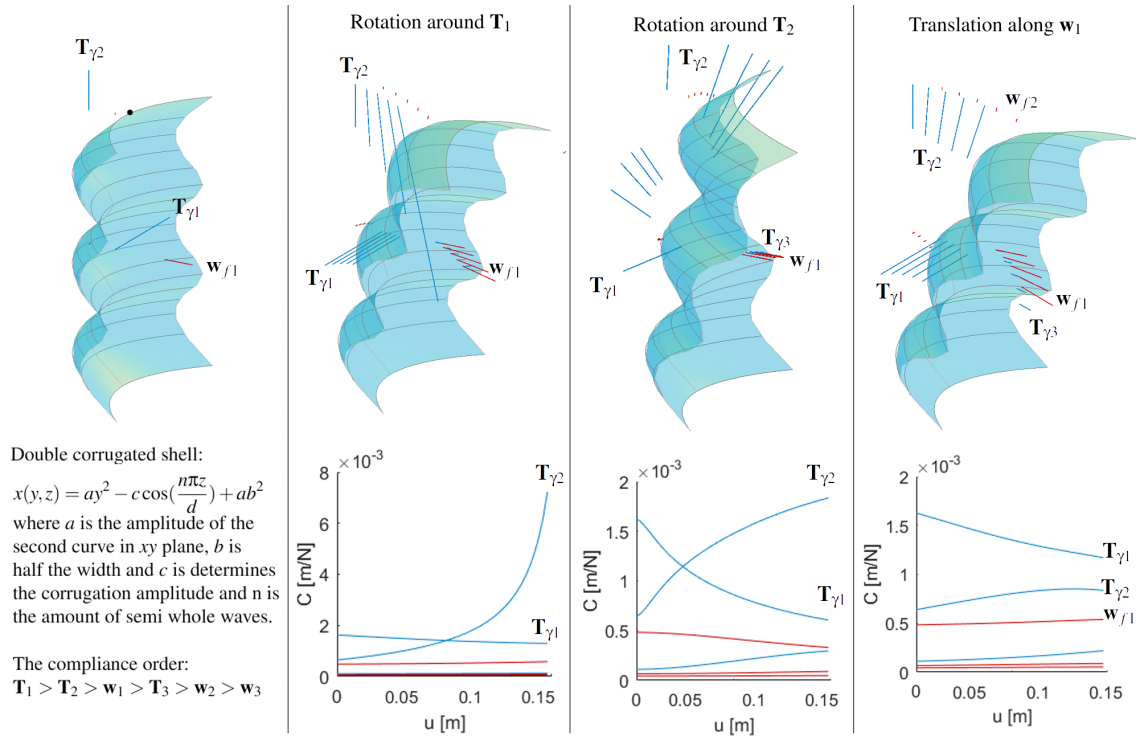


Figure B.6: Characterized Double Corrugated building block

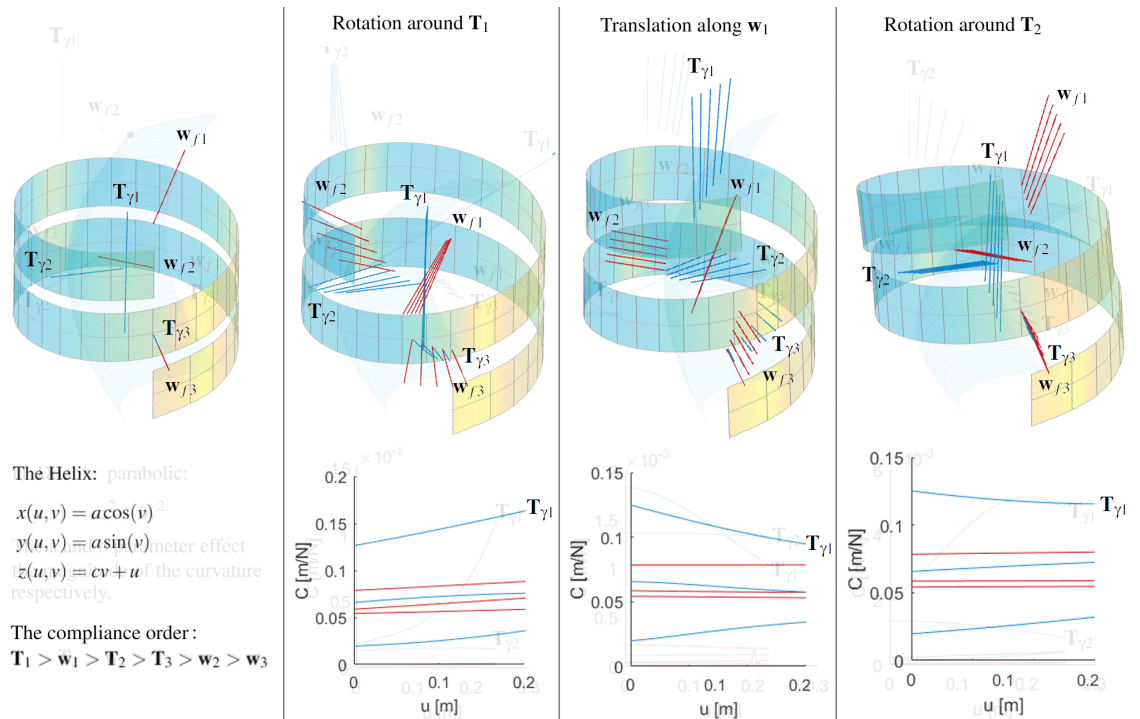


Figure B.7: Characterized Helix building block

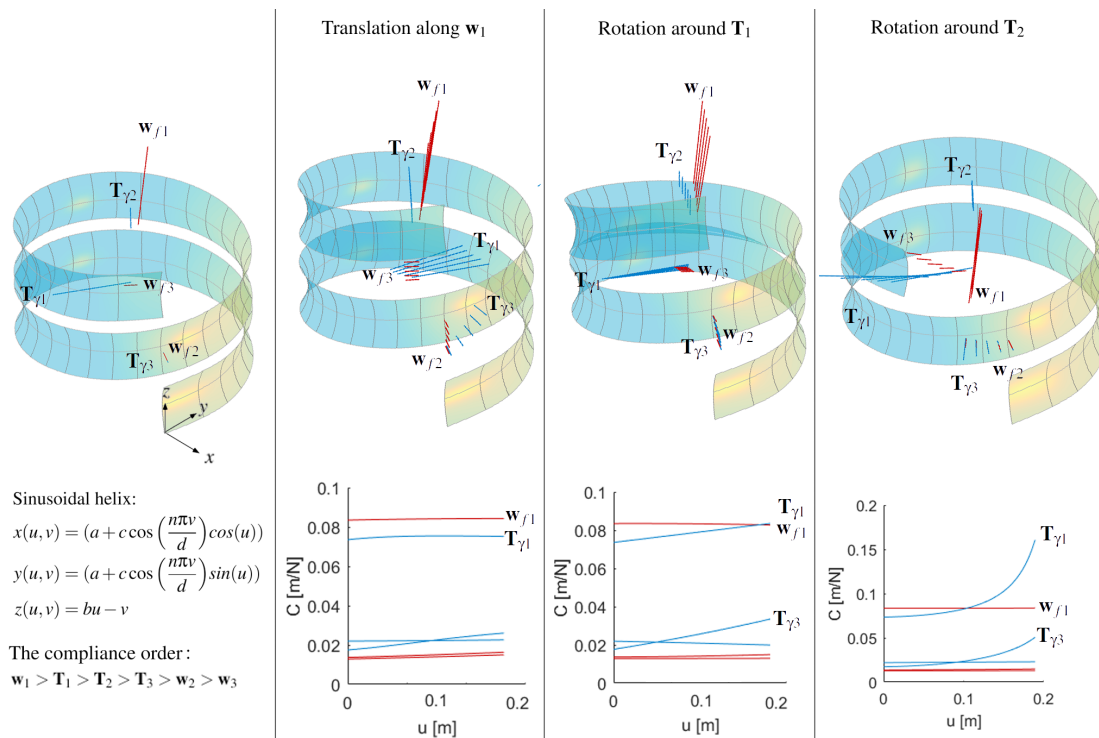


Figure B.8: Characterized Sinusoidal Helix building block

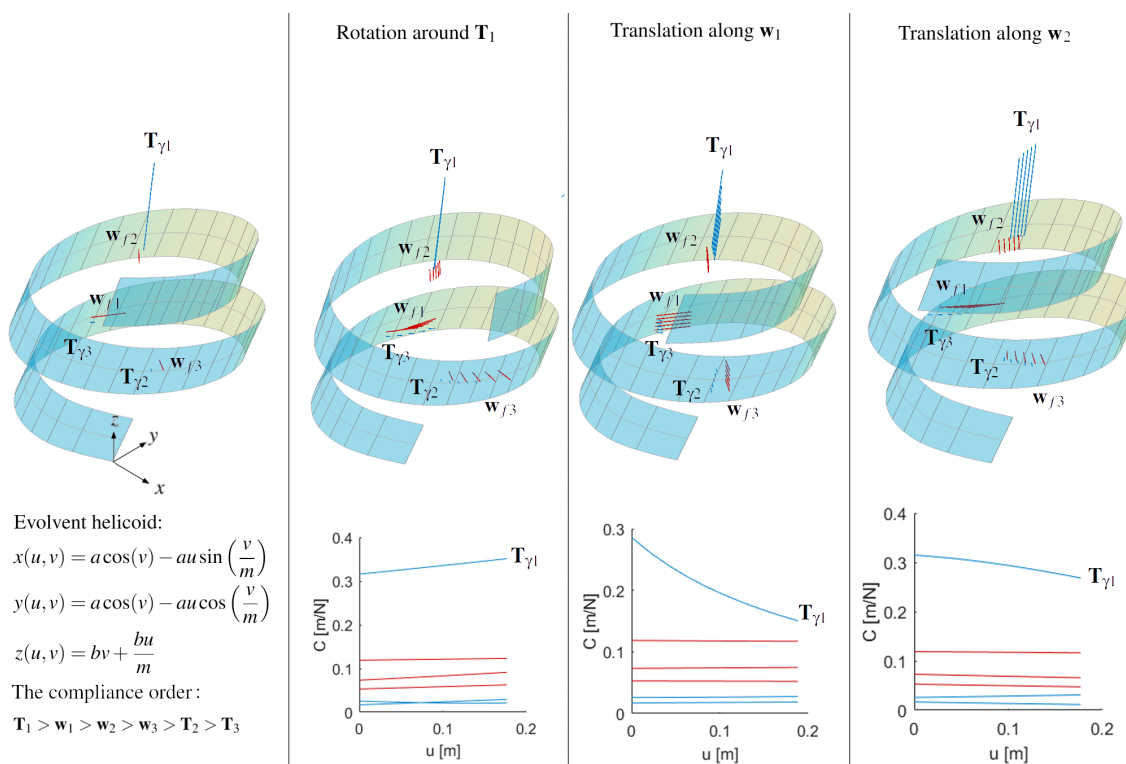


Figure B.9: Characterized Evolvent Helicoid building block

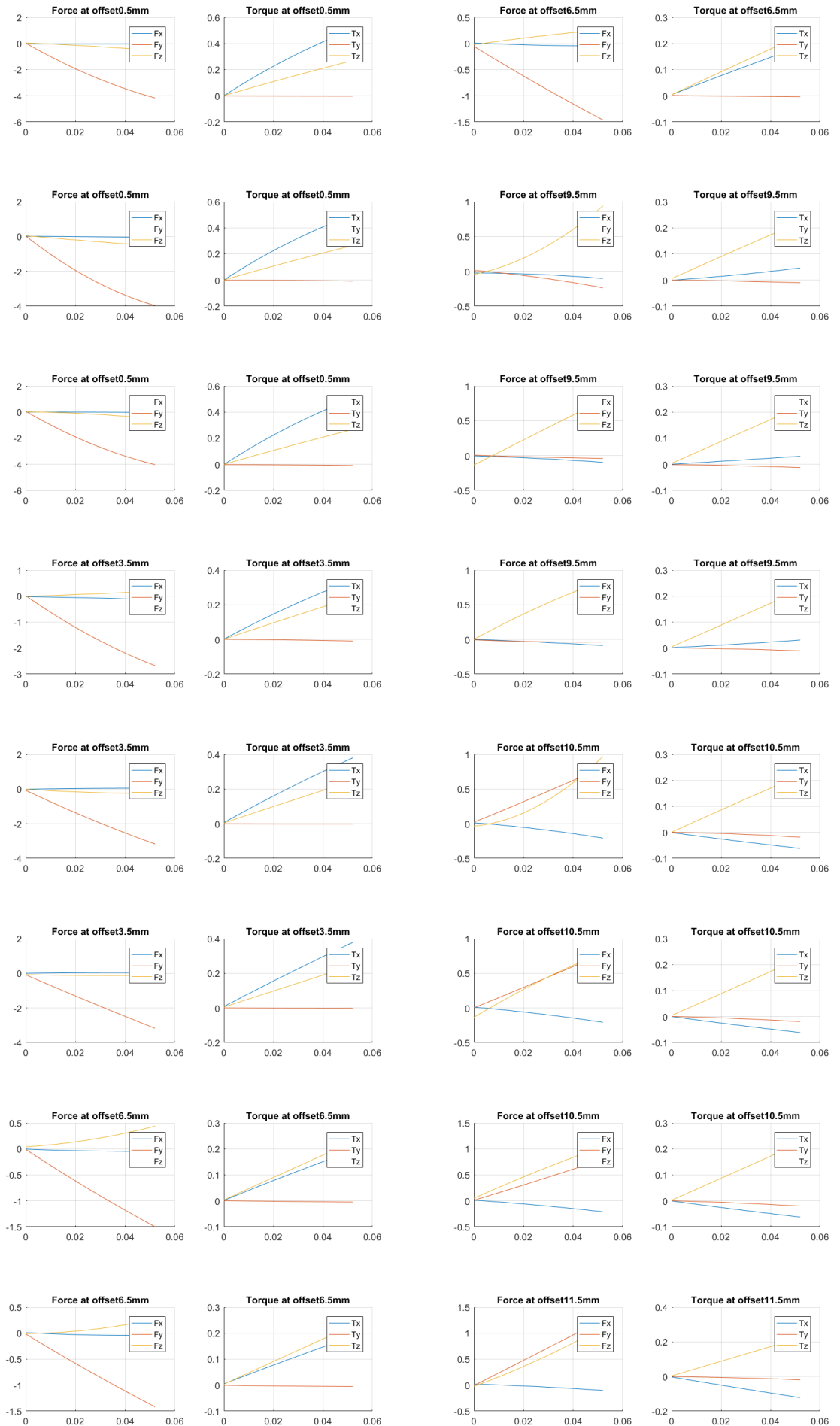
C

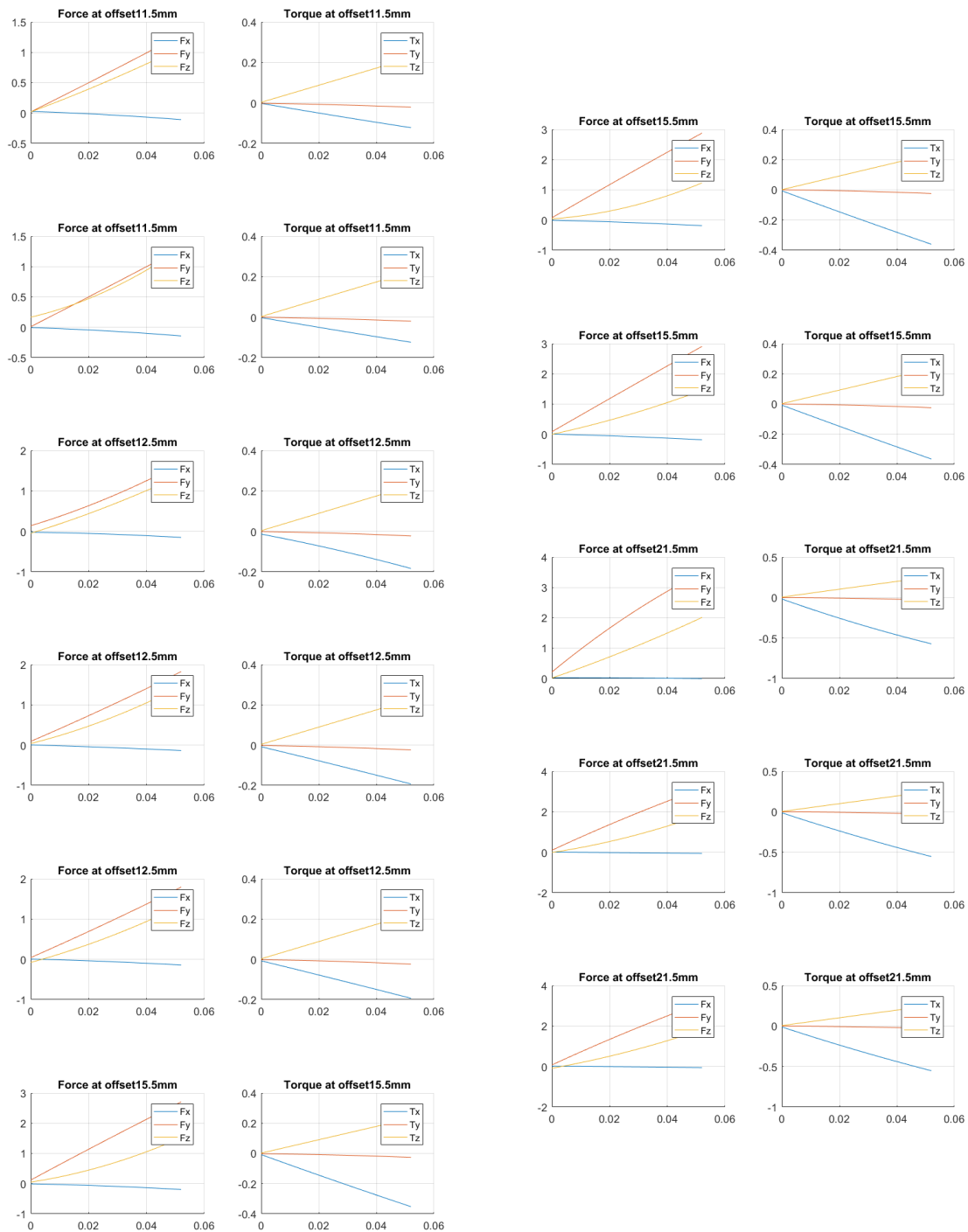
Experiment Data

This chapter provides additional information on the measurement set-up. Including the measurement set-up and raw data.



Figure C.1: Full Measurement Set-up





Background Theory

D.1. Structural analysis

The difficulty of designing compliant mechanisms are the intertwined kinematics and kinetics. Furthermore, the freedom and constraint directions change while subjected to large deformations. This chapter provides basic background theory relevant to describe kinematics and kinetics of compliant shell mechanisms. The background theory starts with a structural analysis of plates, a brief introduction of potential energy in plate theory and the derivation of tangent and secant matrix are discussed.

This section start by describing linear equations and then extending them to continuous and discrete non-linear equations and plate theory.

The linear relation between loads \mathbf{f} and displacement \mathbf{u} of a mechanism can be described as,

$$\mathbf{f} = K\mathbf{u} \quad (\text{D.1})$$

where K is the constant stiffness matrix, when the determinant of the stiffness matrix is not equal to zero the stiffness matrix is invertible. The inverse of the stiffness matrix K is the compliance matrix C , therefore the linear relation can also be described as,

$$\mathbf{u} = C\mathbf{f} \quad (\text{D.2})$$

These linear relations cannot be applied when the system exhibits non-linear behaviour, this includes phenomena such as buckling, plasticity and large deformations. These phenomena can be divided into two categories, geometric and physical non-linearity. Since compliant shell mechanisms are often subjected to large deformations while plastic deformation is avoided, this document focuses on the effects of geometric non-linearity, while assuming linear-physical behaviour. Van Keulen [18] describes the general relation between loads and displacements. The relation between loads and displacements can be divided into three sub-relations based on three principles:

1. Continuity: Displacements \leftrightarrow Deformations
2. Constitutive Equations: Deformations \leftrightarrow Stresses
3. Equilibrium: Stresses \leftrightarrow External Loads

Deformation can be described by both the Lagrangian and the Eulerian description. If the undeformed configuration is starting point of the approach the Lagrangian description is used, which describes the relation between an original $d\mathbf{r}$ and deformed $\hat{d}\mathbf{r}$ line element on a body, defined as

$$2d\mathbf{r} \cdot E d\mathbf{r} = \hat{d}\mathbf{r}^2 - d\mathbf{r}^2 \quad (\text{D.3})$$

where E is the Green-Lagrange strain tensor. The relation between the original and the deformed material line element can also be written as,

$$\hat{d}\mathbf{r} = \mathbf{F}d\mathbf{r} \quad (\text{D.4})$$

where \mathbf{F} is the geometric dependent deformation gradient, which can be decomposed in a deformation \mathbf{U} and a rotation \mathbf{R} matrix. The Green-Lagrange strain tensor for finite elements, respectively in normal and multi-index notation, becomes

$$\mathbf{E}_{ij} = \frac{1}{2} \left(\frac{\delta u_i}{\delta x_j} + \frac{\delta u_j}{\delta x_i} + \sum_k \frac{\delta u_k}{\delta x_i} \frac{\delta u_k}{\delta x_j} \right) = \frac{1}{2} (u_{i,j} + u_{j,i} + \sum_k u_{k,i} u_{k,j}) \quad (\text{D.5})$$

A system is in a static equilibrium if the following equation holds for all virtual displacements δu ,

$$\delta W_i = \delta W_u \quad (\text{D.6})$$

where δW_i is the internal virtual work and δW_u the external virtual work.

Continuous non-linear mechanics

Further on a repeated index automatically means a summation. In continuum mechanics the internal work is described by the integration over the undeformed body V_0 defined as,

$$\delta W_i = \int_{V_0} \mathbf{S} : \delta \mathbf{E} dV_0 \quad (\text{D.7})$$

where \mathbf{E} is the Green-Lagrange strain tensor and \mathbf{S} is the symmetric 2nd Piola-Kirchhoff stress tensor. The external work is described by the integration over the outer surface A_0 and is given by,

$$\delta W_u = \int_{A_0} \delta \mathbf{u} \cdot \mathbf{q} dA_0 + \int_{V_0} \delta \mathbf{u} \cdot (\rho_0 \mathbf{f}) dV_0 \quad (\text{D.8})$$

where δu is a infinitesimal displacement, \mathbf{q} the force and \mathbf{f} is the body load. By substituting the Green-Lagrange deformation tensor of equation D.5 into equation D.12 and by applying the divergence theorem, the internal work can be reorganized as,

$$\delta W_i = \int_{A_0} \delta \mathbf{u} \cdot (\mathbf{F} \mathbf{S} \mathbf{n}_0) dA_0 - \int_{V_0} \delta \mathbf{u} \cdot (\text{Div} \mathbf{F} \mathbf{S}) dV_0 \quad (\text{D.9})$$

where \mathbf{n}_0 is the outward normal vector in the undeformed configuration. Both the internal and the external work must be equal in order to have static equilibrium, consequently the following equations must hold for every point in a body,

$$\text{Div}(\mathbf{F} \mathbf{S} + \rho_0 \mathbf{f}) = 0 \quad (\text{D.10})$$

as well as the boundary condition,

$$\mathbf{F} \mathbf{S} \mathbf{n}_0 = q. \quad (\text{D.11})$$

Discrete non-linear mechanics

The internal en external work can also be described for discrete systems, which can be used for finite element modelling, where complex structures can be combined by simple elements. Each element will have a generalized deformation, for the arbitrary chosen element k this is $\xi^{(k)}$, depending on the number of nodal degrees of freedom $\mathbf{d}^{(k)}$. The internal work for a discrete system on element level is described by,

$$\delta W_i = \sum \zeta^{(k)} \cdot \delta \xi^{(k)} \quad (\text{D.12})$$

where $\zeta^{(k)}$ are the generalized stresses and $\delta \xi^{(k)}$ the generalized deformations. The deformation depends on the degrees of freedom in a non-linear manner, however this relation can be linearised. The tangent of the non-linear function is given as,

$$\delta \xi^{(k)} = D^k [d^k] \delta \mathbf{d}^k \quad (\text{D.13})$$

where D^k is the configuration dependent differentiation matrix, which results from differentiating the deformations with respect to the degrees of freedom; therefore,

$$D_{ij}^k = \frac{\partial}{\partial d_j^k} \xi_i^k \quad (\text{D.14})$$

Hookes law assumes a linear relation between the deformations and stresses given by,

$$\zeta^k = \mathbf{S} \xi^k \quad (\text{D.15})$$

Where \mathbf{S} is a constant matrix which depends on the material, size and type of the element. The internal virtual work of an element is describes as,

$$\delta W_i = \sum \zeta^K \cdot D^k [d^k] \delta d^k. \quad (\text{D.16})$$

Substitution of the generalized stresses on system level results in the following equations respectively for the internal and external energy,

$$\delta W_i = \mathbf{S} \xi \cdot D[d] \delta d \quad (\text{D.17})$$

and

$$\delta W_u = f \cdot \delta d. \quad (\text{D.18})$$

Thus in equilibrium the nodal loads are equal to the transposed of the differentiation matrix times the generalized stresses.

$$f = D^T \xi S \quad (D.19)$$

In conclusion, an element has deformations $[D^k]$ which can be specified in a non-linear manner as a function of the degrees of freedom $[d^k]$. By applying hookes law on the specified deformation the corresponding stresses $[\zeta^k]$ can be calculated. Using these values the virtual internal $[\delta W_i]$ and external $[\delta W_u]$ work can be described, resulting in the equilibrium equation. Where the transposed of the differentiation of the deformations with respect to the degrees of freedom times the stresses is equal to the nodal loads $[f^k]$ in equilibrium. At system level all these elements are summed.

Kirchoff-Love Plate theory

Van Keulen [18] describes shell and plate theory. In order to design plate and shell type constructions numerical tools are necessary in order to describe linear and non-linear phenomena, such as deflection, strain, buckling and vibrations. Developed tools are the boundary element method, finite difference method and the finite element method. [explain boundary element method, finite difference method] Using finite shell elements there are two approaches. First, the degenerate approach, where 3D solid problem can be reduced to a 2D shell problem. Second, the approach directly based on shell theory. Due to the complexity of shell theory simplifications and assumptions are often made, however this can induce problems such as incorrect rigid body motion responses and excessively stiff responses. Kirchoff-Love plate theory applies for thin plates and the Mindlin-Reissner plate theory for thick plates, as earlier defined this document will focus on classical thin plate theory. Kirchoff-Love theory is an extension to plates of the Euler-Bernoulli beam theory. Van Keulen [18] describes the Kirchoff-Love theory, Love developed the theory using the following assumptions imposed by Kirchoff regarding the straight line perpendicular to the mid-surface, also called transverse normals [13].

1. Transverse normals remain straight before and after deformation
2. Transverse normals are inextensible
3. Transverse normals remain perpendicular to the mid-surface after deformation.

In order to describe the theory Cartesian Coordinates (e_x, e_y, e_z) are used, the xy plane coincides with the mid-plane of the plate and the z axis with the thickness perpendicular from the mid-plane. The displacements along the Cartesian coordinates are given by (u, v, w) , as can be seen in Figure D.1

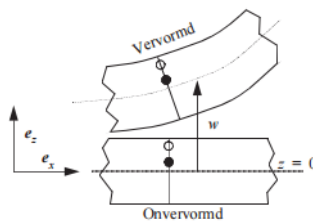


Figure D.1: Undeformed and deformed geometries of a plate, using Kirchoff assumptions, reproduced from [13]

With a constant thickness the upper surface is at $z = 1/2h$ and the lower surface $z = -1/2h$. The displacement vector, for small displacements can be written as,

$$u_x = -z\phi_x(x; y), \quad (D.20)$$

$$u_y = -z\phi_y(x; y), \quad (D.21)$$

$$u_z = w(x; y), \quad (D.22)$$

where

$$\phi_x = \frac{\delta w}{\delta x} = w_x, \quad (D.23)$$

$$\phi_y = \frac{\delta w}{\delta y} = w_y, \quad (\text{D.24})$$

The displacement is thus independent of the transverse coordinate z and only dependant on the displacement of the mid-surface w , since w only depends on the coordinates x en y the the 3D problem is reduced to a 2D problem. Substitution of the displacement vectors D.20 into the Green Lagrange strain tensor D.5 results in,

$$\epsilon_{xx} = -z\phi_{x,x}, \quad (\text{D.25})$$

$$\epsilon_{yy} = -z\phi_{y,y}, \quad (\text{D.26})$$

$$\epsilon_z = 0, \quad (\text{D.27})$$

$$\epsilon_{xy} = \epsilon_{yx} = -z\frac{1}{2}z(\phi_{x,y} + \phi_{y,x}) \quad (\text{D.28})$$

$$\epsilon_{yz} = \epsilon_{zy} = z\frac{1}{2}z(w_{,y} + \phi_y) = 0 \quad (\text{D.29})$$

$$\epsilon_{xz} = \epsilon_{zx} = z\frac{1}{2}z(w_{,x} + \phi_x) = 0 \quad (\text{D.30})$$

Three parameters are introduced $\kappa_{xx}, \kappa_{yy}, \kappa_{xy}$, the change in curve in the mid-plane, defined as

$$\kappa_{xx} = -\phi_{x,x} = -w_{x,x} \quad (\text{D.31})$$

$$\kappa_{yy} = -\phi_{y,y} = -w_{y,y} \quad (\text{D.32})$$

$$\kappa_{xy} = -(\phi_{x,y} + \phi_{y,x}) = -(w_{,yx} + w_{,xy}) = -2w_{,xy} \quad (\text{D.33})$$

and he physical representation of the principal curvatures are shown in Figure D.2

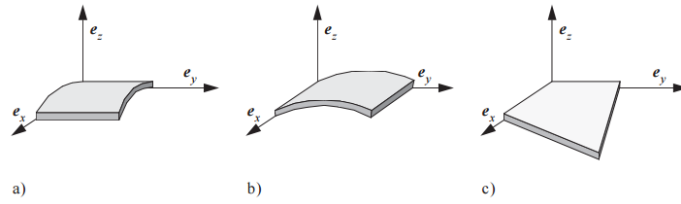


Figure D.2: Principal curvatures

By substituting the new parameters into the resulting strain equation D.25 and using the kirchoff assumption of zero strain in the transverse normals it results in,

$$\epsilon_{xx} = z\kappa_{xx} \quad (\text{D.34})$$

$$\epsilon_{yy} = z\kappa_{yy} \quad (\text{D.35})$$

$$\epsilon_{xy} = \frac{1}{2}z\kappa_{xy} \quad (\text{D.36})$$

$$\epsilon_{zz} = 0 \quad (\text{D.37})$$

$$(\text{D.38})$$

The surface of a plate is denoted by an A and the boundary, assumed line, by an S . Using the internal work equation D.12 and the equations D.25 D.34 the result is,

$$\delta W_i = \int_A (M_{xx}\delta\kappa_{xx} + M_{yy}\delta\kappa_{yy} + M_{xy}\delta\kappa_{xy})dA, \quad (\text{D.39})$$

where the ,

$$M_{xx} = \int_{-\frac{1}{2}h}^{+\frac{1}{2}h} z\omega_{xx}dz \quad (\text{D.40})$$

$$M_{yy} = \int_{-\frac{1}{2}h}^{+\frac{1}{2}h} z\omega_{yy}dz \quad (\text{D.41})$$

$$M_{xy} = \int_{-\frac{1}{2}h}^{+\frac{1}{2}h} z\tau_{xy}dz \quad (\text{D.42})$$

The external work based on D.8 is expressed as,

$$\delta W_u = \int_A (P^+ + P^-) \delta w dA + \int_S \int_{-\frac{1}{2}h}^{+\frac{1}{2}h} (q_x(-z\delta\phi_x) + q_y(-z\delta\phi_y) + q_z(-z\delta w)) dz ds \quad (D.43)$$

where p^+ is the distributed load on the upper surface and p^- the distributed load on the lower surface. A system is in a static equilibrium if the internal virtual work is equal to the external virtual work for all virtual displacements δu , as stated in equation D.6.

D.2. Potential Energy

Van Keulen [18] describes the principal of potential energy in plate bending with conservative systems and loads. The total potential energy ϕ is given by the summation of the elastic potential ξ and the external load potential β and depends on the displacement field u^o thus,

$$\phi[u^o] = \xi[u^o] + \beta[u^o] \quad (D.44)$$

The elastic potential is described by classical laminate theory, expressed as

$$\xi[u^o] = \int \frac{1}{2} \epsilon^T [u^o] \mathbf{S} \epsilon [u^o] dV \quad (D.45)$$

where ϵ is a displacement vector composed of the translations and rotations, V is the total volume and S is 6x6 matrix with material properties.

$$\xi[u^o] = \frac{1}{2} \int_V [\gamma \quad \kappa] \mathbf{S} \begin{bmatrix} \gamma \\ \kappa \end{bmatrix} dV \quad (D.46)$$

where γ represents in plane strain, κ the curvature change. When we ignore the coupling matrices [explain why this could be done] S_B to reduce the complexity the total elastic potential is given by,

$$\phi = \int \int \left\{ \frac{1}{2} \kappa^T \mathbf{S}_D \kappa + \frac{1}{2} \gamma^T \mathbf{S}_A \gamma + \mathbf{M}^T \kappa + \mathbf{N}^T \gamma \right\} dA \quad (D.47)$$

where \mathbf{M} is and \mathbf{N} [extend]

The term equation is build from respectively the bending strain energy, the membrane, strain, the bending moment and the external load.

Tangent stiffness Matrix

The stiffness matrix is able to describe the relation between the load vector and the displacement vector. If it is assumed that the external load vector is not configuration dependent it can be written as function of a scalar, defined as

$$\mathbf{f}^{ext}[\lambda] = \lambda \mathbf{P} \quad (D.48)$$

Where \mathbf{f}^{ext} is the applied external load vector, \mathbf{P} is a load parameter and λ is the load intensity. In order to analyse the system the load intensity can be increased with increments from the unloaded situation, which gives a step by step linear approximation of the resulting deformations, also known as an incremental analysis. For every step the tangent stiffness matrix must be found. The equilibrium equation differentiated to the load intensity gives

$$K_t[d] \frac{d\mathbf{d}}{d\lambda} = \frac{d\mathbf{f}}{d\lambda} \quad (D.49)$$

Where $K_t[d]$ is the symmetric positive definite tangent stiffness matrix, a one-dimensional representation of an incremental analysis using the tangent operator is visualised in Figure D.3

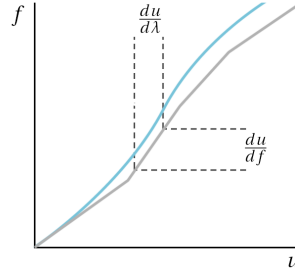


Figure D.3: Incremental analysis

The differentiation D.49 of equilibrium D.19 defines $K_t[d]$, which gives the local stiffness of the system and is composed by two parts

$$\mathbf{K}_t = \mathbf{D}^T \mathbf{S} \mathbf{D} + \mathbf{G} \quad (\text{D.50})$$

The first part is the physical stiffness matrix and the second part the geometrical stiffness matrix. Where \mathbf{G} on element level in multi-index notation is given by

$$G_{ij}^k = \sum_r \zeta_r^k \zeta_{r,ij}^k \quad (\text{D.51})$$

For a one-dimensional representation the tangent stiffness can be defined as

$$K_t \Delta \mathbf{u} = \Delta \mathbf{f} \quad (\text{D.52})$$

Where $\Delta \mathbf{u}$ is an incremental displacement step

D.3. Twist and wrench location vector and pitch

A twist \mathbf{T} contains a translational rotational part, utilizing this the location vector and pitch can be calculated. According to Chasles theorem the twist is defined as,

$$\mathbf{T} = \begin{bmatrix} \vec{\delta}_i \\ \vec{\gamma}_i \end{bmatrix} = \begin{bmatrix} (\vec{r}_i \times \vec{\gamma}_i) + h_i \vec{\gamma}_i \\ \vec{\gamma}_i \end{bmatrix}, \quad i = 1, 2, 3 \quad (\text{D.53})$$

The twist pitch is defined as the ratio between translation and rotation, given a twist defined as,

$$h_i = \frac{\vec{\gamma}_i \vec{\delta}_i}{\vec{\delta}_i \vec{\delta}_i} \quad (\text{D.54})$$

Since the twist location vector and the rotational direction are orthogonal, the twist location vector can be determined as,

$$\vec{r}_i = \frac{\vec{\gamma}_i \times (\vec{\delta}_i - h_i \vec{\gamma}_i)}{\vec{\gamma}_i \vec{\gamma}_i} \quad (\text{D.55})$$

A wrench \mathbf{w} contains a moment and force part, utilizing this the wrench's location vector and pitch can be calculated. According to Poisson theorem the wrench is defined as,

$$\mathbf{w} = \begin{bmatrix} \vec{f}_i \\ \vec{\tau}_i \end{bmatrix} = \begin{bmatrix} \vec{f}_i \\ (\vec{b}_i \times \vec{f}_i) + d_i \vec{f}_i \end{bmatrix}, \quad i = 1, 2, 3 \quad (\text{D.56})$$

The wrench pitch is defined as the ratio between moment couple and force, given a wrench defined as,

$$d_i = \frac{\vec{\tau}_i \vec{f}_i}{\vec{f}_i \vec{f}_i} \quad (\text{D.57})$$

Since the wrench location vector and the force direction are orthogonal, the wrench location vector can be determined as,

$$\vec{b}_i = \frac{\vec{f}_i \times (\vec{\tau}_i - d_i \vec{f}_i)}{\vec{f}_i \vec{f}_i} \quad (\text{D.58})$$

Derivations and Algorithms

E.1. Derivation Translation as Rotation method

Similar to the RasT approach derivation, the translational compliance can be expressed as an equivalent rotational compliance, given as,

$$\tilde{a}_{\gamma_i} = \frac{a_{f_i}}{\psi_i^2} \quad (\text{E.1})$$

Converting the translational compliance into an equivalent rotational compliance at the point of interest using the virtual load method can be done in three consecutive steps.

- I Express θ_{eq_i} , an equivalent rotation at the point of interest in terms of a translation parallel to the wrench axis.
- II Express M_{eq_i} , an equivalent virtual moment at the point of interest in terms of the counteracting force corresponding to a translation parallel to the wrench axis.
- III Express an equivalent rotational compliance \tilde{a}_{γ_i} , by dividing the expressions above to obtain the equivalent translational compliance. That is,

$$\tilde{a}_{\gamma_i} = \frac{\theta_{eq_i}}{M_{eq_i}} \quad (\text{E.2})$$

Step I: Express θ_{eq_i} an equivalent rotation at the point of interest in terms of a translation parallel to the wrench axis.

$$\theta_{eq_i} = \frac{\delta_i}{\sqrt{|d_i^2| + b_i^2}} \quad (\text{E.3})$$

Step II: Express M_{eq_i} an equivalent virtual moment at the point of interest in terms of the counteracting force corresponding to a translation parallel to the wrench axis.

$$M_{eq_i} = \sqrt{|d_i^2| + b_i^2} F_i \quad (\text{E.4})$$

Step III: Express an equivalent rotational compliance \tilde{a}_{γ_i} , by dividing the expressions above to obtain the equivalent translational compliance. That is,

$$\tilde{a}_{\gamma_i} = \frac{\theta_{eq_i}}{M_{eq_i}} = \frac{1}{|d_i^2| + b_i^2} \frac{\delta_i}{F_i} \quad (\text{E.5})$$

The unification length ψ_i follows from Equation E.1 and E.5,

$$\psi_i = \sqrt{|d_i^2| + b_i^2} \quad (\text{E.6})$$

E.2. Derivation moment arm

The shortest distance between a point and a line is described by the surface area of the parallelogram constructed by two vectors. The The direction vector of the line and a vector from the point to any point on the line, divided by the magnitude of the direction vector. In the case of a compliant mechanism, the point is defined as the point of constraint and the line is defined as the force direction originating from the point of interest. The vector to any point on the line, is the vector from the point of constraint $P_{con}(x_0, y_0, z_0)$ to the

point of interest $P_{int}(x, y, z)$, given by $P_{int} - P_{con} = \vec{C}I$. The direction vector is the direction of the wrench axis given by \vec{f}_i . The visualisation of the moment arm can be seen in Figure E.1.

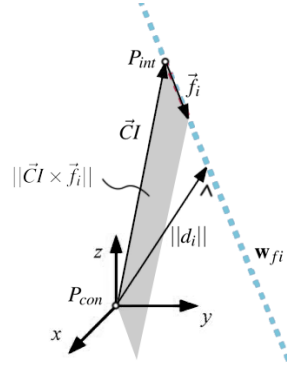


Figure E.1: Visualisation of moment arm magnitude $\|d_i\|$

In Equation form the moment arms are gives as,

$$d_i = \frac{\|\vec{C}I \times \vec{f}_i\|}{\|\vec{f}_i\|} \quad (\text{E.7})$$

E.3. Quantitative example

We have the following single corrugated shell mechanism

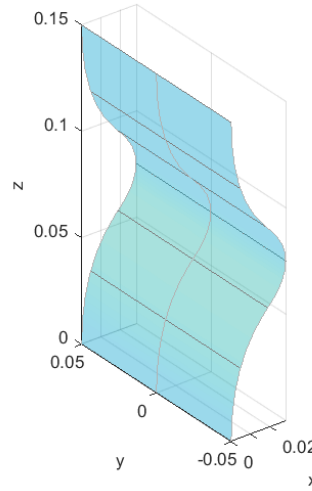


Figure E.2: Single corrugated shell mechanism

The tangent stiffness matrix of the single corrugated shell is given as,

$$K_t = 1.0 \times 10^5 \begin{bmatrix} 0.0150 & 0 & 0 & 0 & -0.0011 & 0 \\ 0 & 2.2079 & 0 & 0.1651 & 0 & 0.0570 \\ 0 & 0 & 0.3034 & 0 & -0.0017 & 0 \\ 0 & 0.1651 & 0 & 0.0130 & 0 & 0.0043 \\ -0.0011 & 0 & -0.0017 & 0 & 0.0003 & 0 \\ 0 & 0.0570 & 0 & 0.0043 & 0 & 0.0017 \end{bmatrix} \quad (\text{E.8})$$

The tangent stiffness matrix eigen-decomposition for the single corrugated shell becomes,

$$K_t = [\hat{\mathbf{w}}_f \quad \hat{\mathbf{w}}_\gamma] \begin{bmatrix} k_f & 0 \\ 0 & k_\gamma \end{bmatrix} \begin{bmatrix} \hat{\mathbf{w}}_f \\ \hat{\mathbf{w}}_\gamma \end{bmatrix} \quad (\text{E.9})$$

where

$$[\hat{\mathbf{w}}_f \quad \hat{\mathbf{w}}_\gamma] = \begin{bmatrix} 1.0000 & 0 & 0 & 0 & 0 & 0 \\ 0 & -1.0000 & 0 & 0 & 0 & 0 \\ 0 & 0 & 1.0000 & 0 & 0 & 0 \\ 0 & -0.0748 & 0 & 1.0000 & 0.0001 & 0 \\ -0.0739 & -0 & -0.0055 & 0 & 0 & 1.0000 \\ 0 & -0.0258 & 0 & -0.0001 & 1.0000 & 0 \end{bmatrix} \quad (\text{E.10})$$

and where

$$\begin{bmatrix} k_f & 0 \\ 0 & k_\gamma \end{bmatrix} = 1.0 \times 10^5 \begin{bmatrix} 0.0150 & 0 & 0 & 0 & 0 & 0 \\ 0 & 2.2079 & 0 & 0 & 0 & 0 \\ 0 & 0 & 0.3034 & 0 & 0 & 0 \\ 0 & 0 & 0 & 0.0006 & 0 & 0 \\ 0 & 0 & 0 & 0 & 0.0002 & 0 \\ 0 & 0 & 0 & 0 & 0 & 0.0002 \end{bmatrix} \quad (\text{E.11})$$

The tangent compliance matrix of the single corrugated shell is given as,

$$C_t = \begin{bmatrix} 0.0009 & 0 & 0 & 0 & 0.0035 & 0 \\ 0 & 0.0001 & 0 & -0.0012 & 0 & -0.0011 \\ 0 & 0 & 0 & 0 & 0.0003 & 0 \\ 0 & -0.0012 & 0 & 0.0163 & 0 & 0 \\ 0.0035 & 0 & 0.0003 & 0 & 0.0472 & 0 \\ 0 & -0.0011 & 0 & 0 & 0 & 0.0432 \end{bmatrix} \quad (\text{E.12})$$

The tangent compliance matrix eigen-decomposition is defined as,

$$C_t = [\hat{\mathbf{T}}_f \quad \hat{\mathbf{T}}_\gamma] \begin{bmatrix} a_f & 0 \\ 0 & a_\gamma \end{bmatrix} \begin{bmatrix} \hat{\mathbf{T}}_f \\ \hat{\mathbf{T}}_\gamma \end{bmatrix} \quad (\text{E.13})$$

where

$$[\hat{\mathbf{T}}_f \quad \hat{\mathbf{T}}_\gamma] = \begin{bmatrix} 1.0000 & 0 & 0 & 0 & 0 & 0.0739 \\ 0 & -1.0000 & 0 & -0.0748 & -0.0258 & 0 \\ 0 & 0 & 1.0000 & 0 & 0 & 0.0055 \\ 0 & 0 & 0 & 1.0000 & 0.0001 & 0 \\ 0 & 0 & 0 & 0 & 0 & 1.0000 \\ 0 & 0 & 0 & -0.0001 & 1.0000 & -0 \end{bmatrix} \quad (\text{E.14})$$

and where

$$\begin{bmatrix} a_f & 0 \\ 0 & a_\gamma \end{bmatrix} = \begin{bmatrix} 0.0007 & 0 & 0 & 0 & 0 & 0 \\ 0 & 0.0000 & 0 & 0 & 0 & 0 \\ 0 & 0 & 0.0000 & 0 & 0 & 0 \\ 0 & 0 & 0 & 0.0163 & 0 & 0 \\ 0 & 0 & 0 & 0 & 0.0432 & 0 \\ 0 & 0 & 0 & 0 & 0 & 0.0472 \end{bmatrix} \quad (\text{E.15})$$

The unified compliance vector representation becomes,

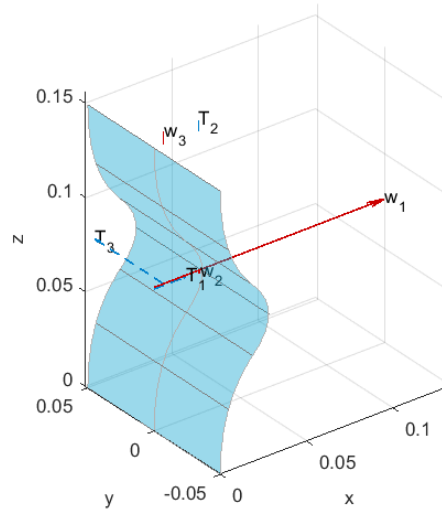


Figure E.3: Unified compliance vector of a single corrugated shell mechanism

Preliminary work synthesis

This master thesis introduces comprehensive non-linear characterization and classification methods, which are partially utilized in this chapter to introduce synthesis proposals for mechanism conjunctions and research directions.

F.1. Parallel and series conjunctions spatial mechanisms

Multiple mechanisms are connected in parallel when their corresponding end-effectors are joined which each other. The equivalent deflection of the combined point of interest is described as,

$$x_{eq} = x_1 = x_2 = \dots = x_n \quad (E1)$$

The equivalent force is given as,

$$F_{eq} = F_1 + x_2 + \dots + x_n \quad (E2)$$

The stored energy is described as,

$$E_{eq} = E_1 = E_2 = \dots = E_n \quad (E3)$$

If a system contains n spring mechanisms in parallel, the following statements are true. The equivalent stiffness constant is given as,

$$k_{eq} = k_1 + k_2 + \dots + k_n \quad (E4)$$

The equivalent compliance of a system containing n mechanisms in parallel is given as,

$$\frac{1}{c_{eq}} = \frac{1}{c_1} + \frac{1}{c_2} + \dots + \frac{1}{c_n} \quad (E5)$$

If a system contains n spatial mechanisms in parallel with the same point of interest, the following statements are true. The equivalent stiffness matrix is given as,

$$K_{eq} = K_1 + K_2 + \dots + K_n \quad (E6)$$

The equivalent compliance of a system containing n mechanisms in parallel is given as,

$$\frac{1}{C_{eq}} = \frac{1}{C_1} + \frac{1}{C_2} + \dots + \frac{1}{C_n} \quad (E7)$$

Multiple mechanisms are connected in series when joined end-to-end. The equivalent deflection of the combined point of interest is given as,

$$x_{eq} = x_1 + x_2 + \dots + x_n \quad (E8)$$

The equivalent force is given as,

$$F_{eq} = F_1 = x_2 = \dots = x_n \quad (E9)$$

The stored energy is described as,

$$E_{eq} = E_1 + E_2 + \dots + E_n \quad (E10)$$

If a system contains n spring mechanisms in series, the following statements are true. The equivalent stiffness constant is given as,

$$\frac{1}{k_{eq}} = \frac{1}{k_1} + \frac{1}{k_2} + \dots + \frac{1}{k_n} \quad (E11)$$

The equivalent compliance of a system containing n mechanisms in parallel is given as,

$$c_{eq} = c_1 + c_2 + \dots + c_n \quad (\text{F.12})$$

If a system contains n mechanisms in series, the following statements are true. The equivalent stiffness matrix is given as,

$$\frac{1}{K_{eq}} = \frac{1}{K_1} + \frac{1}{K_2} + \dots + \frac{1}{K_n} \quad (\text{F.13})$$

where all K matrices are given with respect to the same point of interest using super-positioning. The equivalent compliance of a system containing n mechanisms in parallel is given as,

$$C_{eq} = C_1 + C_2 + \dots + C_n \quad (\text{F.14})$$

We evaluate the compliant mechanisms A and B in series given in Figure F.1.

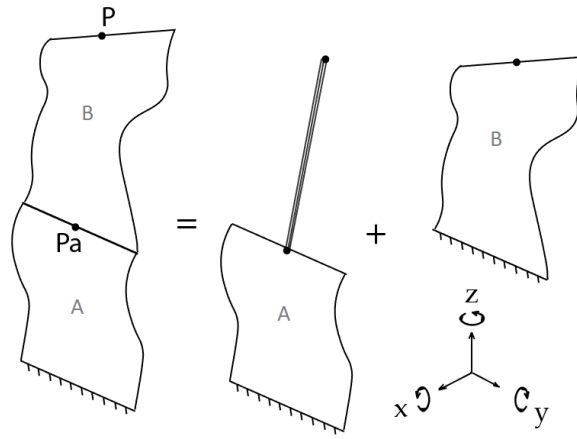


Figure F.1: Compliant mechanisms in series

The loads are transmitted to an imaginary rigid bar from the original point of interest P_a to the collective point of interest P . The vector that determines the length r of the rigid bar is the length of the remaining building block, from the base to point of interest, thus given as,

$$\vec{r} = P - P_a = \begin{bmatrix} r_x \\ r_y \\ r_z \end{bmatrix} \quad (\text{F.15})$$

The applied load on P is defined in Plücker coordinate vector form as the linear forces \vec{f} and the moment couples $\vec{\tau}$ defined as,

$$\vec{f}_P = \begin{bmatrix} f_x \\ f_y \\ f_z \\ \tau_x \\ \tau_y \\ \tau_z \end{bmatrix} \quad (\text{F.16})$$

The geometry necessary to calculate the reaction load on point P_a is given in figure F.2 and F.3.

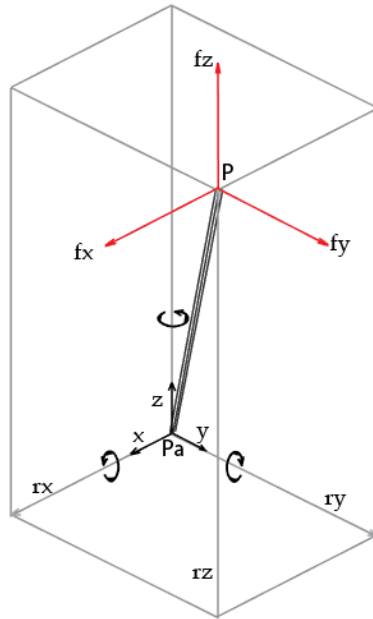


Figure E2: Geometry super-positioning

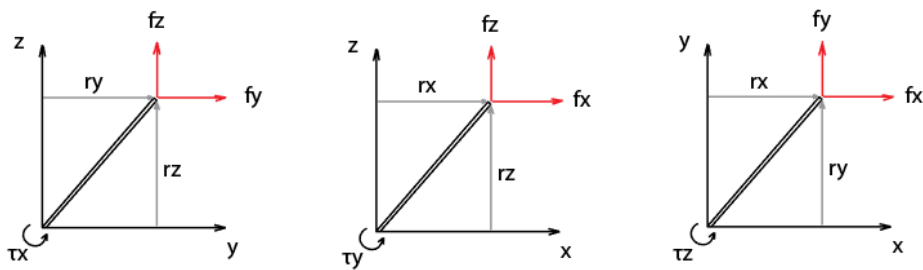


Figure E3: Geometry moments

The reaction load on P_a can be expressed as,

$$\vec{R}_{p1} = - \begin{bmatrix} f_x \\ f_y \\ f_z \\ \tau_x - r_z f_y + r_y f_z \\ \tau_y - r_z f_x + r_x f_z \\ \tau_z - r_y f_x + r_x f_y \end{bmatrix} \tag{E17}$$

The load on building building block 1 is the opposite of the reaction load \vec{R}_{p1}

$$\vec{f}_{P_a} = -\vec{R}_{p1} = \begin{bmatrix} f_x \\ f_y \\ f_z \\ \tau_x - r_z f_y + r_y f_z \\ \tau_y - r_z f_x + r_x f_z \\ \tau_z - r_y f_x + r_x f_y \end{bmatrix} \tag{E18}$$

We can rewrite \vec{f}_{P_a} in terms of \vec{f}_P as,

$$\vec{f}_{P_a} = \begin{bmatrix} 1 & 0 & 0 & 0 & 0 & 0 \\ 0 & 1 & 0 & 0 & 0 & 0 \\ 0 & 0 & 1 & 0 & 0 & 0 \\ 0 & -r_z & r_y & 1 & 0 & 0 \\ -r_z & 0 & r_x & 0 & 1 & 0 \\ -r_y & r_x & 0 & 0 & 0 & 1 \end{bmatrix} \begin{bmatrix} f_x \\ f_y \\ f_z \\ \tau_x \\ \tau_y \\ \tau_z \end{bmatrix} = \begin{bmatrix} 1 & 0 & 0 & 0 & 0 & 0 \\ 0 & 1 & 0 & 0 & 0 & 0 \\ 0 & 0 & 1 & 0 & 0 & 0 \\ 0 & -r_z & r_y & 1 & 0 & 0 \\ -r_z & 0 & r_x & 0 & 1 & 0 \\ -r_y & r_x & 0 & 0 & 0 & 1 \end{bmatrix} \vec{f}_P = H \vec{f}_P \quad (\text{E.19})$$

The matrix H transforms the load \vec{f}_P to \vec{f}_{P_a} accounting for the moment arm due to r . A similar analysis can be performed to determine the appropriate displacement at PA from the displacement at P. Resulting in the compliance matrix of mechanism A in point P given as,

$$C_p = H^T C_{P_a} H \quad (\text{E.20})$$

The total compliance due to mechanism A and B in series at point P is given as,

$$C = C_b + C_p \quad (\text{E.21})$$

As discussed in section E.1 and E.1, parallel en serial conjunctions of spatial mechanisms can be made. Assuming no negative stiffness the following statements are potentially valid:

- Rotational and translational stiffness increases with parallel conjugations.
- Rotational and translational compliance increases with serial conjugations.

Influence of super-positioning:

- Sub-matrix C_d does not change.
- Stationary rotational compliance and stiffness multipliers do not change.

Influence of super-positioning without taking into account the coupling:

- Sub-matrix C_d does not change.
- Eigen-twist direction, location and stationary compliance and stiffness multipliers do not change.

Multiple identical mechanism parallel:

- There is a linear relationship between the number of mechanisms and stationary stiffness multipliers.
- The direction and location of the eigen-twist and eigen-wrenches stays the same.

Two mechanisms sharing the same eigen-twist direction in series

- The resulting stationary rotational compliance is the sum of the two separate stationary rotational compliances, the direction stays the same and the location lies in between the two. (Pseudo-Rigid-Body)

F.2. Rigid-body replacement utilizing Lipkin's eigen-decomposition

If two mechanisms A en B are connected in series and share an eigen-twist direction, given as

$$\frac{T_{\gamma i}^A}{|T_{\gamma i}^A|} = \frac{T_{\gamma i}^B}{|T_{\gamma i}^B|} \quad i = 1, 2, 3 \tag{E.22}$$

The resulting combined eigentwist magnitude of $T_{\gamma i}^{AB}$ is given as,

$$a_{\gamma i}^{AB} = a_{\gamma i}^A + a_{\gamma i}^B \tag{E.23}$$

Which is proven by the following five statements: The resulting compliance matrix of a series concatenation is the results of the separate compliance matrices added with respect to the point of interested, achieved by the superposition matrix. The superposition matrix multiplication multiplied by the tangent compliance matrix as shown above has no influence on the sub-matrix C_d , due to the definition of the superposition matrix H , stated in E.19. The addition of matrices is done by adding corresponding elements assuming both are with respect to the same point of interest, given as,

$$C_I + C_{II} = \begin{bmatrix} C_{aI} + C_{aII} & C_{bI} + C_{bII} \\ C_{bI} + C_{bII} & C_{dI} + C_{dII} \end{bmatrix} \tag{E.24}$$

The eigentwists are defined by sub-matrix C_d of the resulting tangent compliance matrix C , the eigen-directions are defined by the eigen-vectors and the compliance multipliers by the eigen-values of C_d . The eigenvalue of the addition of two matrices with eigenvectors in the same direction is the result of the addition of the two corresponding eigenvalues. This section applicable to spatial mechanism however it is illustrated for a planar example in Figure ???. Equation E.22 is always valid for splanar mechanisms.

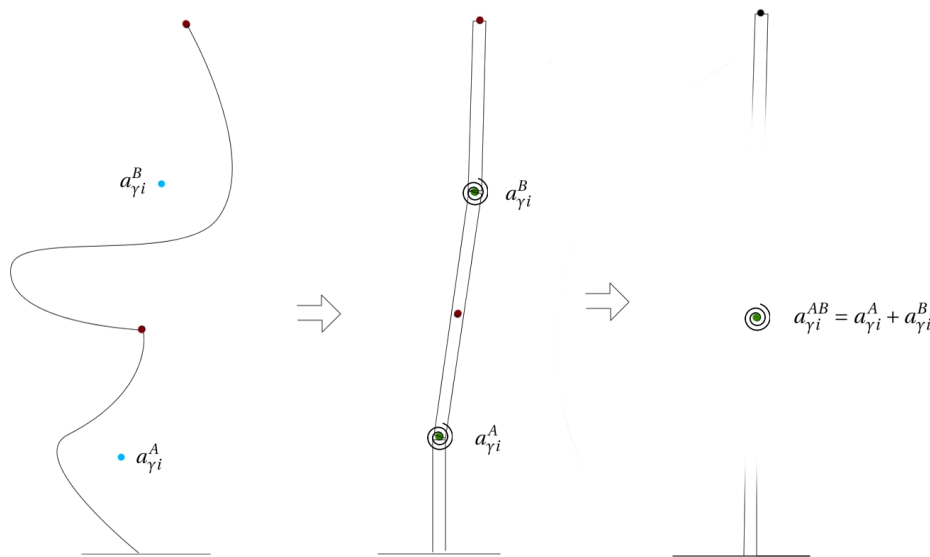


Figure E4: Rotational stationary multiplier summation

It is recommended to perform research to find the location of the resulting combined twist axis corresponding to the equivalent compliance. This could potentially form the basis for a synthesis method in combination with the subsequent section.

F.3. Systematic linearisation utilizing Lipkin's eigen-decomposition

This section proposes a theory to approximate non-linear behaviour of compliant mechanisms utilizing Lipkins eigen-decompositon [11]. This theory has the objective to find the equivalent linear principle twist axis with corresponding equivalent rotational stiffness multiplier of a non-linear compliant mechanism.

Subsequently the non-linear mechanism can be modelled as a pseudo rigid body model to simplify the non-linear behaviour.

This theory is based on the fact that an infinitesimal rotation of point I around a point II is similar to a rotation around any point on the line crossing point I & II. This is illustrated in Figure E5. Point P_I can be moved along the dotted line, however the resulting infinitesimal displacement will remain perpendicular to the dotted line.

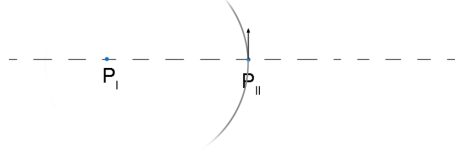


Figure E5: Linear approximation non-linear mechanism

The described phenomena is applied on flexure mechanism shown in Figure E6. Based on the definition of an eigen-wrench presented by Lipkin. If a moment is applied on the point of interest it will rotate around the its corresponding eigen-twist axis.

We plot the point of interest and eigen-twist locations along a deformation for a 2d flexure. An applied clockwise moment results in a clockwise rotational displacement, which is plotted various steps. The blue lines cross the point of interests and twists locations. The point of interests are plotted as red dots and the twist locations as crosses. The point of interest represents P_{I} and the twist location P_I . As described, the point of rotation indicating the infinitesimal displacement as result of the rotation can be anywhere on the corresponding blue lines. If we plot the blue line for every step in a stepwise analysis of an applied moment, we see that the blue lines cross. This point is a linear approximate twist axes that represents the the point of rotation of the point of interest along the deformation, plotted as a green dot. If we give linear approximate twist axes the average stiffness of the corresponding stiffness multipliers of each step, we can model the flexure as a linear approximated pseudo rigid body model, given as

$$k_{linearized} = \frac{1}{n} \sum_{i=1}^n k_{\gamma_i} \quad (F.25)$$

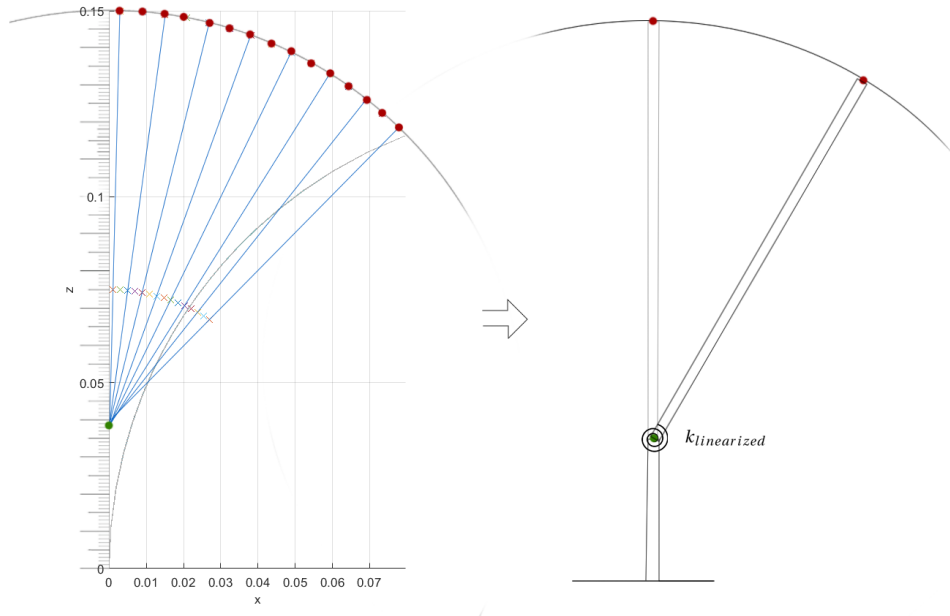


Figure E6: Linear approximation non-linear mechanism

The equivalent pseudo-rigid-body model can be constructed using the linearised equivalent eigen-twist location.

The proposed preliminary theory is applied on the flexure since it is a striking well-described example mechanism. However the proposed preliminary theory can be applied on any mechanism that can be decomposed using Lipkin's eigen-decomposition. This includes spatial mechanisms. However, the in Figure E6 not always cross. Further research is necessary to expand this proposed theory by including eigenwrenches and mechanisms which do not have a clear linearisation point.

Bibliography

- [1] Gerben J Bulthuis, Albert G Veldhuizen, and Gert Nijenbanning. Clinical effect of continuous corrective force delivery in the non-operative treatment of idiopathic scoliosis: a prospective cohort study of the triac-brace. *European Spine Journal*, 17(2):231–239, 2008.
- [2] Frederique Desbiens-Blais, Julien Clin, Stefan Parent, Hubert Labelle, and Carl-Eric Aubin. New brace design combining cad/cam and biomechanical simulation for the treatment of adolescent idiopathic scoliosis. *Clinical biomechanics*, 27(10):999–1005, 2012.
- [3] Juan A Gallego and Just Herder. Synthesis methods in compliant mechanisms: An overview. In *ASME 2009 International Design Engineering Technical Conferences and Computers and Information in Engineering Conference*, pages 193–214. American Society of Mechanical Engineers, 2009.
- [4] Jonathan Brigham Hopkins. *Design of parallel flexure systems via freedom and constraint topologies (FACT)*. PhD thesis, Massachusetts Institute of Technology, 2007.
- [5] Larry L Howell. *Compliant mechanisms*. John Wiley & Sons, 2001.
- [6] C.J. Kim J.P.A. Nijssen, G. Radaelli and J.L. Herder. Overview and kinematic characterization of compliant shell mechanism building blocks. 2016.
- [7] C.J. Kim J.P.A. Nijssen, G. Radaelli and J.L. Herder. Design and analysis of a shell mechanism based two-fold force controlled scoliosis brace. 2016.
- [8] Charles J Kim. *A conceptual approach to the computational synthesis of compliant mechanisms*. PhD thesis, 2005.
- [9] Charles J Kim, Yong-Mo Moon, and Sridhar Kota. A building block approach to the conceptual synthesis of compliant mechanisms utilizing compliance and stiffness ellipsoids. *Journal of Mechanical Design*, 130(2):022308, 2008.
- [10] Girish Krishnan, Charles Kim, and Sridhar Kota. An intrinsic geometric framework for the building block synthesis of single point compliant mechanisms. *Journal of Mechanisms and Robotics*, 3(1): 011001, 2011.
- [11] Harvey Lipkin and Timothy Patterson. Generalized center of compliance and stiffness. In *Robotics and Automation, 1992 Proceedings, 1992 IEEE International Conference on*, pages 1251–1256. IEEE, 1992.
- [12] Nancy Hadley Miller. Cause and natural history of adolescent idiopathic scoliosis. *Orthopedic Clinics*, 30(3):343–352, 1999.
- [13] Junuthula Narasimha Reddy. *Theory and analysis of elastic plates and shells*. CRC press, 2006.
- [14] Manuel Rigo and H Weiss. The chèneau concept of bracing-biomechanical aspects. *Studies in Health Technology and Informatics*, 135:303, 2008.
- [15] J B Ring, Charles J Kim, Jeffrey Evans, and Craig Beal. A Passive Brace for the Treatment of Scoliosis Utilizing Compliant Mechanisms. Master’s thesis, Bucknell University, Lewisburg PA, 2017.
- [16] Daniel Rolton, Colin Nnadi, and Jeremy Fairbank. Scoliosis: a review. *Paediatrics and Child Health*, 24(5):197–203, 2014.
- [17] Marek Teichmann. A grasp metric invariant under rigid motions. In *Robotics and Automation, 1996. Proceedings., 1996 IEEE International Conference on*, volume 3, pages 2143–2148. IEEE, 1996.
- [18] Fred van Keulen. *On refined triangular plate and shell elements*. Cambridge university press, 1998.
- [19] Stuart L Weinstein, Lori A Dolan, James G Wright, and Matthew B Dobbs. Effects of bracing in adolescents with idiopathic scoliosis. *New England Journal of Medicine*, 369(16):1512–1521, 2013.